UNIVERSIDADE DE SÃO PAULO
ESCOLA DE ENGENHARIA DE SÃO CARLOS

Bernardo Martinez Rocamora Junior

Experimental Analysis of Fan Noise and Performance at the EESC-USP Fan Rig Workbench

São Carlos, Brasil

2019

Bernardo Martinez Rocamora Junior

Análise Experimental de Ruído e Performance de Fan na Bancada EESC-USP Fan Rig

Dissertação apresentada à Escola de Engenharia de São Carlos da Universidade de São Paulo, para obtenção do título de Mestre em Ciências - Programa de Pós-Graduação em Engenharia Mecânica.

Área de concentração: Aeronaves

Supervisor: Prof. Dr. Paulo Celso Greco Junior

ESTE EXEMPLAR TRATA-SE DA VERSÃO CORRIGIDA. A VERSÃO ORIGINAL ENCONTRA-SE DISPONÍVEL JUNTO AO DEPARTAMENTO DE ENGENHARIA MECÂNICA DA EESC-USP.

São Carlos, Brasil
2019

Ficha catalográfica elaborada pela Biblioteca Prof. Dr. Sérgio Rodrigues Fontes da EESC/USP com os dados inseridos pelo(a) autor(a).

Martinez Rocamora Junior, Bernardo
M385e Experimental Analysis of Fan Noise and Performance at the EESC-USP Fan Rig Workbench / Bernardo Martinez Rocamora Junior; orientador Paulo Celso Greco Junior. São Carlos, 2019.

Dissertação (Mestrado) - Programa de Pós-Graduação em Engenharia Mecânica e Área de Concentração em Aeronáutica -- Escola de Engenharia de São Carlos da Universidade de São Paulo, 2019.

1. Fan noise. 2. Fan aerodynamics. 3. Spectral analysis. 4. Modal analysis. 5. Rotor-stator interaction. 6. Instrumented stator vane. I. Título.

Eduardo Graziosi Silva - CRB - 8/8907

FOLHA DE JULGAMENTO

Candidato: **BERNARDO MARTINEZ ROCAMORA JUNIOR**

Título da dissertação: "Análise experimental de ruído e performance de fan na bancada EESC-USP Fan Rig"

Data da defesa: 08/02/2019

Comissão Julgadora:	**Resultado:**
Prof. Associado **Paulo Celso Greco Junior** **(Orientador)** (Escola de Engenharia de São Carlos/EESC)	APROVADO
Prof. Dr. **Júlio Apolinário Cordioli** (Universidade Federal de Santa Catarina/UFSC)	APROVADO
Prof. Dr. **Carlos do Carmo Pagani Junior** (Universidade Estadual Paulista "Júlio de Mesquita Filho"/Unesp)	Aprovado

Coordenador do Programa de Pós-Graduação em Engenharia Mecânica:
Prof. Titular **Gherhardt Ribatski**

Presidente da Comissão de Pós-Graduação:
Prof. Titular **Luís Fernando Costa Alberto**

This work is specially dedicated to my parents, Dora and Bernardo.

ACKNOWLEDGEMENTS

First and foremost, I would like to thank my parents, Bernardo and Dora. You both have always motivated me to become a better version of myself and have provided everything in your capacities to help me be where I am, and everything I achieved is owed to you. I would like to thank my brother Henrique, my best friend. I would also like to thank other members of my family: my grandmother Eloina, my grandfather Nanminando - who is no longer with us but lives in our memories -, my uncle Zé, my aunt Zenaide, my cousin Daniel, and everyone else. You have been really important and helped me a lot throughout these years of studies. I love you all.

I would like to thank my advisor Prof. Paulo Greco for your help, mentoring and guidance. You have been really patient during these last few years and have given me lots of insights when problems appeared. You have dedicated much of your time to run experiments with me and for that I am really indebted. Also, I would like to thank Prof. Fernando Catalano for devoting some of his time to arrange bursary issues and for giving advices regarding many aspects of experimental aerodynamics in the Rig. I would like to thank my friend Luciano Caldas and Dr. Rafael Cuenca who extensively have helped me learning aeroacoustics, electronics, the experimental procedures of the Rig and much more and I am grateful of having you as friends. I thank Eng. Rudner Lauterjung, that was in step with the project and has also helped in many regards.

Mario Sbampato is thanked for helping me design many instrumentation devices that were necessary these two years, including the design and manufacturing of the instrumented stator vane. Also I would like to thank him for taking some of his time to teach me electronics. Fábio Gallo is thanked by manufacturing most of the mechanical parts that I have designed and needed for this project. José Cláudio, Claudinho, is thanked for making the work at Campus 2 more pleasant, solving all sorts of infrastructure problems, making coffee for the students and helping me assemble, disassemble and assemble the Rig over and over again. Osnan is thanked for helping me assemble the Anechoic Termination, making a lot of woodwork for the Rig and painting the instrumented stator vane. I also would like other staff at the Department of Aeronautical Engineering, who were always kind to me.

I would like to thank my friends at the República Poltergeist. Living in a fraternity is an experience of great personal growth, of tolerance development and of leadership. There I have met some of my best friends and it is where I have spent some of the best moments of my life. I would like to thank my friend Dr. Rubens Belfort, which was very supportive in this university years too. I would like to thank the following communities, promulgators of knowledge and science, and that helped me on a daily basis: Mathworks,

LaTeX, Arduino, Youtube, Stack Exchange, Stack Overflow.

Finally, I want to thank the University of São Paulo, my *alma mater*, for being an excellent centre for development of knowledge and that gave me the conditions needed for doing this work. I would like to thank Embraer and the funding agencies CNPQ and FINEP, for providing resources for this project. And I would to thank people of São Paulo and the rest of Brazil, whose taxes were allocated to fund the university and part of my studies.

Bernardo Martinez Rocamora Junior
São Bernardo do Campo, Brazil
October, 2018

"Basic research is what I am doing when I don't know what I am doing."
Wernher von Braun

ABSTRACT

MARTINEZ R. Jr., Bernardo **Experimental Analysis of Fan Noise and Performance at the EESC-USP Fan Rig Workbench**. 2019. 123p. Master Thesis - Escola de Engenharia de São Carlos, Universidade de São Paulo, São Carlos, Brasil, 2019.

The study of turbofan aeroacoustics has become important in academia and industry as noise from other aircraft sources, as jet noise, have been reduced. The EESC-USP Fan Rig is a long-duct low-speed fan experimental setup recently built at the Department of Aeronautical Engineering of the University of São Paulo. The objective is to provide a facility for studying fan aeroacoustics with a flexible configuration that allows changes in operational conditions and geometry of the rig so that each of the noise sources can be treated separately. In this work, three experimental campaign were taken aiming to extend the knowledge of this workbench capabilities and to observe the effect that some parameters can have on noise generation. A performance campaign was carried out to characterise the effects of controllable parameters on the aerodynamic characteristics of the flow. Starting from unrestricted flow to 70% area constraint, and a range of fan speeds, several flow measurements that could be translated into performance quantities were taken: volume flow rate, fan total and static pressures, compression ratio, total and net power, and efficiency. The measured compression ratio ranged from 1.00 to 1.02, with maximum axial Mach of 0.13 and maximum total efficiency of 65%. The surge effect, an unstable configuration characterised by rotor blades stall was also observed. Significant differences in fan performance due to the installation of an Inlet Control Device (ICD) and the rotor-stator spacing were not found, except under surge conditions. A parametric campaign was carried out exploring the effects of fan rotational speed, fan loading and rotor-stator spacing. Acoustic measurements were taken using an array of 77 wall-mounted microphones to provide a baseline data set for future comparisons. Hereby, data was processed to obtain the modal decomposition and power spectrum for each configuration. The last proved useful to compare tonal and broadband noise for each configuration. Experimental results indicate that changes in fan rotational speed scale noise generation mechanisms proportionally, do not affect noise spectral shape, and in consequence, are not useful to distinguish noise mechanisms. Although throttling does not seem to exhibit a clear effect on fan noise, it turns out that it is a good approach for cross-comparisons of other parameters' effect on fan noise, because of its direct modification on the flow structure within the duct. Results also showed that increasing rotor-stator spacing reduces both blade passing frequencies tone levels and the acoustic power of the interaction modes, which are in agreement with results obtained by similar test facilities. In this work a instrumented stator vane was designed using recently available technologies, as 3D printing and the use of MEMS microphones, to measure this pressure fluctuations. Phase-averaging and the signal from a hall sensor were used to separate broadband content in time series. Broadband level distribution were analysed for two span lines of the instrumented stator vane and for a reference microphone located in the inlet antenna. Broadband levels increased with the increase in fan speed and its distribution over these span lines maintained its shape for different speeds. Cross-correlation of the microphones were calculated and showed decay of zero-delay cross-correlation with increase in distance between microphones over the vane. And, finally, the integral length scale, obtained by the integration of zero-delay cross-correlation curve, showed decay with increase in fan speed. The data generated by this work showed good agreements with what was expected from the literature and will help as input data to the semi-analytical and semi-empirical models that are being developed in parallel by the research group.

Keywords: Fan noise. Fan aerodynamics. Spectral analysis. Modal analysis. Rotor-stator interaction. Instrumented stator vane.

RESUMO

MARTINEZ R. Jr., Bernardo **Análise Experimental de Ruído e Performance de Fan na Bancada EESC-USP Fan Rig**. 2019. 123p. Dissertação (Mestrado) - Escola de Engenharia de São Carlos, Universidade de São Paulo, São Carlos, Brasil, 2019.

O estudo da aeroacústica de *fan* tornou-se importante na academia e na indústria à medida que o ruído de outras fontes nas aeronaves, como o ruído de jato, foram reduzidas. O EESC-USP Fan Rig é um túnel de vento aeroacústico voltado para *fans* de baixa velocidade, que foi construído recentemente no Departamento de Engenharia Aeronáutica da Universidade de São Paulo. Seu objetivo é prover uma bancada experimental para o estudo dos mecanismos de geração de ruído de *fan* com uma configuração flexível que permita mudanças nas condições operacionais e geométricas de forma a isolar tanto quanto possível cada uma das fontes. Neste trabalho foram realizadas três campanhas experimentais visando aprofundar os conhecimentos sobre as capacidades da bancada e observar os efeitos no ruído que algumas variações paramétricas podem gerar. Uma campanha de performance de *fan* foi realizada para quantificar os efeitos dos parâmetros controláveis sobre o as características aerodinâmicas do escoamento. Partindo de escoamento sem restrição até restrição de área de 70%, e para diversas velocidades de rotação do *fan*, diversas medidas do escoamento foram feitas para que se pudesse calcular as métricas de performance: vazão volumétrica, pressão total e estática do *fan*, taxa de compressão, potência útil, potência elétrica de entrada e eficiência. Os resultados apontaram para uma taxa de compressão entre 1.0 e 1.02, com Mach axial máximo de 0.13 e eficiência máxima de 65%. Os efeitos de “surge”, uma configuração instável caracterizada pelo estol das pás do rotor também foi observado. Diferenças significativas na performance do *fan* devido à instalação de uma Inlet Control Device (ICD) e pelo espaçamento entre rotor e estator não foram encontradas, com exceção em condições de “surge”. Uma campanha paramétrica para estudo de ruído foi realizada explorando os efeitos da velocidade de rotação e carregamento no *fan*, espaçamento entre rotor-estator e condição de entrada do escoamento no duto. Os resultados mostraram que o aumento do espaçamento do rotor-estator reduz os níveis tonais nas frequências de passagem das pás (BPFs) a uma taxa de aproximadamente 4dB quanto o espaçamento é duplicado. Os resultados experimentais indicam que as mudanças nos mecanismos de geração de ruído com a velocidade rotacional do *fan* escalam-se proporcionalmente, não afetam a forma espectral do ruído e, por conseqüência, não são úteis para distinguir os mecanismos de ruído. Embora a variação no carregamento não pareça exibir um efeito claro no ruído do *fan*, verifica-se que é uma boa abordagem para comparações cruzadas, em conjunto com a velocidade de rotação, do efeito de outros parâmetros no ruído do *fan*, já que, desta forma, é possível fazer uma modificação direta na estrutura do escoamento dentro do duto. Os modos Tyler-Sofrin, esperados pela contagem de pás e aletas usadas no conjunto rotor-estator, foram identificados e a potência acústica desses modos de interação acompanham a potências dos respectivos tons no espectro, levando à conclusão que a maior contribuição para o ruído tonal é, de fato, a interação rotor-estator. Também neste trabalho, também foi projetada uma aleta de estator instrumentada, usando tecnologias recentemente disponíveis, como a impressão 3D e o uso de microfones MEMS, para realizar medições de flutuação de pressão na superfície superior da aleta. Um método de processamento de sinal foi desenvolvido, usando a técnica de “phase averaging” combinada com o sinal de um sensor Hall para separar o conteúdo de banda larga em séries temporais. A distribuição do nível de ruido banda larga foi analisado para duas linhas na envergadura da aleta instrumentada e em um microfone de referência localizado na antena de microfonnes. Os níveis de banda larga aumentaram com o aumento da velocidade do *fan* e a sua distribuição ao longo destas linhas de alcance manteve a sua forma para diferentes velocidades. As correlações cruzadas dos microfones foram calculadas e mostraram o decaimento da correlação cruzada de zero-atraso com o aumento da distância entre os microfones sobre a aleta. Finalmente, a integral do comprimento de escala, obtida pela integração da curva de correlação cruzada de zero-atraso, apresentou decaimento com aumento na velocidade do *fan.* Os dados gerados por esse trabalho se mostraram de acordo com o esperado na literatura da área e servem de dados de entrada para modelos semi-empíricos e semi-analíticos que vem sendo desenvolvidos paralelamente pelo grupo de pesquisa.

Palavras-chave: Ruído de *fan.* Aerodinâmica de *fan.* Análise espectral. Análise modal. Interação rotor-estator. Aleta de estator instrumentada.

LIST OF FIGURES

LIST OF TABLES

CONTENTS

1 INTRODUCTION

The large increase in aerial transportation brought a very unpleasant problem to urban life: aircraft noise. Considered one of the most undesirable feature of life in the cities, noise - defined as "unwanted sound" - is an important challenge that remain unsolved by the aeronautical engineering community and, consequently, it is a major concern for regulators. International Civil Aviation Organization's (ICAO) 2016 Environmental Report lists some of the social consequences caused by the exposure to aircraft noise in communities surrounding the busiest airports: the most obvious being the community annoyance, but also children learning deficits, sleep disturbance, and increase in health issues (e.g. cardiovascular diseases and hypertension) (ICAO, 2016). For these reasons, aircraft noise sets a clear limit to traffic growth on these airports.

Therefore, to allow increased aircraft operation, some attitudes were in need and ICAO has also developed a policy, called Balanced Approach to Aircraft Noise Managements, which aims to reduce noise in four pillars: (1) Reduction of Noise at Source, (2) Land-use Planning and Management, (3) Noise Abatement Operational Procedures, (4) Operating Restrictions. Reduction of Noise at Source is the pillar that concerns the most Aeroacoustics scientists and engineers and is controlled by setting noise limits for aircraft at some certification reference points. This stringement in noise limits forces the aircraft designers to incorporate into their product the latest technologies available (ANNEX, 2004).

1.1 Basic Concepts of Noise and Quantification

Sound is defined as the pressure (or density) fluctuations occurring anywhere in a fluid that, after propagating through the surrounding medium outward their source, arrive at the ear and cause vibrations on the eardrum which are recognised by the brain (GOLDSTEIN, 1976). Sound is around us in many daily life situations as human communication and music. These are generally pleasant sounds to us, but that is not always the case, for example, the majority of the sounds generated by engineering purposes are not pleasant, on the contrary, they can be very annoying. This unwanted sound is called noise.

Sound propagates as a wave and, as it propagates, it transports energy with it. The sound power (PWL) is a measure of the sound power output compared to a reference sound power of $P_0 = 10^{-12}W$ and is defined as:

$$\begin{aligned} \text{PWL [dB]} &= 10\log_{10}\left(\frac{\text{sound power output [W]}}{P_0}\right) \\ &= 10\log_{10}\left(\frac{\text{sound power output [W]}}{10^{-12}W}\right) \end{aligned} \tag{1.1}$$

The pressure field p on a fluid can be represented as $p_0 + p^{'}$, where p_0 is a uniform pressure and $p^{'}$ is as fluctuation over it. The sound pressure level (SPL) is a measure of the mean square level of fluctuation compared to a reference pressure level $p_0 = 2 \times 10^{-5}$ and is defined as:

$$\begin{aligned} \text{SPL [dB]} &= 10\log_{10}\left(\left(\frac{p^{'}_{rms}}{p_0}\right)^2\right) \\ &= 10\log_{10}\left(\left(\frac{p^{'}_{rms}[Pa]}{2 \times 10^{-5}Pa}\right)^2\right) \end{aligned} \tag{1.2}$$

where $p^{'2}_{rms} = \overline{p^{'2}}$, the overbar denotes time averaging.

For the human being, the SPL threshold of pain is between 130 and 140 dB, corresponding to a pressure variation of $p^{'}/p_0 = 10^{-3}$ and the SPL threshold of hearing is around 0 dB. Also, the audible frequency range for humans is between 20 and 20 kHz.

1.2 Aircraft Noise Certification Process

The noise levels for an aircraft in the certification phase has to be calculated in a standard manner as described in ICAO's Annex 16 (ANNEX, 2004), since it cannot be directly measured. This metric varies both with intensity and frequency of noise is needed to express human response to either loudness or annoyance. It takes into account the human response to specific frequency annoyance, intensity, tones and the total exposure time to the noise. The measurements need to be taken at some different reference points: (1) Fly-over (6.5 km from the brake release point, under the takeoff flight path); (2) Sideline (the highest noise measurement recorded at any point 450 m from the runway axis during take-off); and (3) Approach (2 km from the runway threshold, under the approach flight path), as shown in Figure 1. Also, the permitted levels varies with the weight of the aircraft and constantly are being lowered by updates on the Annex 16, Chapter 14, which defines the current situation.

1.3 Aircraft Noise Sources

Noise is generated in many aircraft regions and often can be studied separately. In general, the many contributors to overall aircraft noise are divided in two main groups:

Figure 1: ICAO's aircraft noise certification.

(a) Reference measurement points.

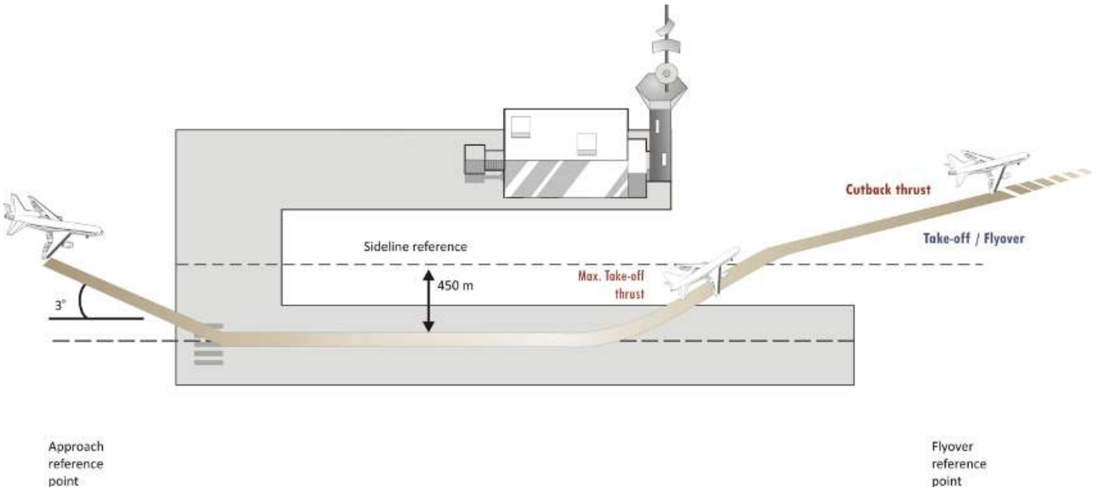

(b) Evolution of noise stringement.

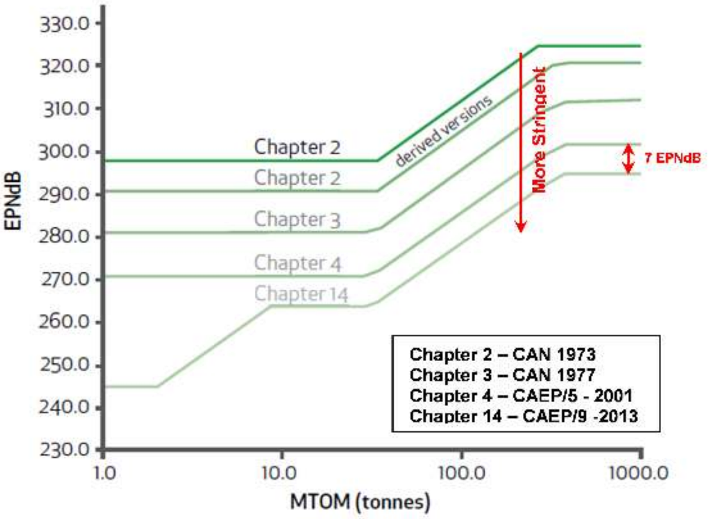

Source: ICAO (2016).

airframe noise and engine noise. Airframe noise accounts for the noise generated by the parts that do not contribute to the aircraft propulsion (see Figure 2): wings, fuselage, tailplane, nacelle, and their appendices (flaps, slats, spoilers, doors, etc.). Currently, the most important airframe noise sources are high lift devices, as slats and flaps, and undercarriage (landing gears). These devices are used in either or both take-off and landing conditions, making them critical for the certification processes.

Engine noise, for instance, is related to the parts that generate thrust: fans, propellers, engine core (compressors, combustor, and turbine), and exhaust jets. Engine noise have a peculiar characteristic, since many of them are constituted of rotating parts, as propellers, fans, compressors and turbines, they have both tonal - noise in discrete frequencies related to their cyclic motion - and broadband noise - related to turbulence - in their noise signature. Jet noise has its origin in the mixing process of the exhaust flow leaving the engine with the atmosphere and was the most prominent source in turbojet aircraft. This type of noise has been greatly reduced with the dissemination of the turbofans replacing turbojet engines and with the development of new engines technologies in general. The other sources became more important then, and are the new challenge for the scientific community.

1.4 Fan Noise: The New Target

Overall aircraft noise had been dominated by jet mixing layer noise with the spread of the "jet engine", because this type of noise scales with the velocity to the eighth power and faster aircraft meant, necessarily, noisier aircraft. The dawn of the fan usage came with the pursuit for the increase in efficiency and ways to reduce the jet noise. Engineers added a bypass flow, encasing the core high speed flow, with lower speeds and increasingly flow rate through it, resulting large diameter fans. With these bigger fans and lower exhaust flow speeds, fan noise started to play an important role on overall aircraft noise. Today, depending on the aircraft condition, fan noise can be the dominant source. At the rotor (fan self-noise), inflow disturbances, inlet boundary layer, interaction potential field and tip vortices can be possible noise generators. At the stator, the wakes, vortices and turbulence generated by the rotor and the interaction potential field can be seen as noise generators. Rotor-stator interaction noise is generated by the impingement of fan wakes on stator vanes, creating a strong pressure fluctuation field over them. This has been postulated as one of the most important noise sources during take-off and landing operations of an aircraft, when the fan blade tips are in subsonic condition.

1.4.1 Fan Noise Types

Like any turbomachinery, fan system has two main types of sound characteristics on frequency domain: tonal and broadband, as shown in Figure 3. Tonal noise has been of great interest because certification procedures penalise single frequency content (which tends to be more annoying), but it has much consolidated knowledge. Tonal noise is generated by pressure fluctuations locked to the rotor revolutions. For subsonic fan, the main sources of discrete tones are cyclic pressure-field, inflow non-uniformities, and wake interactions between rotating and stationary stages, since there is not presence of shock waves. The proximity of the fan and the stator can generate a very intense pressure-field interaction but this effect can be reduced by increasing the spacing between rotating and stationary stages, since the wake interaction with downstream stages is a dominant noise source and the intensity of these tones depend on the strength of the wake, that diminishes with distance. The frequencies at which tones are observed are multiple of the fundamental

Figure 2: Main aircraft noise sources.

(a) Airframe noise sources.

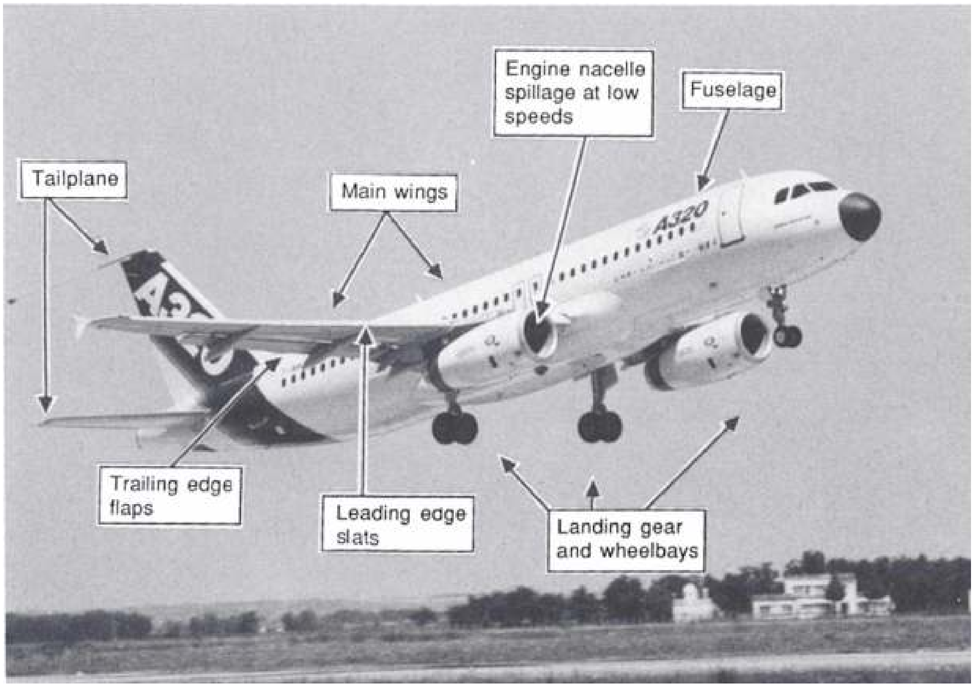

(b) Engine noise sources.

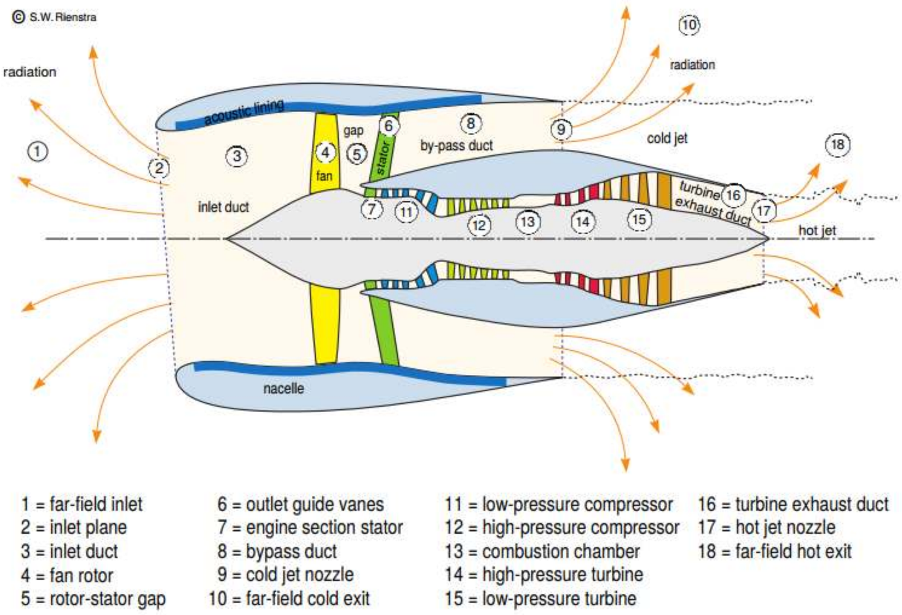

Source: Smith (1972) and Rienstra e Hirschberg (2014).

frequency, called Blade Passage Frequency (BPF), which is dependent on the number of blades, B, and the rotational speed (in rpm), Ω:

$$f_{BPF} = \frac{B\Omega}{60} \tag{1.3}$$

While tonal part is well understood and has already been modelled, broadband, the content that appears at similar levels for any frequency, knowledge is still incipient and experimental methods can provide insights and data for on-going research. Broadband is of great interest of the academia today and its noise content results from the pressure fluctuations associated with turbulent flow in the vicinity of the surface of the blades. The important sources for turbulence are the turbulence ingested from the atmospheric inflow, the boundary layers that grow on the fan casing, flow separations and blade wakes (SMITH, 2004).

Figure 3: Typical noise spectrum generated by a subsonic fan.

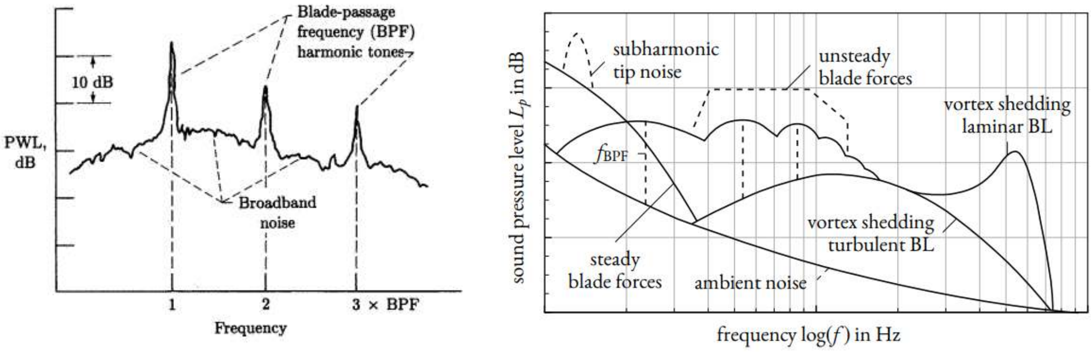
(a) Simplified schematics.

(b) Other sources schematics.

Source: Hubbard (1991) and Krömer (2018).

1.4.2 Fan Noise Generation Process

Figure 4 shows the generation process of noise within a fan stage. Both internal and external disturbances, like periodic impingement of blade wakes on stator vanes, cause unsteady surface pressure oscillations, which generate noise. The generated sound couples itself to the duct and the acoustic modes propagate to duct intake or exhaust sections where the acoustic modes are propagated into far-field. In the flowchart (Figure 4), every round shaped block can be measured by the proper instrumentation in a fan rig. For instance, internal and inflow disturbances can be measured with the use of anemometers (e.g. Pitot tubes, hot-wire anemometers), unsteady blade and vane surface pressures can be measured with fast-response pressure transducers or microphones, duct acoustic mode contents can be measured with microphones and convoluted signal processing, and, finally, far-field directivity can be measured with microphone antennas.

Most authors will divide the sources of sound in axial fans as: rotor self-noise and interaction noise. Rotor self-noise include many generation mechanisms: boundary layer noise, boundary layer separation noise, trailing edge noise for laminar and turbulent boundary layers, trailing edge vortex shedding, tip noise, steady loading noise, and thickness

Figure 4: Noise generation process at the fan stage.

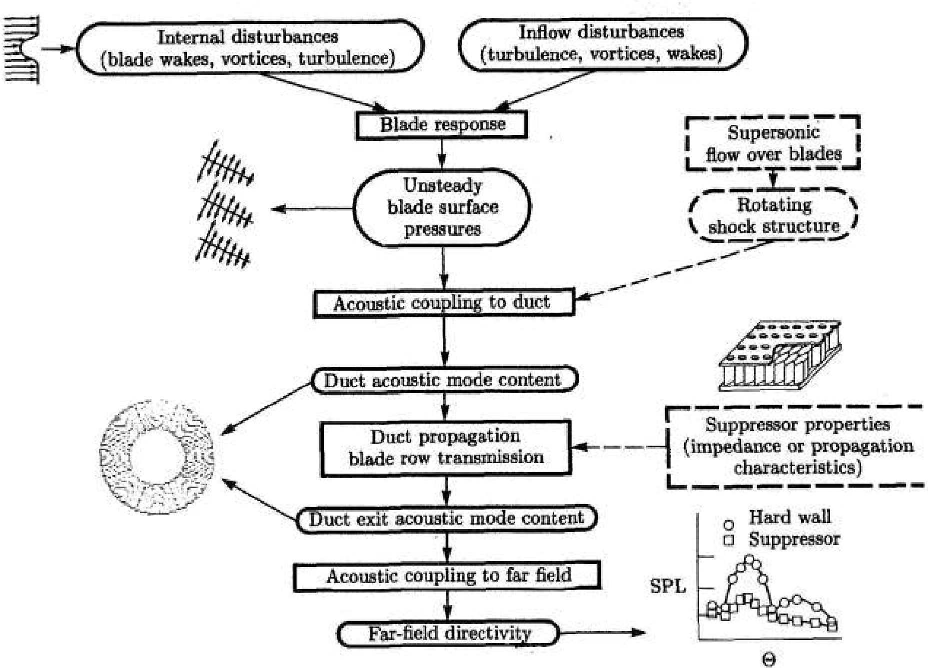

Source: Hubbard (1991).

noise. Interaction noise can be due to turbulence ingestion or unsteady loading noise, caused by turbulence, non-homogeneous flow and rotor-stator interactions. Other, lesser explored, sources can appear as sub-harmonic tip noise and rotating stall noise. These sources and their spectral characteristics are compiled in Table 1.

Table 1: Aeroacoustic sound sources and source characteristic in axial fans

Mechanism		Tonal	Narrowband	Broadband
Rotor Self Noise	Boundary Layer (BL) Noise			X
	BL Separation Noise	X		X
	Trailing Edge (TE) Noise (Laminar BL)	X		
	TE Noise (Turbulent BL)	X		X
	Blunt TE Vortex Shedding	X		
	Tip Noise			X
	Steady Loading Noise	X		
	Thickness Noise	X		
Turbulence Ingestion (Leading Edge) Noise				X
Unsteady Loading Noise		X		
Subharmonic Noise			X	
Rotating Stall			X	

Source: Adapted from Krömer (2018).

1.5 Methodology Strategies

Three approaches are necessary in the development of new and quieter engine designs: prediction, numerical simulation and experimental, each one with its due importance. Figure 5 shows the three approaches and how they are connected. Prediction is the creation of models that describe the system with simplicity, usually supported by empirical data and analytic formulations of the problem. This is an approach that can be reproduced several times with low cost and therefore, are able to assess multiple design configurations at once and obtain optimum design. Numerical simulation approach is computationally expensive and time demanding, but it provides great insight into physical mechanisms and provide data in all desired domain points, allowing more complete data. The experimental approach is very limited in versatility, since the preparation for a single experiment can take a lot of time and can very expensive. Also, the amount of data extracted is localised and limited. Nevertheless, this approach is the only one that provide true and reliable input data for the other two approaches to be validated.

Figure 5: Research methodology for fan aeroacoustics design.

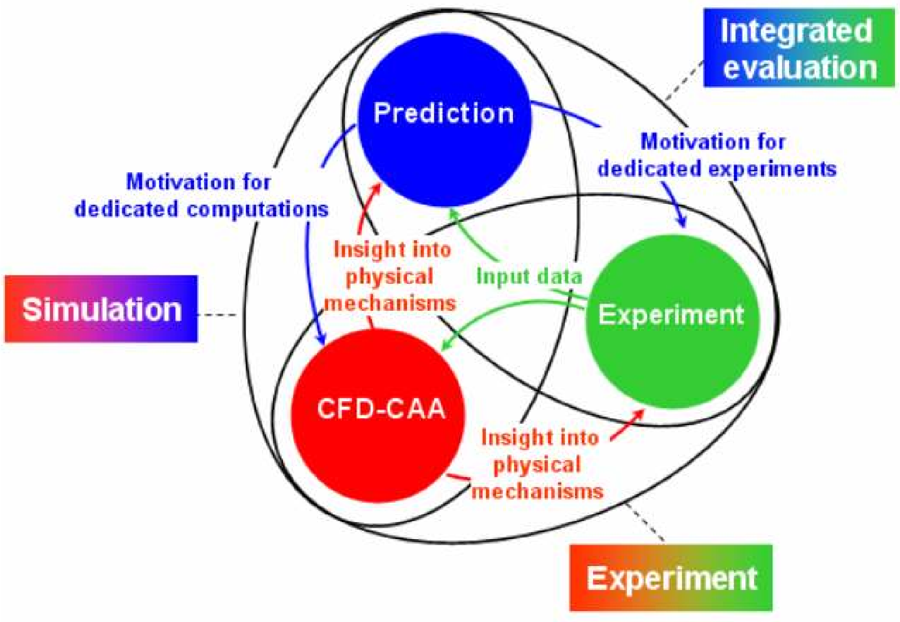

Source: Moreau e Enghardt (2008).

1.6 Research Framework and Objectives

The Department of Aeronautical Engineering of the São Carlos School of Engineering (EESC) at the University of São Paulo (USP), in partnerships with other Brazilian universities and Embraer S.A., has been part of the Silent Aircraft and SILENCE research projects. These projects have the objective of understanding aircraft noise and developing new technologies to mitigate this issue. As seen in Figure 6, these projects follow a trend spread around the world where, among others countries, the United States of America, the European Union, Japan, Russia, Canada, and Brazil are leading aeroacoustics research for the expansion of aircraft operation. At EESC-USP, SILENCE Project has two research teams (Fan and Airframe Noise) and in other universities Jet Noise, Liner Technologies are also studied. The author has been part of the Fan Noise team and has been part of the development of an experimental setup to investigate subsonic fan noise, the EESC-USP Fan Rig. The present dissertation, related to the Mechanical Engineering Graduate Program, results from the experimental study conduced in this workbench.

Figure 6: Noise abatement initiatives around the globe.

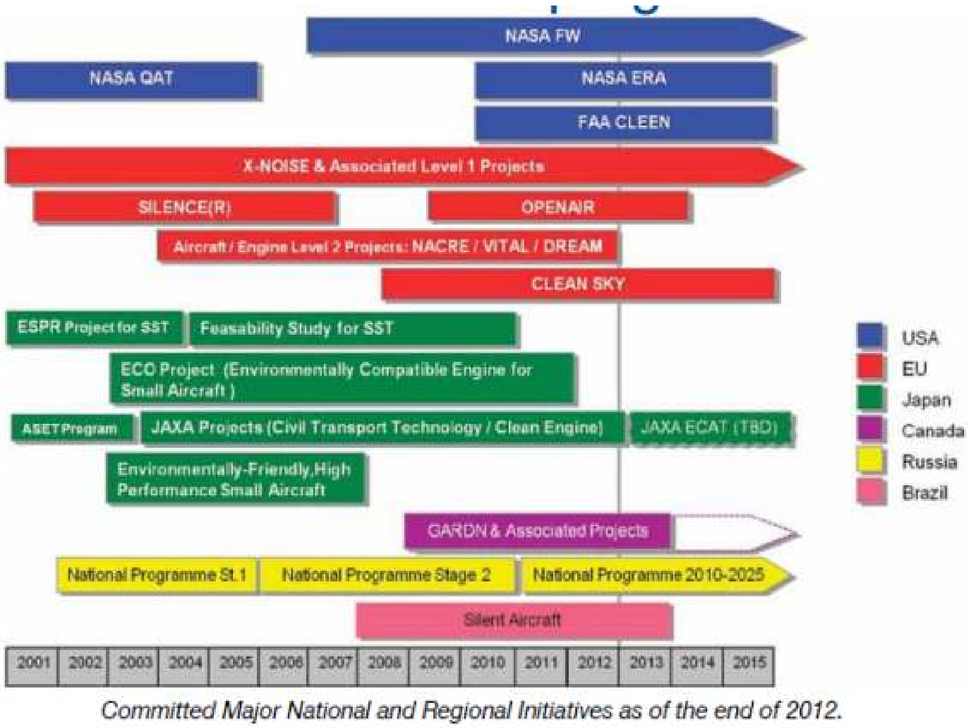

Source: ICAO (2013).

In this work, the focus remains in obtaining aerodynamic and acoustic experimental data from a subsonic fan installed in an aeroacoustics wind-tunnel and there are three main objectives. The first objective characterise the aerodynamic performance of the fan, which provides a better understanding of the flow that is generating noise. This is done by measuring flow quantities and electrical input power, in order to obtain characteristic curves of the fan in terms of volumetric flow rate, fan total and static pressure, compression ratio, fan air power and total efficiency. The second objective is to carry out a parametric campaign of experiments in the current fan rig configuration to state baseline measurements, such experiments are planned to isolate noise sources acting on a fan that can be due to several aerodynamic phenomena: inflow disturbances, inlet/casing boundary layer, potential field interactions, rotor-stator interaction, and others. This is done in terms of the effects of rotational speed, fan loading, inflow condition, and rotor-stator spacing. The third objective, aiming to further investigate the rotor-stator interaction source contribution to overall fan noise, is the design of an instrumented stator vane to record time histories of fluctuating pressures on suction side of one of the vanes on the stator ring and the analysis of the data collected to create insights on broadband noise generation. In summary, the main objectives for this dissertation are:

1. Fan Aerodynamic Performance Analysis
2. Parametric Study of Fan Noise Generation Mechanisms
3. Unsteady Surface Pressure Measurements and Analysis using an Instrumented Stator Vane

1.7 Outline of the Dissertation

This work is divided in seven main chapters, appendices and annexes. Chapter 2 provides an overview of relevant literature and related work and projects in the topic of this dissertation and also a brief discussion about noise, duct acoustics, and fan aeroacoustics. Chapter 3 contains the description of the experimental test bed and its capabilities, the instrumentation necessary for the acoustic and aerodynamic measurements, the experimental procedure, and the planned design of experiments of the three campaigns mentioned above (parametric, performance and instrumented stator vane). Chapter 4 contains the results from the performance campaign. Chapter 5 contains the results from the parametric campaign. Chapter 6 contains the results from the parametric campaign. Chapter 7 presents the main conclusions and further considerations of the developed work. Appendices contain extra information of the designed and manufacture components, tables which are to extensive for the dissertation body containing the tested points.

2 LITERATURE SURVEY

Aeroacoustics, the science of understanding of the phenomena generating noise in aircraft or any other vehicles or object moving in a fluid, is an imperative field to the development of new technologies, and, recently, an effort has been done to reduce the noise generated by the fan at the inlet and outlet of turbofan engines. This chapter contains an overview on acoustics and, more specifically, fan aeroacoustics literature that was relevant for the studies presented in this dissertation.

2.1 Papers of Historical Significance

The most modern aeronautical engines are the so-called turbofan engines, and the big difference for conventional turbojets - their predecessors - is the existence of a first stage with an enlarged diameter rotor, which admits more air and increases the efficiency of the propulsive system. Another advantage comes from the fact that air is divided between the one passing through the core and the one passing around it. The latter, in spite of its low speed, produces a reduction of the jet noise in the exhaust (SMITH, 1972).

The analytical modelling of the phenomena of noise generation and propagation are mostly based on the theory of acoustic analogy developed in the 1950' by Lighthill (1952), Lighthill (1954). This mathematical modelling is done by the rearrangement of the exact Navier-Stokes equations so that on one side the linear wave equation is obtained and on the other, modelled sources appear. The right hand side equation, shown below, acts as a source term and the Lighthill's stress tensor, T_{ij}, contains the information of the noise generation inside a region of the flow without necessarily explaining the generation mechanisms.

$$\frac{\partial^2 \rho'}{\partial t^2} - c_\infty^2 \frac{\partial^2 \rho'}{\partial x_i^2} = \frac{\partial^2 T_{ij}}{\partial x_i \partial x_j} \qquad T_{ij} = \rho v_i v_j + (p - p_\infty) - (\rho - \rho_\infty) c_\infty^2 \delta_{ij} - \sigma_{ij} \tag{2.1}$$

Curle (1955) extended the Lighthill formulation to include solid boundaries upon the sound field, by using Green's functions the solution of the wave equation can be found in terms of integrals that describe the convolution of noise sources distribution and propagation characteristics. This solution can be understood as the sum of three different types of acoustic sources, taken from linear acoustics: monopole, dipole and quadrupole sources.

$$\begin{aligned}\rho'(\mathbf{x},t)c_\infty^2 &= \left(\int\limits_S \left[\frac{\partial(\rho v_j)}{\partial\tau}\right]_{\tau=\tau^*}\frac{n_j dS(\mathbf{y})}{4\pi|\mathbf{x}-\mathbf{y}|}\right) + \left(-\frac{\partial}{\partial x_i}\int\limits_S [p_{ij}+\rho v_i v_j]_{\tau=\tau^*}\frac{n_j dS(\mathbf{y})}{4\pi|\mathbf{x}-\mathbf{y}|}\right)\\ &+ \left(-\frac{\partial^2}{\partial x_i \partial x_j}\int\limits_S [T_{ij}(\mathbf{y},\tau)]_{\tau=\tau^*}\frac{n_j dV(\mathbf{y})}{4\pi|\mathbf{x}-\mathbf{y}|}\right)\\ &= (\rho'(\mathbf{x},t)c_\infty^2)_{monopole} + (\rho'(\mathbf{x},t)c_\infty^2)_{dipole} + (\rho'(\mathbf{x},t)c_\infty^2)_{quadrupole}\end{aligned} \tag{2.2}$$

The expression presented above are general solutions for the wave equation for a medium that include objects that are not moving. In applications as turbomachinery noise, the movement of the surfaces are important and need to be taken into account. This problem was addressed by Williams e Hawkings (1969) that extended the Lighthill-Curle theory to include arbitrary convective motion and, later, by Farassat (1981) that developed linear formulas for the calculation of rotating blade noise, used for propeller and helicopter rotors noise using the solutions of the Ffowcs Williams-Hawkings (FW-H) equation.

Compared to open rotors, a suitable model for the geometry of a fan and a stator in a duct is harder to obtainm and, in this setup, sound sources due to different interactions appear. Among these new mechanisms of noise generation, most of the scientific effort was focused on to predict rotor-stator interaction, because it is the mechanism with the greatest power intensity, as mentioned by Huff (1997). Further details on the importance of this interaction and the latest challenges in fan aeroacoustics are explored in Peake e Parry (2012). This phenomenon is usually modelled by interaction between gusts and a cascade of airfoils (ENVIA et al., 2008). Nevertheless, in a review made by Laborderie e Moreau (2016) in fan noise prediction state-of-the-art, several solutions found for the problem are highlighted.

A first approach was developed based on the research developed in Carlson e Heins (1947), Heins e Carlson (1947) and Heins (1950), in which the authors used the formulation of the Green's functions together with a Fourier transform and the Wiener-Hopf technique to obtain an approximate solution for noise generated by the interaction between periodic wakes and a cascade of airfoils, considering them mathematically equivalent to electromagnetic waves reflection and transmission by a set of infinite parallel plates. Later, Mani e Horvay (1970) used the Fourier transform and the Wiener-Hopf technique in a dual formulation of the integral equation, instead the Green's functions, to find the solution for the sound reflection and transmission through a line of airfoils. Many other authors have extended this methodology that uses the closed solutions of the Wiener-Hopf technique, among them Koch (1971), Glegg (1999), and Posson, Moreau e Roger (2010).

At the same time, the first studies of non-stationary aerodynamics, necessary for the modelling of this rotor-stator interaction with acoustic applications, without the need for an analogy, were drawn up in Sears (1941). Then Kemp e Sears (1953) developed an aerodynamic model for interference rotor-stator and raised two important interactions: the interaction between the potential fields and the interaction of the upstream (rotor) airfoils wake with the downstream airfoils (stator), but they found out that the second type becomes more relevant to spacings between the cascades greater than a tenth of the blade chord. Shortly after, Kemp e Sears (1955) were able to estimate the oscillations in blade loading due to viscous wakes. Based on these models, Mani (1970), who already worked with the closed solution by the Wiener-Hopf technique, developed a methodology to predict the acoustic energy in the blade passing frequency (BPF) and its harmonics making a linearization of the Lighthill's equations.

Kaji e Okazaki (1970b) formulated the problem of the flat and rectilinear plates cascade and they solved it by the method of potential acceleration. Then, based on the work of Kemp e Sears (1953), Kemp e Sears (1955), they were able to make a prediction of noise generated by the interaction between rotor and stator (KAJI; OKAZAKI, 1970a). From the work of Kaji e Okazaki (1970b), Whitehead (1970) and Smith (1972) used the blade elements approximation to make non-stationary aerodynamic representation, in which the blades are represented as a set of two-dimensional flat plates cascades, stacked in the radial direction and made the first computational models of this interaction considering some three-dimensionality. Namba (1977) developed a three-dimensional lifting surface model and discussed the fact that as the acoustic response frequency increases, the three-dimensional effects become less important for a given gust wave number in the span direction. This phenomenon was confirmed by Kobayashi (1978) and Kobayashi e Groeneweg (1980).

Finally, another approach was developed by Goldstein (1976). He described the sound generated by the interaction between a viscous wake and a cascade of airfoils and managed to model this phenomenon by developing Green's functions for a fan inside an infinite duct with constant axial velocity. Ventres, Theobald e Mark (1982) then used these Green's functions developed by Goldstein to numerically calculate the unsteady loading, considering a distribution of acoustic sources in the stator blades and their radiation in the annular duct to model the generation of fan noise.

2.2 Papers Under the Same Topics

Experimental fan aeroacoustics and each of the effects that will be explored in this dissertation have started to be tested after the 60s mainly by NASA and aircraft engine manufacturers. Regarding to rotor-stator spacing, there were some investigators that proposed expressions for tone level as function of non-dimensional spacing (x/c). Some investigators suggested a relation of 4-dB per doubling up to 1 chord spacing and

2-dB thereafter (LOWSON, 1968), others suggested 6-dB per doubling (BALOMBIN; STAKOLICH, 1974). Woodward e Glaser (1981) showed that cut-off criterion strongly affects the fundamental tone and other tones showed good agreement with the 6-dB criterion. Broadband showed little change with rotor-stator spacing in these experiments. Goldstein, Glaser e Coates (1972) showed the effect of the casing boundary layer on fan noise, with a small increase in blade passing tone and a stronger effect for subsonic fans. Broadband noise is more affected and reductions of as much as 7-dB can be achieved under special circumstances. Gliebe e Kantola (1983) studied the effects of spacing and vane/blade ratio. They found that, for high vane/blade ratio, the third harmonic is greater than the second harmonic and spacing has a greater effect on higher harmonic tones, which drop more rapidly as spacing is increased and push the energy to the second harmonic. For a ratio close to unity, the second harmonic is dominant in close spacings and as spacing increases the spectrum peak shifts to the first harmonic.

Regarding to the simulation of flight conditions, Lowrie (LOWRIE, 1975) gives three possible causes for differences in noise measured for static and flight conditions: (1) Modifications of the annular boundary layer on nacelle inlet; (2) Ingestion of vortices generated on the ground; (3) Differences in ingested atmospheric turbulence for each case. The author states that, from the experience he gained at Rolls-Royce, the change in boundary layer thickness and in ingested turbulence are the most important factors for flight effects on noise generation. The author also states that the flight effects on noise may be well reproduced for static tests by reducing ingested turbulence, controlling the boundary layer and the Mach number gradient between intake and rotor. The first can be controlled by a well designed ICD (Inlet Control Device). A flight test program utilising a JT15D-1 turbofan engine has been conducted with the objectives of studying flight effects on fan noise (PREISSER; CHESTNUTT, 1983). The study showed that the use of an ICD helps to simulate the in flight noise level of the first BPF. That similarity, however, does not apply to neither the broad band noise and multiple-pure-tone harmonics.

The NASA Glenn Research Center (GRC) has been part of several programs aiming to reduce the noise generated by turbofan engines in aircrafts. More spefically they have, in the early 1990's, built the Advanced Noise Control Fan (ANCF) test bed which is a unique, large diameter, low speed, axial fan to evaluate noise reduction concepts (as active noise control), general fan aeroacoustics research and to provide experimental data to numerical simulation verifications (HEIDELBERG et al., 1996). Among several scientific publications, Sutliff et al. (1996) took one of the first steps taking baseline measurements of the fan aeroacoustics in spectral and modal forms, to which the new concepts could be compared to. Also, Bozak (2009) took flow measurements in order to obtain aerodynamic performance of the tested fan and developed a method of inferring these quantities only from wall static pressures. Sutliff, Heidelberg e Envia (1999) also developed a instrumented stator vane to measure unsteady pressures on vane suction and pressure sides and compare measured modes from modes predicted using the proper integration of these pressures and uniform-flow annular-duct Green's functions.

Following the ANCF, NASA GCR launched the Fan Noise Source Diagnostic Test (SDT), a test for assessing the noise characteristics of three outlet guide vane designs, in which they were able to identify broadband noise sources with the use of advanced measurement methods. Hughes et al. (2002) took flow measurements to check the effect the outlet guide vanes had on the fan performance, in order to make the two conditions match, so that acoustic sources are not affected. Woodward et al. (2002) used wall sound pressure levels measured in three rings of microphones in the aft duct walls to obtain the spinning modes to test broadband noise prediction codes. Heidelberg (2002) took tone mode measurements of circumferential and radial order, created by rotor-stator interaction or rotor-locked modes, when in sonic condition, and the effect of the vane sweep and solidity on them. Envia (2002) took measurements from a instrumented stator vane, designed for the stator of this new test bed, decomposed the measurements in coherent and non-coherent component and observed, for a increasing fan rotational speed, a linear increase of average broadband level (in dB), a decreasing function of integral length scale and homogeneity of broadband pressure distribution over the vane.

Under the European PROBAND Project, the German Aerospace Centre (DLR) also launched a laboratory scale fan rig for the development of new measurement techniques and generation of data for CFD and semi-analytic prediction models validation. DLR's Low Speed Fan Rig, WP3, is located in their unit in Berlin and it is one-stage low speed fan rig for aerodynamic and acoustic measurements with the aim of investigating the broadband noise generation mechanisms in a ducted. In their Rig, they have conducted studies on broadband noise and rotor-stator interaction sources (MOREAU; ENGHARDT, 2008; MOREAU; ENGHARDT, 2009; ENGHARDT; NEUHAUS; LOWIS, 2004; ENGHARDT; HOLEWA; TAPKEN, 2007).

2.3 Papers Under the Same Project

The EESC-USP Fan Rig was first assembled in 2014 and the first experimental results were published by Caldas et al. (2015), in which his beamforming technique for a wall mounted-antenna of microphones was explained and a first mode detection was tested. This results were also published in his dissertation (CALDAS et al., 2016a) and were expanded in Caldas (2016), Caldas et al. (2016b). Cuenca, Caldas e Greco (2016), Cuenca (2017) have proposed and tested a new meta-model approach for parametric analysis and the author has published a first set of baseline measurements, which is also present in this dissertation (MARTINEZ et al., 2017a). More recently, the author has published the results from the instrumented vane campaign (MARTINEZ et al., 2017b) and Cuenca, Martinez e Greco (2018) extended his meta-model analysis.

3 EXPERIMENTAL SETUP AND INSTRUMENTATION

The EESC-USP Fan Rig is a test facility to investigate fan noise sources at the Department of Aeronautical Engineering of the São Carlos School of Engineering at the São Carlos campus of the University of São Paulo, where the tests were ran. The facility, that can be seen in Figure 7, provides a flexible configuration that allows changes in operational conditions of the rig that tries to isolate the sources as much as possible. This chapter contains the description of the EESC-USP Fan Rig test facility, its capabilities, the setup and the instrumentation that were used for collecting the data present in this work.

Figure 7: The EESC-USP Fan Rig.

Source: Elaborated by the author.

3.1 The EESC-USP Fan Rig

The object of analysis of this dissertation is the aeroacoustics phenomena resulting from experiments in the EESC-USP Fan Rig. This facility is an aeroacoustics wind-tunnel located at the Department of Aeronautical Engineering of the University of São Paulo at São Carlos School of Engineering. It contains a rotor-stator assembly, to simulate a scaled-down version of the fan of an aircraft engine. The rig is composed by a long duct (more than ten meters long) with its axis positioned 1.3 m above the floor over a metallic workbench. The duct radius at the inlet and the outlet has a diameter of 0.6 m, and at the fan-stator stage there is a contraction to a diameter of 0.5 m, which was done aiming the reduction of the casing boundary layer. At the inlet there is a glass-fibre bell-mouth installed, with an asymmetric elliptic curvature geometry decreasing from 1.36 m to 0.6 m, this provides a smoother air inflow, avoids separation and reduces non-uniformities entering the duct.

Figure 8: Anechoic termination.

Source: Elaborated by the author.

The design philosophy for the ducts was inspired on DLR's test facility (ENGHARDT; HOLEWA; TAPKEN, 2007) and consists of a very long, hard walled, duct with flow treatments in both its inlet and outlet. There was a major concern in isolating the noise generation of the fan assembly from other possible noise sources. This explains the choice for long ducts, pushing the boundaries far from the acoustic generation phenomena, and reducing the effect acoustic reflections at both ends of the tunnel. A special care was taken to acoustically isolate the fan section from the outlet, where there is an abrupt change in duct acoustic impedance, and in flow condition, where an internal flow becomes a jet flow. An anechoic termination, seen in Figure 8, was then installed in the outlet following the design recommendations of the ISO 5136 standard. Each of this device chambers work as a resonator, damping some frequency bands and, overall, the device reduces the sound wave reflections at the exhaust back to the duct. In the inlet, however, the concern regarding sound reflection is not that important since there is no abrupt change in duct area, nonetheless there is a preoccupation with the inflow conditions.

As the ducts are installed close to the ground, the ingested flow is influenced by the increased turbulence level and by the asymmetries generated by the proximity to the ground floor, like the alteration on the potential flow and the appearance of a ground vortex. These flow distortions are believed to have a significant effect on the noise and bring the fan away from flight condition. A device (called here Inlet Control Device or ICD) was placed in it to mitigate inflow distortions and non-uniformities and to reduce ingested turbulence levels, providing an approximation to flight condition. The Inlet Control Device (ICD) is located at the duct inlet where an elliptical bell-mouth is installed. It is a dome-shaped structure, inspired on that described by Homyak (HOMYAK; MCARDLE; HEIDELBERG, 1983), but, for now, with the main the objective being achieving a turbulence reduction, we are only using a steel wire mesh, with a porosity of about 60%. The fan is driven by a Remy HVH-250-115 DOM 100-hp electrical motor (Figure 9) which is mounted inside the duct, supported by three struts, and is capable of reaching speeds up to 5000 rpm.

Figure 9: Remy HVH-250-115 DOM 100-hp electrical motor and rectifier.

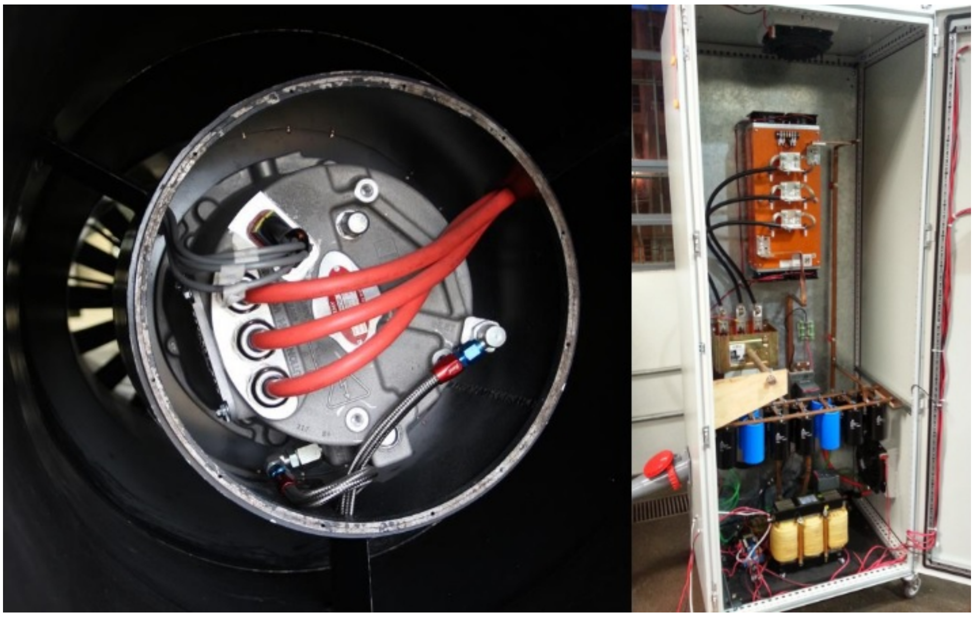

Source: Elaborated by the author.

3.1.1 The ANCF Fan and Stator Geometries

The fan stage tested in the EESC-USP Fan Rig is a scaled-down replica of the Advanced Control Noise Fan (ANCF) at the Aeroacoustic Propulsion Laboratory facility at NASA Glenn. This rig was developed in the early 1990s to evaluate noise reduction concepts as, for example, vanes trailing edge blowing or soft/porous vanes, and, there, several geometries were tested. At the EESC-USP Fan Rig, the 16-blades rotor (Figure 10a), 14-vanes stator (Figure 10b) was the geometry reproduced. The fan and stator diameters are 0.5 meters, the rotor blades have an manually adjustable pitch, and the stator vanes are fixed. In the tests presented here, the pitch is also held constant. The spinner has a ellipsoid geometry and the hub has a constant diameter of 0.2 meters. Neither the blades nor the vanes have much camber or twist from hub to tip and their thickness is approximately constant. Table 2 shows main dimensions of the fan and stator.

Figure 10: EESC-USP Fan Rig rotor and stator geometries.

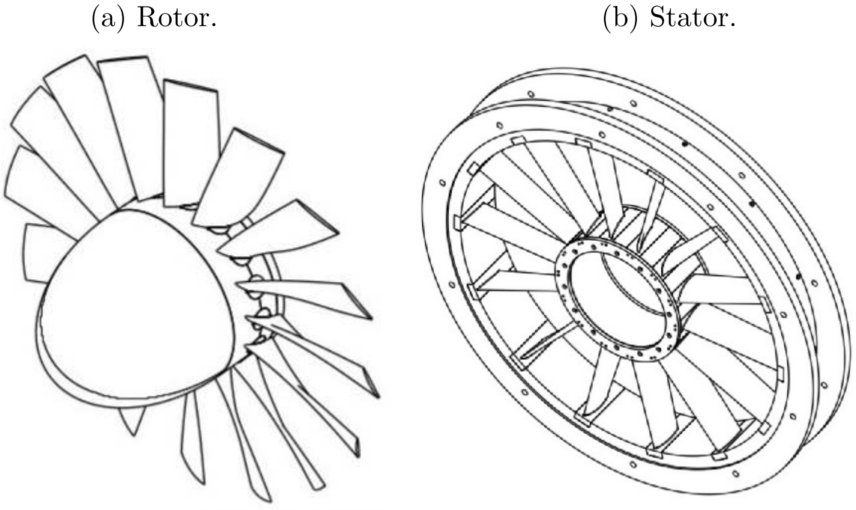
(a) Rotor.

(b) Stator.

Source: Elaborated by the author.

Table 2: Rotor-stator dimensions.

Parameter	**Dimension [mm]**	**Parameter**	**Dimension [mm]**
Fan Diameter	500	Vane Chord at Tip	56.5
Duct Diameter	502	Vane Chord at Hub	56.9
Average Tip Gap	1	Mean Vane Chord	56.7
Blade Chord at Tip	56.5	Rotor-Stator Spacing at Tip	32.5
Blade Chord at Hub	56.9	Rotor-Stator Spacing at Hub	15.7
Mean Blade Chord	56.7	Mean Rotor-Stator Spacing	24.1

Source: Elaborated by the author.

3.1.2 Adjustable Parameters

The EESC-USP Fan Rig has been designed to have the possibility of adjusting some of the operational and geometric parameters of the flow. The main controllable parameters up to the date of the experiments described in this dissertation are: (1) fan speed, (2) throttling, (3) rotor-stator spacing, and (4) inflow condition. Fan speed is set by a software that controls the electrical motor inverter, it was constrained to 4500 rpm, speed in which the fan was capable of producing axial flows up to Mach 0.14 and tip speeds of around Mach 0.37 and still showed acceptable levels of vibration.

Throttling can be set by installing interchangeable screens (Figure 11) in the duct exhaust section, obstructing the flow to the hangar outside, increasing the pressure

Figure 11: Throttling screen installed in the duct exhaust (outside of the hangar).

Source: Elaborated by the author.

downstream to the fan and, therefore, controlling fan loading (since the reduction of axial speed of the flow changes the angle of attack of the rotor blades). These screens were fabricated to have different area restrictions compared to the open outlet area (600 mm diameter duct). For this device fabrication, the international standard ISO 5136 recommendations were used, with some small modifications. The fabricated screen area restrictions were: 0.0% (no screen), 24.3%, 37.7%, 52.2%, 63.0%, 74.7%., but, for sake of simplification, these screen areas are marked on the plots below as 0%, 25%, 40%, 50%, 60%, 70%. Table 3 with true and approximate area restriction is shown below.

Table 3: Throttling Plates Configurations.

Configuration	**True Area Restriction** [%]	**Approximate Area Restriction** [%]
1	0	0
2	24.3	25
3	37.7	40
4	52.2	50
5	63.0	60
6	74.7	70

Source: Elaborated by the author.

Rotor-stator spacing was changed by increasing shaft and hub length between rotor and stator using shaft extensions (spacers) that were manufactured so that at least three configurations could be tested. These manufactured parts can be seen in Figure 12. In

Figure 12: Rotor-stator spacing manufactured parts.

(a) Hub extension. (b) Shaft extension.

Source: Elaborated by the author.

chord spacing (here defined as the mean distance between rotor blade trailing edge and the vanes leading edge, divided by the rotor blade mean chord) three configurations that were designed are: (0) 0.43, (1) 0.95, and (2) 1.5. Table 4 with rotor-stator spacers configuration is shown below.

Table 4: Rotor-stator spacers dimensions.

Configuration	**Spacers**	**Rotor-Stator Spacing [mm]**	**Rotor-Stator Spacing [mm/mm]**
0	None	24.1	0.43
1	1	54.1	0.95
2	2	84.1	1.48

Source: Elaborated by the author.

Finally, inflow conditions were controlled by installing devices to control turbulence level: beyond the regular configuration (0), a reduced turbulence condition configuration (1), with the installation of an inlet control device (ICD), and an increased turbulence condition configuration (2), with the installation of a turbulence generator (TG) grid in the duct intake section were studied. The different configurations can be seen in Figure 13.

3.2 Instrumentation

An overview of the instrumentation present in the current configuration of the EESC-USP Fan Rig. From left to right, the air goes from ambient condition (A), enters

Figure 13: Inflow configurations.

(a) No device.

(b) ICD.

(c) TG.

Source: Elaborated by the author.

the duct through the Inlet Control Device. Then, it gets accelerated in the bellmouth. In the inlet ducts there are the inlet microphone antenna, the inlet static pressure taps (1) and the inlet Pitot tube. The air gets contracted once more and then it gets pumped by the fan. Near the fan assembly, there are static pressure taps upstream to the fan (a), between fan and stator (b) and downstream to the stator (c). The pumped air circumvents the electrical motor then enter the exhaust duct. In the exhaust duct there are another Pitot tube and the outlet static pressure taps (2), the anechoic termination and free space downstream again.

Figure 14: Instrumentation setup overview.

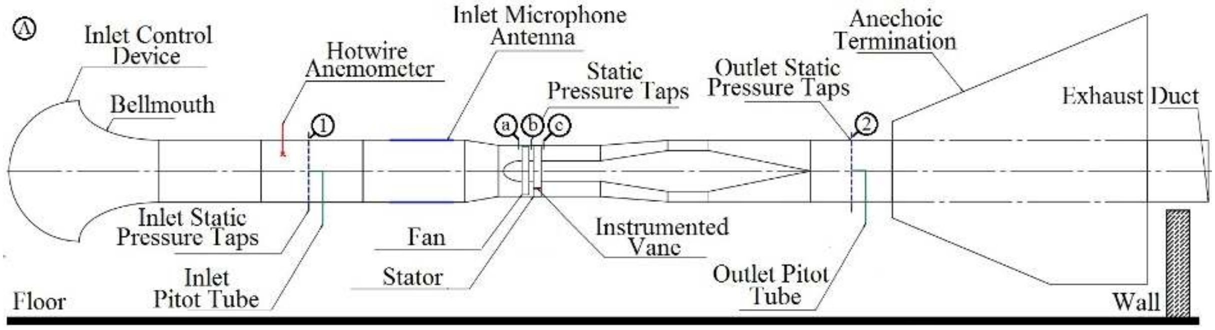

Source: Elaborated by the author.

There are two main instrumentation systems in the workbench: one of simultaneously high acquisition frequency that accounts the acoustic measurements, and one for low acquisition frequency which is responsible for the pressure, vibration and safety measurements. The first system of acquisition is done using a NI PXI-1042Q chassis (Figure 15a), and NI 4496 and NI 4498 module boards. They are connected to a computer via optical fiber (due to the high acquisition frequency) and the acquisition software was developed by Federal University of Santa Catarina, in Brazil. The second acquisition system used is the NI cDAQ-9184 (Figure 15b). The cDAQ is connected to a PC via Ethernet and the acquisition is done using Matlab and Labview.

Figure 15: Acquisition systems.

(a) NI PXI-1042Q chassis with microphones cabling.

(b) NI cDAQ-9184.

Source: Elaborated by the author and from manufacturers website.

3.2.1 Acoustic Measurements System

Acoustic measurements were taken from two sources: an antenna array of microphones mounted in the inlet of the duct, and the microphones embedded in one of the stator vanes. The use of microphones allows obtaining the generated noise spectrum, modal decomposition of the acoustic field in the duct and performing a beamforming analysis - a technique used to find spatial sources of noise. The high frequency system has the acoustic measurements carried out with free-field array Microphones G.R.A.S. 40PH-S2 ϕ7 mm and B&K Type 4958 ϕ 7 mm (Figure 16). These are microphones with great accuracy in phase match and frequency bandwidth from 20 Hz to 20 kHz and a dynamic range of 135dB (SPL), therefore being ideal to the fan noise measurements. The microphones are regularly calibrated to ensure acoustic accuracy and are then distributed on an antenna upstream of the rotor.

3.2.1.1 Inlet Microphone Antenna

An antenna of microphones - disposed in three circumferential rings - was used to capture the sound pressure in the duct walls upstream to the fan and the full description of this system can be seen in (CALDAS et al., 2015; CALDAS et al., 2016a; CALDAS, 2016; CALDAS et al., 2016b). Aiming the determination of the sound power radiated across the duct, this arrangement of flush-mounted microphones is set as three rings, with 33, 23 and 21 equally distributed microphones in each ring. The first ring, with 33 microphones, is at an spacing of 0.70 m upstream from the fan, the next is away 0.10 m from the first and the

Figure 16: Microphones.

(a) Microphone G.R.A.S. 40PH-S2 ϕ7 mm.

(b) Microphone B&K Type 4958 ϕ 7 mm.

Source: From manufacturers websites.

third is 0.17 m away from the second. The schematics of the microphones positions and the assembled antenna can be seen in Figure 17. The design of a microphone antenna should take into account some important aspects such as: bandwidth, focal length of possible sources, duct diameter, number of blades of the rotor / stator assembly. This last parameter is of great importance, since the tonal components of generated fan noise are excited in acoustic modes directly connected to the number of rotor/stator blades (TYLER; SOFRIN, 1962). Finally, the number of sensors per ring is related to the maximum circumferential order of the modes capable of detecting (LOWIS, 2007; CALDAS et al., 2015). The need for multiple rings is given by the detection of radial modes.

Figure 17: Inlet microphone antenna.

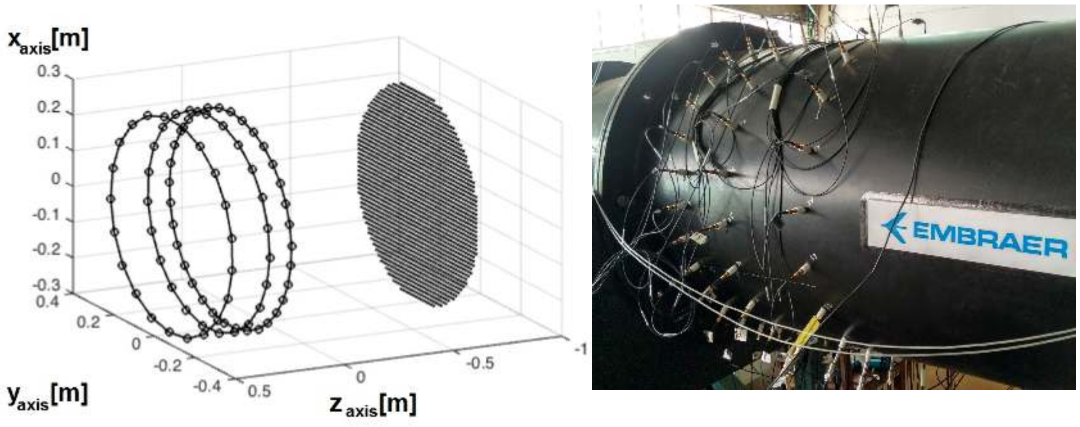

(a) Microphone array positions.

(b) Assembled antenna.

Source: Elaborated by the author.

3.2.1.2 Instrumented Stator Vane

Aiming to further investigate how rotor-stator interaction contributes to overall fan noise, an instrumented vane (Figure 18a) was installed to record time histories of fluctuating pressures on suction side of one of the vanes on the stator ring.To do so, a 3D-printed PLA vane was designed to hold an internal flexible circuit board with 21 SPM0406HE3H-SB surface mounted MEMS microphones (Figure 18b) . The microphones are installed in a flexible circuit board (FCB), which in addition to transmitting the signal, has an interface circuit to supply power to the microphones. The circuit is going to be covered with a cap which will have pressures where the transducers are going to be located. Microphones data will be acquired with a NI PXI-1042Q chassis and NI 4496 and NI 4498 data acquisition modules, with which data will be acquired simultaneously at a sampling rate of 128 kHz and 60 seconds of duration. Microphones are distributed both chord and span-wise, so that correlations can be taken in both directions. The recorded time histories of unsteady pressure will provide a signal containing both changes in pressure due convection and sound.

Figure 18: Instrumented stator vane system.

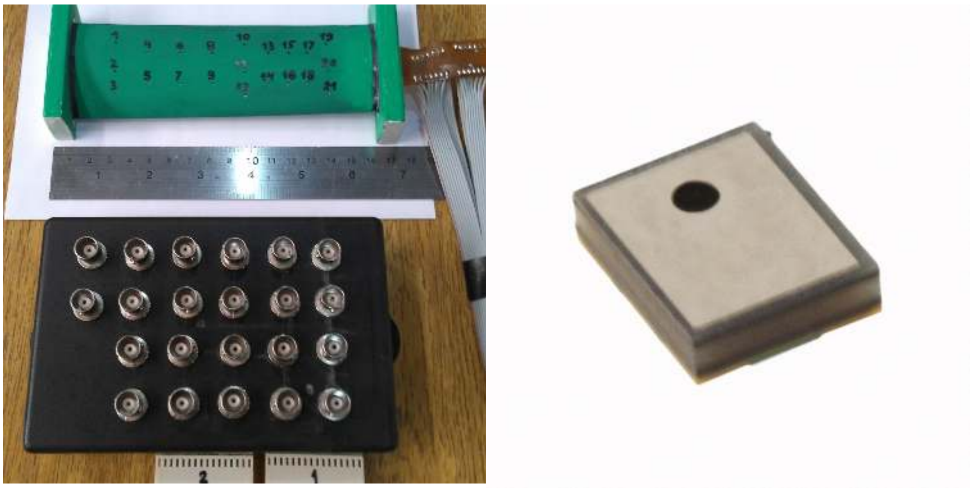

(a) Instrumented stator vane.

(b) SPM0406HE3H-SB.

Source: Elaborated by the author.

3.2.2 Flow Measurements System

Flow measurements are essential to determine how the parameters variation in the EESC-USP Fan Rig configurations affect fan aerodynamic performance, that can be accessed by estimating the mass-flow rate in the wind-tunnel and the increase in total pressure due to addition of energy provided by the fan. To estimate these parameters a series of measurements must be taken. The most straightforward measurements are the ambient properties denoted by the subscript “A”, as seen in Figure 14. Ambient temperature in Celsius (T_A), ambient pressure (p_A), and humidity (h_A) are measured using a meteorological station, an Instrutemp's Model IVWH 1170 Meteorological Station (Figure 19b). According to the standard, ambient pressure and humidity measurements should be taken at mean altitude between centres of fan inlet and fan outlet, and temperature measurements should be taken near fan inlet, these conditions are respected with the use of the portable meteorological station instrument. Humidity measurement has an accuracy of ±5% and temperature accuracy is of ± 1 °C, which are greater than ± 0.2% and ± 0.5 °C recommended by the standard. Ambient pressure pressure precision is of 1.5 hPa, which corresponds to 0.16% of the full scale, smaller than the 0.2% recommended by the Standard.

In any given airway section the average pressure can be measured by installing static pressure taps in duct wall of this section. In the case of cylindrical airways, the Standard recommends four tappings equally spaced around the duct circumference, and then they can be connected to a manometer each or connected altogether to a single manometer. These static pressure tappings can be constructed by simply drilling holes on the duct walls, with diameter no less than 1.5mm. In the Fan Rig, they were constructed separately and screwed to the duct walls, and the bore diameter is 1.5mm (see Figure 72). Two of these static pressure rings were installed in the Fan Rig, in the inlet and in the outlet duct (stations 1 and 2 in Figure 14). Also, three less intrusive tappings, not circumferentially distributed, were bore near the fan, one upstream to the fan, one between fan and stator, and one downstream to the fan (stations a, b and c in Figure 14).

Static pressure is measured in several positions: at the inlet, before the fan, between fan and stator, after stator and at the outlet; dynamic pressure is measured at the inlet and the outlet. Average pressure in airway sections 1, a, b, and c (from Figure 14) are measured using TSI's DP-CALC Micromanometer 8705 (from Figure 19a). These micromanometers have differential transducers by leaving their second port open to atmospheric pressure, we obtain gauge pressures $p_{e,1}$, $p_{e,a}$, $p_{e,b}$, and $p_{e,c}$. These micromanometers have accuracy of 1%, as recommended by the Standard for differential manometers. Outlet static pressure tapping measurements ($p_{e,2}$) are done individually using SensorTechnics' HDI Series Amplified 10-mbar gauge pressure sensors , also of acceptable accuracy (0.5%). These sensors are connected to a signal conditioning circuit and the acquisition is done using the cDAQ-9184.

Determination of flow rate can be done using one of four methods, described in the Standard: multiple nozzle, conical or bellmouth inlet, orifice plate and Pitot-static tube traverse. In this Rig, we have chosen to use the Pitot-static tube option. The Pitot tube probe used was a Dwyer Series 160E Ellipsoidal Tip Pitot Tube that is in conformity with ISO Standard 3966. The outlet Pitot tube was fixed, since its main attribution was to capture total pressure. The inlet Pitot tube main attribution was to map the dynamic

Figure 19: Flow instrumentation.

(a) DP-CALC Micromanometer 8705.

(b) IVWH 1170 Meteorological Station.

Source: Elaborated by the author.

pressure across the inlet section, whose positions are described in Table 6, and calculate the inlet average dynamic pressure ($p_{d,1}$). These pressures were measured using SensorTechnics' HDI Series Amplified 10-mbar differential pressure sensors, also of acceptable accuracy (0.5%).

3.2.3 Other Measurements

Other relevant measurements are the fan rotational speed and the power input. The rotational speed is controlled via the motor software and is shown in the controller software. It is also measured using a Hall sensor, whose signal is acquired simultaneously to the microphones. Power input of are measured prior to the motor inverter, where there is a electrical meter: it shows the input voltage (which is constant and set to 556 V) and input current. Finally, vibration is measured with accelerometers installed at the stator and the motor bedding.

4 FAN PERFORMANCE CAMPAIGN

4.1 Introduction

The knowledge of performance curves is necessary to understand the characteristics and capabilities of different fan equipment and can help with the selection of new fan types and sizing. Also it assures stable and efficient operation as well as enables predictions of the wind-tunnel behaviour and, therefore, shorter and acoustic-dedicated experiments. An extensive campaign of experiments was taken to analyse the performance characteristics of the scaled-down ANCF geometry used in the EESC-USP Fan Rig. These experiments consisted of Pitot tube traversing - measuring dynamic pressure in a set of radial and circumferential positions-, static pressure measurements in several sections of the ducts, ambient pressure, temperature and humidity measurements, input electric power measurements, and fan speed measurements, that, altogether, make possible to calculate the performance quantities.

4.2 Data Processing

The following formulation and notations are based on what is presented in ISO5801 (2007). This standard explain how to build or classify a workbench for measuring fan performance and shows how the flow measurements taken during the experiments can be translated in performance quantities.

4.2.1 Determination of Performance Quantities

When carrying out low-pressure fan tests and using standardised conditions, the air velocity can be considered sufficiently low so that its influence on parameters such as pressure, temperature and density can be neglected. The Mach number of 0.15 and fan pressure less than 2000 Pa are considered as the limits above which this distinction shall be made, because, below these values, the difference between the gauge stagnation pressure, $p_{sg,x}$, at an arbitrary section, denoted by the subscript “x”, of the test airway, and the total pressure, $p_{t,x}$, is very small.

The meteorological station, described in Chapter 3, provides the ambient temperature, T_A, ambient pressure, p_A, and ambient humidity, h_A. The temperature for each measurement should be expressed in Kelvin, according to:

$$\theta_A = T_A + 273.15 \tag{4.1}$$

As the air velocity in the duct does not exceed the reference Mach number for operating range of the fan installed in the EESC-USP Fan Rig, the air flow through the fan and the test airway is considered as incompressible and at same temperature in all sections. This means that the following relations can be considered:

$$\rho_A = \rho_x = \rho_{sg,1} = \rho_{sg,2} \tag{4.2}$$

Temperature is assumed to be constant across the duct, in a manner that $\theta_x = \theta_A$ and they are both constant for each of the tests.

$$T_A = T_x = T_d = T_1 = T_2 \tag{4.3}$$

Therefore, the ambient air density, in kg/m^3, can be obtained from the ambient pressure and the vapour pressure, p_v:

$$\rho_A = \frac{p_A - 0.378 p_v}{287\theta_A} \tag{4.4}$$

The vapour pressure, by its turn, should be obtained using the ambient humidity and saturation pressure which is a function of the ambient temperature as shown in the following formulas.

$$p_v = h_A (p_{sat})_{T_d} \tag{4.5}$$

$$(p_{sat})_{T_d} = 610.8 + 44.442 T_d + 1.4133 T_d^2 + 0.02768 T_d^3 + 2.55667 \times 10^{-4} T_d^4 + 2.89166 \times 10^{-6} T_d^5 \tag{4.6}$$

The dynamic viscosity, in Pa.s, as long as the temperature is within the range from -20 °C to +100, can be obtained with the formula:

$$\mu = (17.1 + 0.0048 T_A) \times 10^{-6} \tag{4.7}$$

The kinematic viscosity, in m^2/s, is given by:

$$\nu = \frac{\mu}{\rho} \tag{4.8}$$

If the gauge static pressure is measured from a hose that connects multiple tappings, the average static pressure is directly obtained, else, if each tapping is measured using a separated transducer, the pressures should be averaged using the following relation:

$$p_{e,x} = \frac{1}{N_{taps}} \sum_{j=1}^{N_{taps}} p_{e,x}^{(j)} \tag{4.9}$$

Adding the ambient pressure to the gauge value gives the section total static pressure, p_x:

$$p_x = p_{e,x} + p_A \tag{4.10}$$

The local velocity should be measured at a number of positions across a duct and the individual velocity values combined, using an averaging technique, to yield an estimate of the mean velocity in the duct. Measurement of the cross-sectional area of the duct in the traverse plane then allows calculation of the flow rate Measuring the dynamic pressure in K predefined positions, as $p_{d,x}^{(k)}$, we can average them out and have a mean dynamic pressure value, $p_{d,x}$

$$p_{d,x} = \left[\frac{1}{K} \sum_{k=1}^{K} (p_{d,x}^{(k)})^{0.5} \right]^2 \tag{4.11}$$

$$V_{m,x} = (2\rho_x p_{d,x})^{0.5} \tag{4.12}$$

The geometric parameter D_x is assumed to have no error and it is used to calculate the duct section areas A_x. In the absence of leakage, q_m is constant throughout the airway system and it is calculated using the following expression:

$$q_m = \frac{V_{m,x}}{A_x} \tag{4.13}$$

From the mass-flow (q_m) we can calculate the volume flow ($q_{Vsg,1}$)

$$q_{Vsg,1} = \frac{q_m}{\rho_{sg,1}} \tag{4.14}$$

The stagnation pressure and total pressure can be considered equilavent for velocities as low as 0.15 Mach and, therefore, the stagnation pressure in a determined duct section, in Pa, can be obtained using the following relation:

$$p_{sg,x} = p_x + p_{d,x}, \tag{4.15}$$

where $p_{d,x}$ is the dynamic pressure in the same section, obtained from the averaged velocity of the flow.

$$p_{d,x} = \frac{1}{2}\rho_x V_{m,x}^2 \tag{4.16}$$

The fan pressure, p_f, is defined as the difference between the stagnation pressures downstream ($p_{sg,2}$) and upstream ($p_{sg,1}$) to the fan. It denotes the pressure rise provided by the rotor. It is obtained using the following formula:

$$p_f = p_{sg,2} - p_{sg,1} = p_{e,2} + p_{d,2} - (p_{e,1} + p_{d,1}) \tag{4.17}$$

The static fan pressure, p_{sf}, is the fan pressure decreased from the dynamic pressure in the airway.

$$p_{sf} = p_2 - p_{sg,1} = p_f - p_{d,1} \tag{4.18}$$

The compression ratio, r, is given by:

$$r = 1 + \frac{p_f}{p_{sg,1}} \tag{4.19}$$

The fan air power, P_u, is the energy transferred to the fluid with the fan. It takes into account the volume-flow ($q_{Vsg,1}$) and the fan pressure (p_f). It can be calculated by the following equation:

$$P_u = q_{Vsg,1} p_f \tag{4.20}$$

Power input is essential for determination of the fan efficiency calculation. power supplied to the fan can be obtained in several positions of the supply tree. There are four main power input types of measurement: (1) motor input power - electrical power supplied at the terminals of an electric motor drive (P_r) -, (2) motor output power - shaft power output of the motor -, (3) fan shaft power - mechanical power supplied to the fan shaft -, and (4) impeller power: mechanical power supplied to the fan impeller. In this work, the only measurement of power supplied to the fan is an electrical meter in the inverter that measures input current and voltage. Voltage is held constant at 556 V and current will vary for each test. The average motor input power can be calculated by the following equation:

$$P_r = Ui \tag{4.21}$$

where U is the inverter DC input voltage and i is the average inverter input current, in A.

4.2.1.1 Efficiency Calculation

Efficiency is an important parameter to investigate how much energy is actually being transferred to the fluid in form of pressure and mass-flow. Therefore, it is a ratio between the output power and the input power. In our experiments, only the electrical output power can be assessed and, therefore, only the total efficiency can be calculated, using the following equation:

$$\eta_{total} = P_u/P_r \tag{4.22}$$

4.2.2 Fan Characteristic curves

One of the most important ways of analysing fan performance, which is also commonly obtained from manufacturers when using a commercial fan, is by drawing performance curves. This curves depict, graphically, mass-flow, rotational speed, fan pressures and fan powers. These curves can illustrate the performance characteristics of the fan like areas of instability, or the rate of change between flow and pressure. With some basic knowledge of performance curves, decisions can be made concerning fan selection, fan and system alterations, or the advisability of using a fan in a modulating system, for example. Data points are collected at a given RPM while the flow is slowly modulated from full closed to full open. A complete fan characteristic curve extends from zero fan static pressure to zero inlet volume flow rate plotted as a series of test points against inlet volume flow. Smooth curves should be drawn through these points, with broken-line sections joining any discontinuities where stable results are not obtainable.

Fan characteristic curves are obtained at constant rotational speeds and different throttling conditions which is the form of adjusting fan characteristic curves for altering their performance. A family of constant speed characteristic curves at 1,2 kg/m3 inlet density is recommended, selected at suitable steps of adjustment over the whole available range of volume flow rates. Usually, fan pressure, p_f, fan static pressure, p_{sf}, fan input power, P_r, and fan air power, P_u, are plotted against the inlet volume flow rate, $q_{V,sg1}$. The fan efficiency, η_{total}, can be plotted in the form of a map using inlet volume flow rate, $q_{V,sg1}$ and compression ratio, r. Efficiencies may be shown by means of smooth contours drawn through points of equal efficiency on the fan pressure characteristic curve. In the drawn fan curves, fan's performance can be extrapolated to different speeds since the following fan scaling laws are expected:

- Flow rate varies as (fan speed)

- Fan total and static pressures varies as (fan speed)^2

- Fan input and output powers varies as (fan speed)^3

4.3 Experimental Procedure

For the performance analysis, it was chosen to test as much combinations as possible from the settable parameters: rotor-stator spacing, inflow condition, throttling and fan speed. Succinctly, rotor-stator spacing of 0.43 (0) and 0.95 (1), inflow conditions no ICD(0) and ICD (1), throttling of 0% (1), 25% (2), 40% (3), 50% (4), 60% (5) and 70% (6) area restriction, and fan speeds from 500 to 4500 rpm were tested. In this campaign, no acoustic measurements were necessary. Tables 8, 9 and 10, in the Appendix B, contain the test matrix of the experiments, with all the configurations actually tested.

4.4 Experimental Results

4.4.1 Baseline Fan Performance

The effect that the fan speed has over the inlet mean volume-flow rate is depicted in Figure 20a. As expected, the volume-flow rate is related linearly with the increase in fan speed. The advance-ratio, defined as $J = \frac{V}{nD}$, is therefore also kept constant for a given throttling condition, as is the flow structure (velocity triangles). Also, it is possible to notice that as the flow is restricted in the outlet of the Rig, the volume-flow rate and advance ratio are decreased. The relation of the restriction area with the volume-flow is not linear for each velocity, as seen in Figure 20b.

Figure 20: Adjustable parameters effects on mean volume flow rate (No ICD, RSS = 0.43).

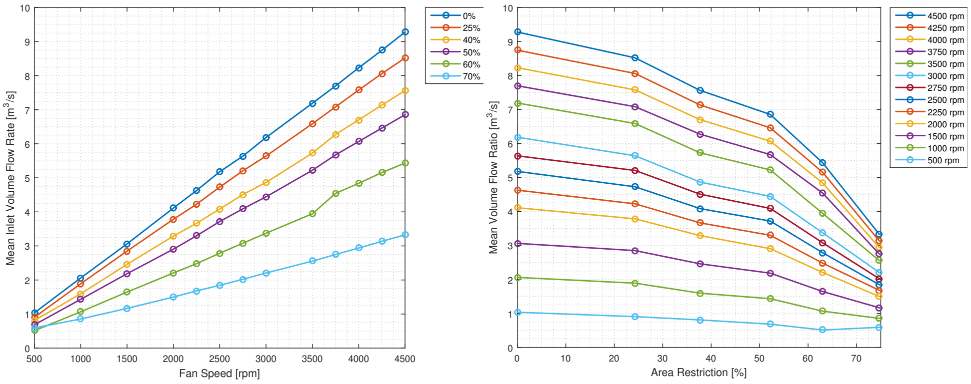
(a) Fan speed effect.
(b) Throttling effect.

Source: Elaborated by the author.

Fan total and static pressure curves can be seen in Figures 21a and 21b. These two graphs are related by the subtraction of the inlet average dynamic pressure at each test from the total fan pressure leading to the fan static pressure. The first observation to be made is that the gauge static pressures used to calculate both of them was limited to approximately 1070 Pa, and, thus, as easily seen in Figure 21b in the form of a *plateau*, some values are not strictly valid. Nevertheless, the expected behaviour was obtained.

For a constant speed curve, the centre points, with higher pressure, are the points in which the operating condition is optimal. Going for a higher flow rate makes the fan pressure drop quickly and, thus, the fan is pumping air, but it is not increasing its static pressure, i .e. not transferring all possible energy. Going for lower flow rates, or too much throttling, makes the blades angles of attack too high and the fan enters in a stalled condition, named surge. This is also an inefficient condition, where the fan is at high loads but the air is not pumped. Both figures show the increase in pressure with fan speed and the relation between curves is quadratic for each throttling condition.

Figure 21: Pressure and power curves (No ICD, RSS = 0.43).

(a) Fan total pressure. (b) Fan static pressure.

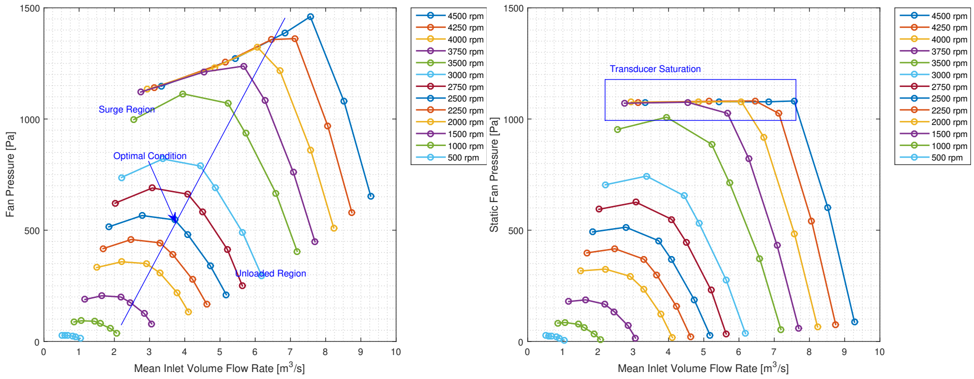

(c) Electrical input power. (d) Fan air power.

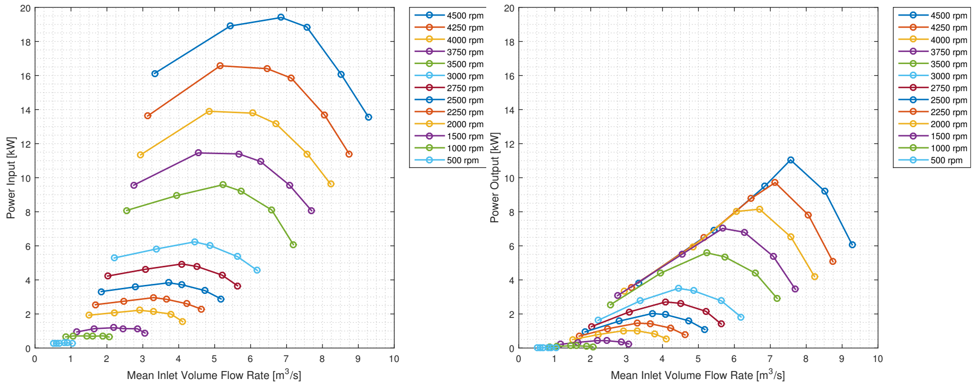

Source: Elaborated by the author.

Electrical input power curves can be seen in Figure 21c and denotes the power consumption from the the electrical grid. Obviously, it is increased with rotational speed and has a maximum over a range of flow rates. Fan air power can be seen in Figure 21d is obtained by multiplying fan pressure and mean volume flow rate, meaning the amount of energy that was harnessed by the flow. The output power is directly affected by fan pressure and the saturation on the pressure sensors is present in this graph as well where the curves of higher speeds (4000, 4250, 4500 rpm) have lower values than what was actually happening in the lower volume flow rate range. Both figures show the increase in power with fan speed and the relation between curves is cubic for each throttling condition.

Figure 22b shows the efficiency curves for each of the fan speeds tested. For each of the velocities there is a peak in efficiency for a moderate flow rate value and this flow rate value of maximum efficiency is dislocated right as the speed is increased. Figure 23 compiles all the information on the fan performance, compression rate and volume flow rate are linked through this map in the total efficiency of the system. As expected, when both compression rate and volume flow rate are increased accordingly, the efficiency is maximum.

Figure 22: Fan compression ratio and efficiency (No ICD, RSS = 0.43).

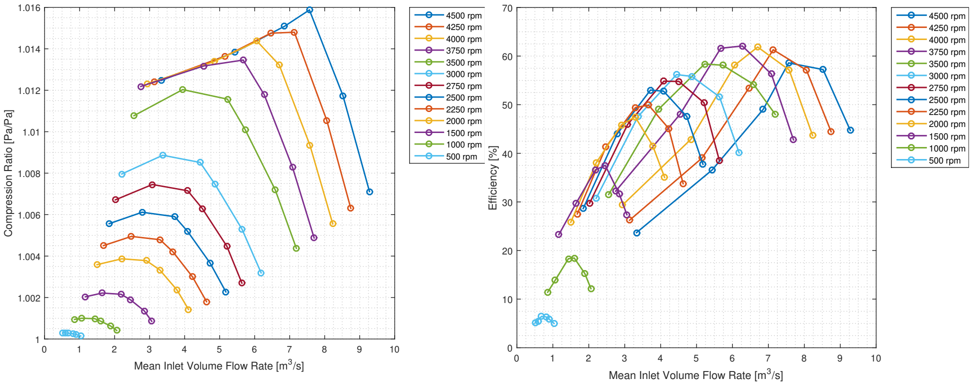

(a) Compression ratio curves.

(b) Fan Efficiency curves.

Source: Elaborated by the author.

Figure 23: Fan efficiency map (ICD, No ICD, ICD + RSS=0.95).

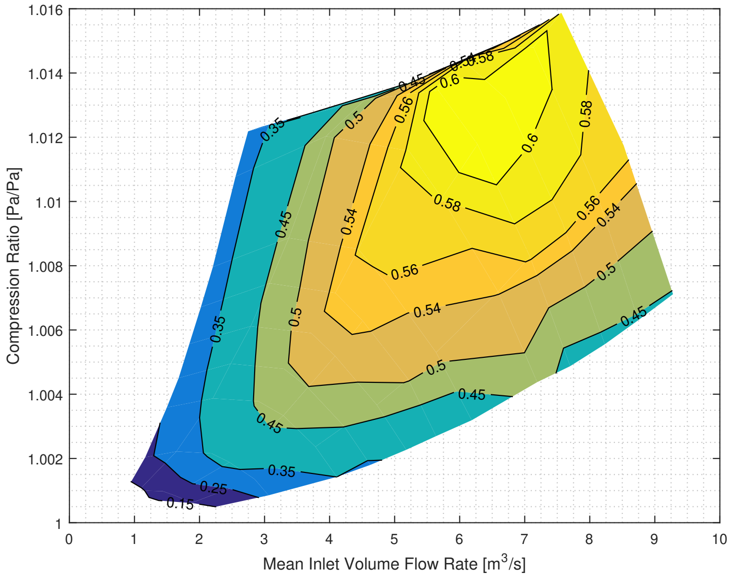

Source: Elaborated by the author.

4.4.2 Effects of ICD Installation and Rotor-Stator Spacing on Fan Performance

By installing the ICD in the duct inlet, it is possible to create a flow obstruction, just as throttling would create, and increase fan loading. But the current configuration of the ICD consists simply of a steel mesh of high porosity and in a section of very low speed, therefore, its effect might become negligible. Rotor-stator spacing effect on the flow characteristics is mainly acoustical and, again, might have negligible in fan performance. The next graphs try to analyse these modifications effects on performance quantities.

Figure 24 compares the mean volume flow rate of the open inlet configuration of the Rig with the mean volume flow rate curves when the ICD is installed or the fan-stator spacing is increased. It is possible to see that for lower throttling configuration there is not any clear effect of this modifications and the curves are superposed. After stalling (at 50% throttling, each configuration reach a very different mean volume flow rate, and the ICD has lesser effect than increasing rotor-stator spacing. Also, the effect of rotational speed is still the same and the volume flow rate scales linearly with the fan speed.

Figure 24: Fan speed effect on mean volume flow rate (ICD, No ICD, ICD + RSS=0.95).

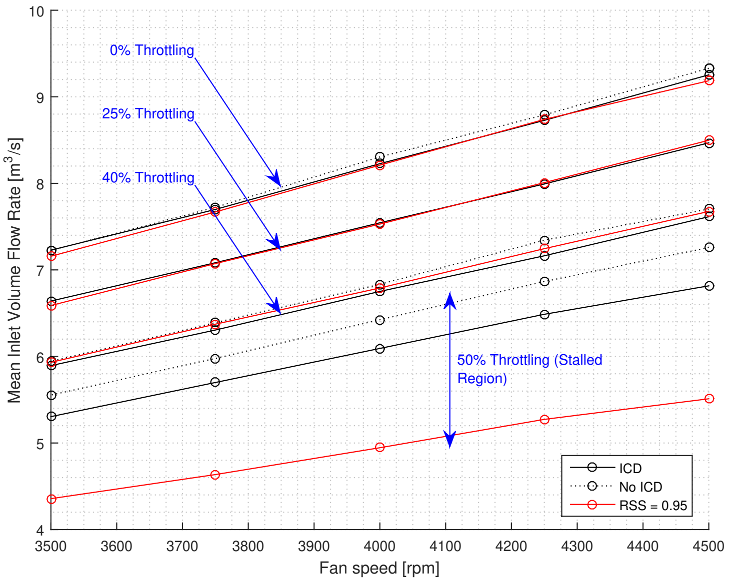

Source: Elaborated by the author.

Figure 25 compare fan pressures, and power quantities, of the open inlet configuration of the Rig with the curves when the ICD is installed or the fan-stator spacing is increased. Again, the conclusion is that for the region of lower fan loading, there is little difference between the curve and the effect of rotor-stator spacing is more pronounced in surge condition.

Figure 25: Pressure and power curves (ICD, No ICD, ICD + RSS=0.95).

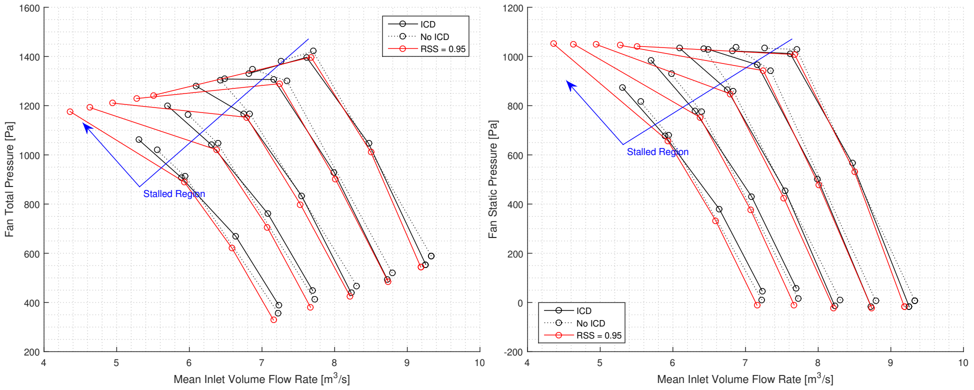

(a) Fan total pressure.

(b) Fan static pressure.

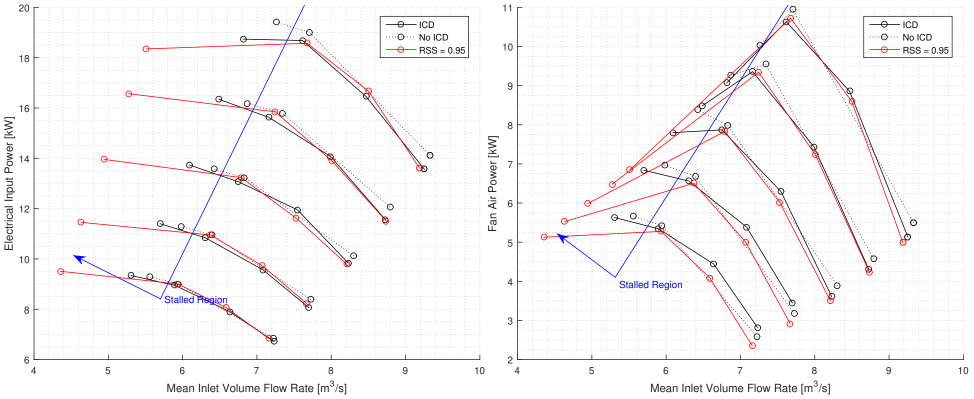

(c) Electrical input power.

(d) Fan Air power.

Source: Elaborated by the author.

4.5 Summary

A performance campaign was carried out to characterise the effects of controllable parameters on the aerodynamic characteristics of the flow. Starting from unrestricted flow to 70% area constraint, and a range of fan speeds, several flow measurements that could be translated into performance quantities were taken: volume flow rate, fan total and static pressures, compression ratio, total and net power, and efficiency. The measured compression ratio ranged from 1.00 to 1.02, with maximum axial Mach of 0.13 and maximum total efficiency of 65%. The surge effect, an unstable configuration characterised by rotor blades stall was also observed. Significant differences in fan performance due to the installation of an Inlet Control Device (ICD) and the rotor-stator spacing were not found, except under surge conditions. Other main conclusions are: the flow quantities behave as expected, i.e. flow Rate varies as fan speed; fan total and static pressures varies as fan speed to the power of two, Fan input and Output powers varies as fan speed to the power of three. The installation of the ICD and rotor-stator spacers have negligible effect as long as the fan is not in surge condition

5 PARAMETRIC CAMPAIGN

5.1 Introduction

An effort to understand fan generated noise and its sources is being taken at the Department of Aeronautical Engineering at the University of São Paulo. From a parametric campaign taken at the EESC-USP Fan Rig, in which several fan speed, loading conditions, rotor-stator spacing and inflow configurations, noise spectral and modal components are presented. A good part of the expected effects, as the rotor-stator interaction modes at the blade passing frequencies, were observed, in agreement with literature and publications of other similar fan rigs. This experimental data collected at this parametric campaign will also be valuable as input for semi-empirical and semi-analytic prediction methods which are developed at the University of São Paulo. Also, it is valuable for the development of noise reduction technologies in partnership with other Brazilian universities members of the SILENCE Project.

5.2 Theoretical Background

5.2.1 General Formulation for Cylindrical Ducts Acoustics

An important starting point for the fan noise analysis is the Goldstein's wave equation (GOLDSTEIN, 1976). The formulation described below follows what is done by Glegg e Devenport (2017). It considers an inviscid flow with no heat conduction and the mean flow as homentropic, i.e. of uniform and constant entropy. We start considering the time derivative of the continuity equation:

$$\frac{\partial^2 \rho}{\partial t^2} + \frac{\partial}{\partial t} \nabla \cdot (\rho \mathbf{v}) = 0 \tag{5.1}$$

This equation can be linearized about the mean flow and, if the RDT (Rapid Distortion Theory) is assumed, i.e. the flow perturbations are convected by the mean flow but not by itself, we obtain:

$$\frac{D_0}{Dt}\left(\frac{1}{\rho_0 c_0^2}\frac{\partial p}{\partial t}\right) + \frac{1}{\rho_0}\nabla\left(\rho_0 \frac{\partial \mathbf{v}}{\partial t}\right) = 0, \qquad \frac{D_0 s}{Dt} = 0 \tag{5.2}$$

Goldstein (1976) decomposes the velocity vector in three terms: a velocity potential, phi, the mean flow, U, and the disturbances, $u^{(g)}$:

$$\mathbf{v} = \mathbf{U} + \nabla\phi + \mathbf{u}^{(g)} \tag{5.3}$$

Also, the velocity potential term can be expressed as in relation to the pressure fluctuations:

$$\rho_0 \frac{D_0}{Dt}\left(\frac{\partial \phi}{\partial t}\right) = -\frac{\partial p}{\partial t} \tag{5.4}$$

The velocity vector and this last relation can be substituted back in the linearized continuity equation giving:

$$\frac{D_0}{Dt}\left(\frac{1}{c_0^2}\frac{D_0\dot{\phi}}{Dt}\right) - \frac{1}{\rho_0}\nabla(\rho_0\nabla\dot{\phi}) = \frac{1}{\rho_0}\nabla\left(\rho_0\dot{\mathbf{u}}^{(g)}\right) \tag{5.5}$$

Now, assuming low Mach numbers, with constant mean density and speed of sound, we can write the last equation considering the fluctuating parts, giving the Goldstein's wave equation:

$$\frac{1}{c_\infty}\frac{D_\infty^2\phi}{Dt^2} - \nabla^2\phi = \nabla\cdot\mathbf{u}^{(h)} \tag{5.6}$$

Next, considering this Goldstein's wave equation without a source term and written in terms of cylindrical coordinates we have:

$$\frac{1}{c_\infty}\frac{D_\infty^2\phi}{Dt^2} - \frac{\partial^2\phi}{\partial x^2} - \frac{1}{R^2}\frac{\partial^2\phi}{\partial\psi^2} - \frac{1}{R}\frac{\partial}{\partial R}\left(R\frac{\partial\phi}{\partial R}\right) = 0 \tag{5.7}$$

The solution of this equation is the velocity potential, ϕ, that uses a time dependence and mean flow in the x direction. Also, the sound field can be considered periodic in the ψ direction, yielding:

$$\phi(R,\psi,x,t) = \sum_{m=-\infty}^{\infty}\hat{\phi}_m(R,x)e^{-i\omega t - im\psi} \tag{5.8}$$

where $\hat{\phi}_m(R,x)$ are the complex Fourier series coefficients of order m. Substituting this back in the wave equation in cylindrical coordinates we obtain:

$$\left(k^2 - \frac{m^2}{R^2}\right)\hat{\phi}_m + 2ikM\frac{\partial\hat{\phi}_m}{\partial x} + (1-M^2)\frac{\partial^2\phi_m}{\partial x^2} + \frac{1}{R}\frac{\partial}{\partial R}\left(R\frac{\partial\hat{\phi}_m}{\partial R}\right) = 0 \tag{5.9}$$

This last equation is the basic equation that describe wave propagation in a circular duct. The next step is to consider the peculiarities of the boundary conditions of the this equation. Since in most cases the fans are inserted in a hard walled duct, this can be integrated in the equation. This will lead to velocity perturbations in the direction normal to the wall being zero.

Considering that the mean flow is independent of radial coordinate, we can make use of the method of separation of variables as to find a solution for the last equation. So we propose:

$$\hat{\phi}_m(R, x) = X_m(x)\Psi_m(R) \tag{5.10}$$

And so,

$$\left(k^2 - \frac{m^2}{R^2}\right) + \frac{2ikM}{X_m}\frac{\partial X_m}{\partial x} + \frac{(1 - M^2)}{X_m}\frac{\partial^2 X_m}{\partial x^2} + \frac{1}{\Psi_m R}\frac{\partial}{\partial R}\left(R\frac{\partial \Psi_m}{\partial R}\right) = 0 \tag{5.11}$$

This last equation can now be split into two parts, since the second and third term are independent of R and should be equal to a constant (here chosen to be $-\kappa^2$) so that the equation is always valid.

The first equation is:

$$\frac{2ikM}{X_m}\frac{\partial X_m}{\partial x} + \frac{(1 - M^2)}{X_m}\frac{\partial^2 X_m}{\partial x^2} = -\kappa^2 \tag{5.12}$$

And the second:

$$\left(k^2 - \frac{m^2}{R^2} - \kappa^2\right) + \frac{1}{\Psi_m R}\frac{\partial}{\partial R}\left(R\frac{\partial \Psi_m}{\partial R}\right) = 0 \tag{5.13}$$

The first equation can be solved by seeking a solution of the form $X_m(x) = C_m e^{i\mu x}$. The value of μ is obtained by substituting the solution in the equation and has two possible values:

$$\mu = \frac{kM}{\beta^2} \pm \sqrt{\left(\frac{kM}{\beta^2}\right)^2 + \frac{\kappa^2}{\beta^2}} \tag{5.14}$$

The second equation can be solved by transforming it in the well-know Bessel's equation:

$$\frac{\partial^2 \psi_m}{\partial R^2} + \frac{1}{R}\frac{\partial \psi_m}{\partial R} + \left(\alpha^2 - \frac{m^2}{R^2}\right)\psi_m = 0, \qquad \alpha^2 = k^2 - \kappa^2 \tag{5.15}$$

with a solution of the form:

$$\psi_m(\alpha R) = AJ_m(\alpha R) + BY_m(\alpha R) \tag{5.16}$$

where $AJ_m(\alpha R)$ and $BY_m(\alpha R)$ are Bessel functions of the first and second kind of order m.

5.2.2 Modal Propagation

Equations 5.8 and 5.10 can be used to describe the modal propagation of sound in a duct, as:

$$\phi(R,\psi,x,t) = \sum_{m=-\infty}^{\infty}\sum_{n=0}^{\infty} \tilde{A}_{mn}\Psi_m(\alpha_{mn}R)\exp^{-i\omega t - im\psi + i\mu^{\pm}_{mn}x} \tag{5.17}$$

where we define $\mu^{\pm}_{mn}$ as, from the dispersion relationship (Equation 5.14), as the wavenumber of axial direction propagation:

$$\mu^{\pm}_{mn} = -\frac{kM}{\beta^2} \pm \sqrt{\left(\frac{kM}{\beta^2}\right)^2 + \frac{k^2-\alpha^2_{mn}}{\beta^2}} \tag{5.18}$$

This last expression can be rearranged as:

$$\mu^{\pm}_{mn} = -\frac{kM \pm k_{mn}}{\beta^2}, \qquad k_{mn} = \sqrt{k^2 - \alpha^2_{mn}\beta^2}, \qquad \beta^2 = 1 - M^2 \tag{5.19}$$

This expression gives a lot of insight about the propagation in the duct. The ± sign means that the sound propagates both downstream and upstream to the sources. The fact that it can be either an imaginary or real number, gives the possibilities of these waves to propagate or rapidly decay in the duct. The rate of decay depends on the “cut-off ratio”, χ_{mn}:

$$\chi_{mn} = \beta\alpha_{mn}/k \tag{5.20}$$

A large “cut-off ratio” (» 1) means that $\mu^{\pm}_{mn}$ has a large absolute value of the imaginary part. This means that the duct mode (m,n) decays along the duct. Otherwise, if the “cut-off ratio” is small, $\mu^{\pm}_{mn}$ is a real value and the mode propagates without attenuation and with the following wavenumber:

$$\frac{\pm k}{1 \pm M} \tag{5.21}$$

The distance for which the “cut-off” modes are negligible can be calculated from the decay rate of these modes, which depends on:

$$\exp\left(-(k|x|/\beta^2)\sqrt{\chi^2_{mn}-1}\right) \tag{5.22}$$

5.2.3 Duct Mode Amplitudes

The acoustic field in the duct can be expressed by a modal expansion using the velocity potential at a fixed frequency , ω, defining the amplitude of each mode as $A_{m,n}(\omega)$.

From this, the acoustic pressure in the duct, which is related to the velocity potential by $p' = -\rho_\infty D_\infty \phi / Dt$, can be expressed in a similar manner:

$$p'(\mathbf{x}, t) = \int_{-\infty}^{\infty} \sum_{m=-\infty}^{\infty} \sum_{n=0}^{\infty} P_{mn}(\omega) \Psi_{mn}(R) e^{im\psi - i\omega t - i\mu_{mn}^{\pm} x} d\omega \tag{5.23}$$

where

$$P_{mn}(\omega) = -i\rho_\infty(\omega + U\mu_{mn}^{\pm}) A_{mn}(\omega) \tag{5.24}$$

5.3 Data Processing

5.3.1 Spectral Analysis

To obtain the frequency spectrum, it is necessary to do a sampling of the continuous-time signal, pre-filter it to avoid aliasing. Later, numerical methods are used to perform windowing, block processing and Fourier Transform of this discrete-time signal. In this study, the method utilised for estimating power spectra is Welch's method, also called the periodogram method. It consists on a modified Fast Fourier Transform to estimate power spectra. It is carried out by sectioning the recorded noise signal into successive blocks, forming the periodogram for each block and averaging them.

A standard way to characterise aeroacoustics measurements is throughout their power spectral density and observe important characteristics of a noise signal is to obtain its frequency spectrum, due to their nature as a regular stochastic process. Spectral estimation methods is used to calculate a cross-spectral density distribution. As input, for each configuration, a sampling frequency of 51.2 kHz and 39 seconds of acquired acoustic data is used, which allows the adequate use of the well-known Welch's method (PERCIVAL; WALDEN, 1993; MUELLER, 2001) with 2048 samples Hanning window and 50% overlap. Plots are displayed in terms of SPL levels by taking the logarithmic value with reference to $p_{ref} = 20\mu Pa$ sound pressure, i.e., $SPL = 10 \cdot log_{10}(S/p_{ref}^2)$, where S is the power spectrum density estimated.

5.3.2 Modal decomposition

A special characteristic of fan generated noise is the possibility, when it is inserted in a duct of constant cross section with constant boundary conditions (as a hard wall casing) and medium (incompressible air), to obtain a series expansion of the wave equation solution for time-harmonic perturbations. Each of these self-similar solutions is called a mode. These modes are important because they are a simple way to represent very complex solutions of the acoustic field and they can be used to identify noise generation mechanisms. Modal decomposition here is obtained using beamforming, which is a well-used technique for locating noise sources for a range of desirable frequencies (MUELLER, 2001). To achieve this task an array of microphones was specially designed for this setup, taking as input requirements: the signal bandwidth, focal distance, duct diameter, blade and vane counting and the maximum circumferential order of modes we desire to measure. The blade and vane counting and the maximum mode order are directly related through Tyler-Sofrin (TYLER; SOFRIN, 1962) relation, which states the limits of cut-on duct modes. The classical beamforming formulation used in this work is nearly the same as described by Caldas et al. (2016b), Caldas (2016) as follows

$$b_{m,n} = \frac{g_{m,n} \cdot C \cdot g_{m,n}^H}{\sqrt{N \|g_{m,n}\| \|g_{m,n}\|^H}} \tag{5.25}$$

where C is the cross-spectral matrix and $g_{m,n}$ is the modal steering vector computed mode by mode. The main diagonal of C is excluded to avoid boundary layer noise in the auto-spectra of each sensor (MUELLER, 2001). The square root added in the denominator of Eq. 5.25 was empirically tested and led to a better results in terms of modal power levels. Dougherty e Walker (2009) showed that a slight weight modification in the formulation 5.25 would lead results proportional to acoustic pressure, instead of source power. This is obtained by

$$b_{m,n} = \frac{\|g_{m,n}\| \|g_{m,n}\|^H}{N} b_{m,n} \tag{5.26}$$

The steering vector formulation used is given by

$$g_{m,n}(\vec{r_i}, \vec{r_s}, \omega) = \frac{J_m(k_{m,n} r_i) J_m(k_{m,n} r_s)}{N_{m,n}^2} e^{jm(\theta_i - \theta_s)} e^{-jk_z^{(-)}(z_i - z_s)} \tag{5.27}$$

where $J_m(x)$ is a Bessel function of first kind, $\vec{r} = (r, \theta, z)$ is the position vector in cylindrical coordinates, subscripts i and s refer to microphone and mesh point indexes, respectively. $k_z^{(-)}$ is the axial wave number and the superscript $^{(-)}$ means the upstream propagation wave, i.e., from the fan to the microphone array.

Values of $k_{m,n}$ are computed so that $J'_m(k_{m,n} a) = 0$, i.e., the product $k_{m,n} a$ is the n^{th} stationary point of order m of the first kind Bessel function $J_m(x)$. $N_{m,n}^2$ in Eq. 5.27 is a mode normalisation for energy conservation, it is computed by

$$N_{m,n}^2 = \left(1 - \frac{m^2}{(k_{m,n} a)^2}\right) |J_m(k_{m,n} a)|^2 \tag{5.28}$$

In order to obtain sound pressure (or amplitude) of each (m,n) mode, the output beamforming map $b_{m,n}$ should be integrated over the duct cross section **S**. This can be achieved by

$$P_{m,n}^2 = \int_{\mathbf{S}} b_{m,n} d\mathbf{S} \tag{5.29}$$

where $P_{m,n}^2$ is the estimated pressure amplitude of the respective (m,n) mode. However, a suitable representation for modal analysis relies on their respective power level (PWL) $\hat{\mathbf{P}}_{m,n}$ instead of SPL levels. Then, the mode power can be obtained from the pressure level by the formulation introduced by Sutliff (2005)

$$\hat{\mathbf{P}}_{m,n} = \mp \frac{\pi a^2(1-\sigma^2)}{\rho_0 c_0} \beta^4 Re \left\{ \frac{\sqrt{1-\frac{1}{\zeta^2}}}{\left\| 1 \pm M\sqrt{1-\frac{1}{\zeta^2}} \right\|^2} \right\} \|P_{m,n}^2\| \tag{5.30}$$

where

$$\zeta = \frac{f}{f_c} = \frac{2\pi f}{c_0 \beta k_{m,n}} \tag{5.31}$$

$\beta^2 = 1 - M^2$ and ζ is the cut-off ratio as defined by Sutliff (2005), i.e., the ratio between the frequency of interest and the cut-off frequency for the given (m,n) mode order. In the special case of $k_{m,n} = 0$ (or “infinite” axial wave number) the cut-off frequency f_c can be defined. Indeed, the eigenvalue $k_{m,n}$ increases with m or n and f_c also increases for higher order modes.

5.4 Experimental Procedure

For the parametric analysis, it was chosen to test as much combinations as possible from the settable parameters: rotor-stator spacing, inflow condition, throttling and fan speed. Succinctly, rotor-stator spacing of 0.43 (0) and 0.95 (1), inflow conditions No ICD (0), ICD (1) and Turbulence Grid (2), throttling of 0% (1), 25% (2), 40% (3) and 50% (4) area restriction, and fan speeds from 4500 to 3000, with steps of 250 rpm (1-6), were tested. In this Campaign, the complete inlet microphone antenna was used. Tables 8, 9 and 10, in the Appendix B, contain the test matrix of the experiments, with all the configurations actually tested.

5.5 Experimental Results

5.5.1 Effects of Fan Speed

As it is possible to see at Table 11, the fan advance ratio and blade angle of attack maintain themselves constant as the fan rotational speed is increased. That happens because, for a given loading condition, the aerodynamic flow structure adjusts itself to the fan speed. As stated by Moreau e Enghardt (2009), in this case, the noise sources scale similarly to each other, and an increase throughout the whole frequency spectra is expected, conserving its shape. Conditions 9, 1, 10, 11, 12, and conditions 13, 2, 14, 15, 16 explore this effect for rotor-stator spacing of 0.43 and 0.95, respectively.

The first set results (conditions 9, 1, 10, 11, 12) are presented in Figure 26 below. First graph shows the relation between the noise spectra and shaft speed, where, overall, the shape of the spectra is unaltered by the increase in rotational speed. There are, however, some perceivable exceptions, as, for example, the appearance of a tone at frequencies lower than the first BPF tone for the higher speeds. The increase in the first BPF seems to be linear with the rotational speed, but the following ones do not have a straightforward pattern. Broadband noise levels are increased quite consistently with the speed, including the high frequency bubble, that appears at this fan loading.

Figure 26: Average spectra comparing multiple rotational speeds (RSS = 0.43 and open throttle).

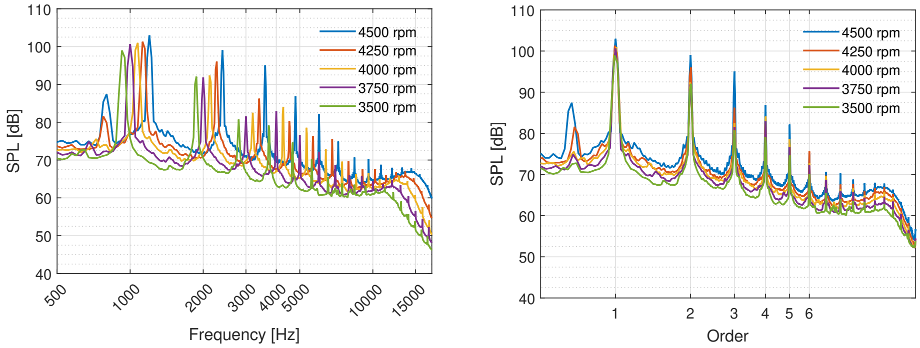
(a) on frequency domain.

(b) on shaft order domain.

Source: Elaborated by the author.

Figure 27a shows the variation on the broadband level in a comparison to the higher rotational speed,27b a comparison between rotational speeds separated by 250rpm, and 27c, the results of the integration between some frequency bands (low frequency band, from 500 Hz and 2 kHz; high frequency band, from 2 kHz and 7 kHz; overall frequency, from 500 Hz to 7 kHz; and bubble frequency band, from 7 kHz to 15 kHz). The overlap in the curves in 27b and results of the integration shown in 27c confirm that the additional broadband (in dB) can be considered linear with the variation in fan speed for the given conditions, and this apply throughout the whole spectra. Additionally, the result of the integration shows that there is as much energy on broadband noise for the lower and the higher frequency bands.

In Figure 28, it can be seen that the summation of the first six BPFs tone levels (called here overtone) is monotonically increasing on an average of 1dB with an increase of 250 rpm on fan speed. However, when we analyze the BPFs one by one, the relation has

Figure 27: Analysis of the effect of RPM on broadband noise (RSS = 0.43 and open throttle).

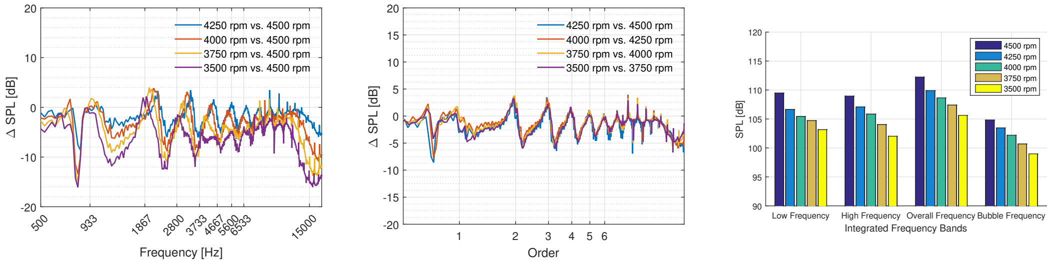
(a) Variation on SPL level (on frequency domain).

(b) Variation on SPL level (on shaft order domain).

(c) Integration of broadband noise.

Source: Elaborated by the author.

no clear pattern on their variation. The first two BPFs follow the same behavior of the overtone, the 3rd grows at higher rates each time the fan speed is raised and the last three have eventual reductions.

Figure 28: Analysis of the BPFs tone levels and overtone (their sum) (RSS = 0.43 and open throttle).

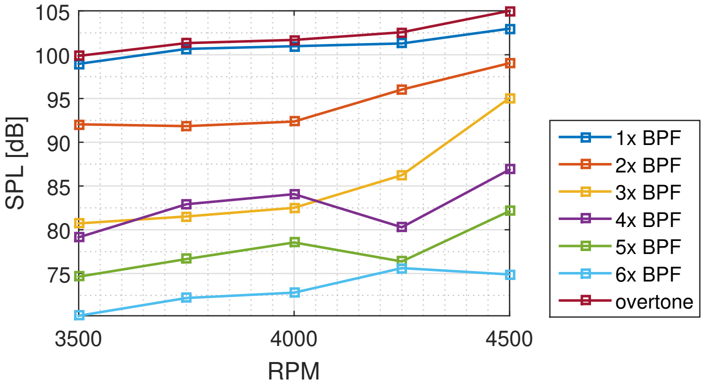

Source: Elaborated by the author.

The rotational speed has a clear effect on the Tyler-Sofrin modes. Reducing the fan speed, directly reduces the SPW of these rotor-stator interaction modes as it can be seen for the (2,0) mode in Figure 29, and for the (4,0) and (6,0) modes at the 2nd and 3rd BPFs, respectively, as shown in Figure 30 and 31. It is also relevant to point out that these modes are fully dominant at the 1st (Figure 29) and 2nd BPFs (Figure 30), with at least 20dB over almost all other cut-on modes, but beyond the 3rd BPF, this no longer applies and the modal structure, besides still being dominated by the interaction mode, also has other relevant components (Figure 31).

Figure 32 compiles the effect of the rotational speed on (2,0), (4,0) and (6,0)

Figure 29: Modal decomposition of the 1st BPF for multiple fan rotational speeds (RSS = 0.43 and open throttle).

(a) 4500 rpm. (b) 4250 rpm.

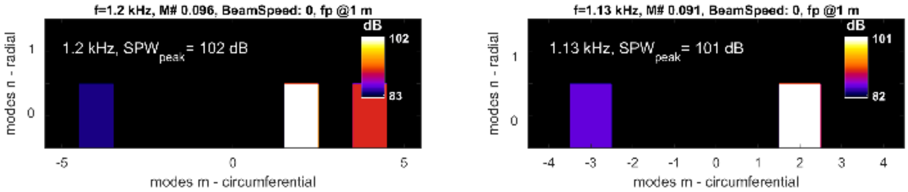

(c) 4000 rpm. (d) 3750 rpm. (e) 3500 rpm.

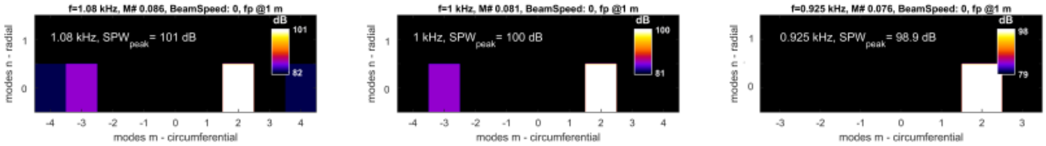

Source: Elaborated by the author.

Figure 30: Modal decomposition of the 2nd BPF for multiple fan rotational speeds (RSS = 0.43 and open throttle).

(a) 4500 rpm. (b) 4250 rpm.

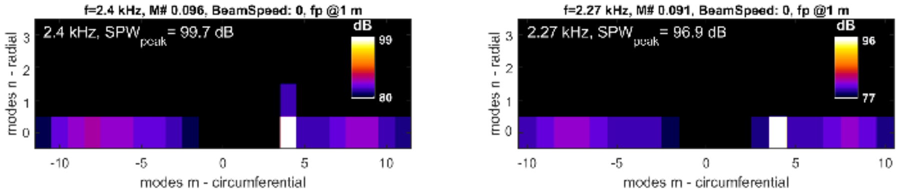

(c) 4000 rpm. (d) 3750 rpm. (e) 3500 rpm.

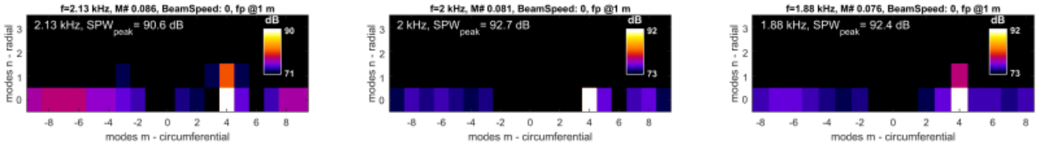

Source: Elaborated by the author.

interaction modes PWL values. Its is possible to see that, for both, rotor-stator spacings, the tendency is of an increase on the PWL value, just as seen with the BPF tone levels.

5.5.2 Effects of Throttling

By changing screens at the duct outlet, we were able to change the flow condition of the fan. The throttling device affects the mass-flow inside the duct and, since the angle of attack of the fan blades is given both by axial and tangential velocity, increasing the area restriction on the duct outlet we induce an increase in fan loading. Only the first five throttling screens were utilized, up to a 70% of area restriction. Beyond that, the fan

Figure 31: Modal decomposition of the 3^{rd} BPF for multiple fan rotational speeds (RSS = 0.43 and open throttle).

(a) 4500 rpm. (b) 4250 rpm.

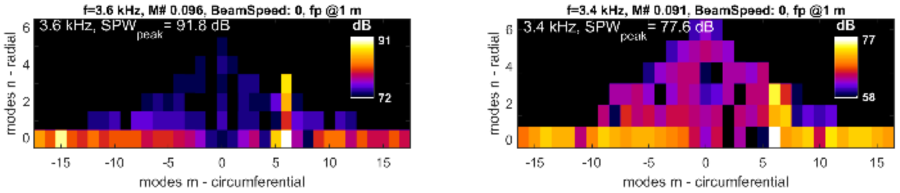

(c) 4000 rpm. (d) 3750 rpm. (e) 3500 rpm.

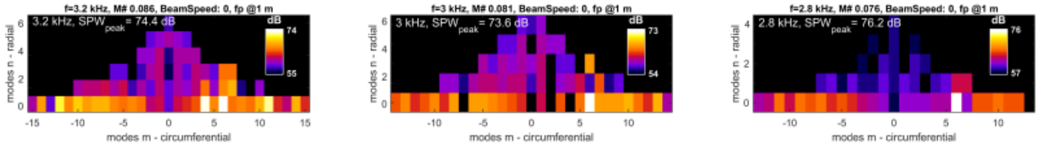

Source: Elaborated by the author.

Figure 32: Interaction modes (2,0), (4,0) and (6,0) compared to fan rotational speed for two rotor-stator spacings (open throttle).

(a) RSS = 0.43. (b) RSS = 0.95.

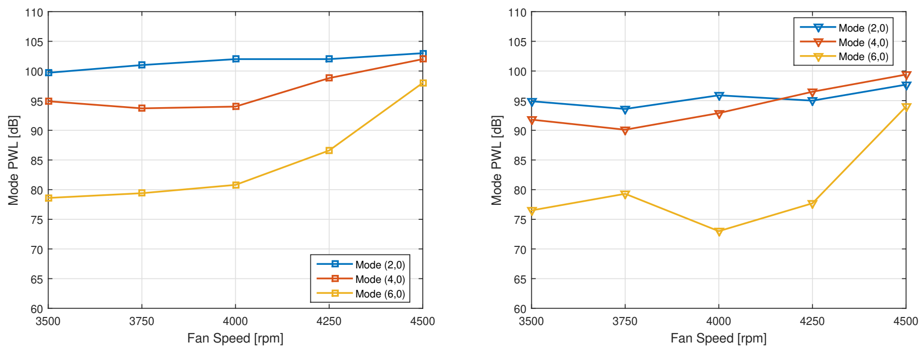

was already stalled and no further tests were of interest. Conditions 1, 4, 5, 6, 7 and 8, conditions 2, 17, 18 and 19, and conditions 3 and 20, explore this effect for RSS = 0.43, RSS = 0.95, and RSS = 1.50, respectively.

Figure 33, shows the averaged spectra for different loading conditions and two different rotor-stator spacing. It is worth mention that the fan noise becomes highly broadband for higher area restriction (>50% of the duct area). The reason for this, probably, is that the fan blades are already in stall condition, because of the blades' angle of attack increase. In this condition, the fan pumps fewer air each time (the axial speed becomes smaller with the increase in area restriction, and the blade wakes are larger and more turbulent. The stalled condition does not necessarily need to affect the whole fan and does not change the fact that while there is still axial flow, there is pressure oscillation due

Figure 33: Averaged spectra for multiple throttling configurations and fan speed of 4250 rpm.

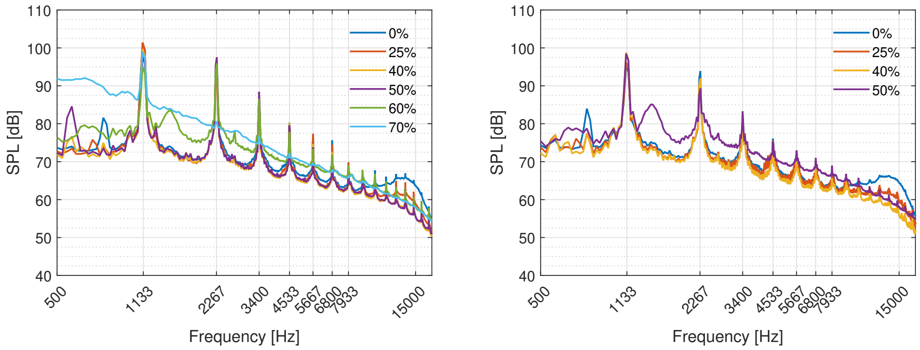

(a) RSS = 0.43.

(b) RSS = 0.95.

Source: Elaborated by the author.

to fan wakes on the stator vanes. But curiously enough, when the area restriction reach 70%, only the 1st BPF is still present. Another effect is the relation with the high frequency bubble: this decrease in axial speed caused by throttling makes the bubble weaker and even disappear for area restrictions higher than 40%. When analysing the broadband (Figure 34a), compared to the open throttle, the other non-stalled configurations, apart from the bubble frequencies, are altered by less than 2dB, but when compared to consecutive conditions, it is possible to see that reduction comes from the 0% to 25% configuration, from 25% not much changes and from 40% to 50%, there is an actual increase in broadband level. Integration of the broadband spectra (Figure 34b) confirms this behavior and shows that this increase in broadband can lead to a very noisy fan.

Figure 34: Analysis of the effect of throttling on broadband noise (RSS = 0.43 and open throttle).

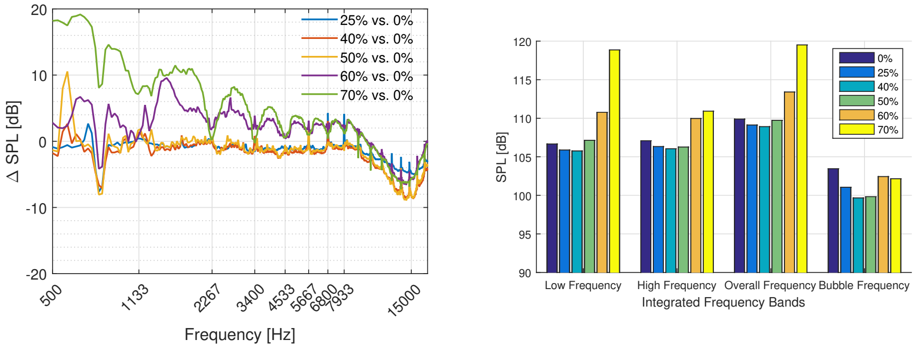

(a) Variation on SPL level (on frequency domain).

(b) Integration of broadband noise.

Source: Elaborated by the author.

When analysing the BPF tone levels (Figure 35), the overall behaviour for the non-stalled configurations is a small reduction on its value, another curious behaviour happens with the second BPF, which seems to increase by the same amount that the 1st BPF is reduced from 25% to 50% area restriction.

Figure 35: Analysis of the BPFs tone levels and overtone (their sum) (RSS = 0.43 and 4250 rpm).

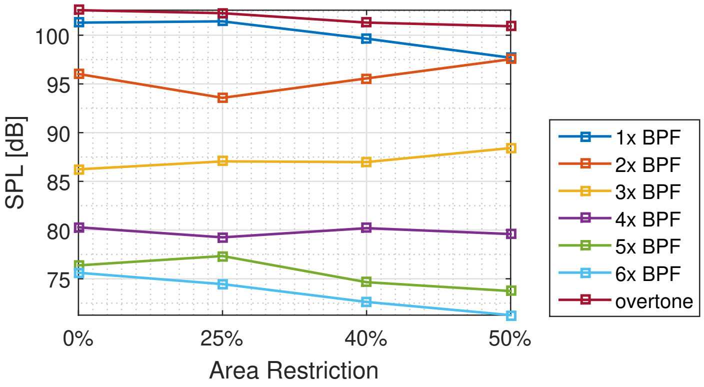

Figure 36: Modal decomposition of the 1st BPF for multiple throttling (RSS = 0.43 and 4250 rpm).

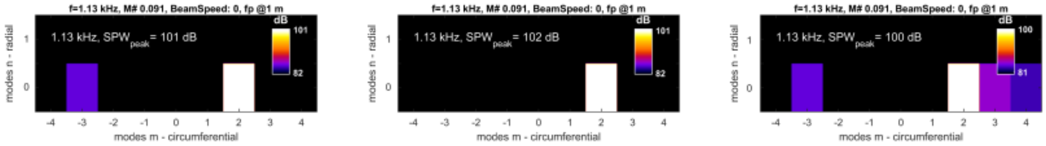
(a) Open throttle.

(b) Throttle at 25% of area restriction.

(c) Throttle at 40% of area restriction.

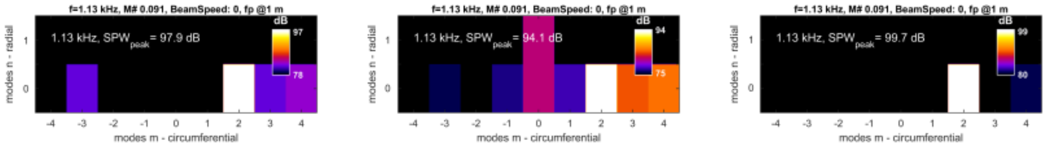
(d) Throttle at 50% of area restriction.

(e) Throttle at 60% of area restriction.

(f) Throttle at 70% of area restriction.

Source: Elaborated by the author.

Figures 36, 37 and 38 present the comparisons for different throttle conditions with respect to the first three BPFs. It is possible to see that the modal structure is clearer at lower loading and the interaction modes (2,0), (4,0), (4,1), (6,0), (6,1), (6,2) are prominent. Figure 39 was taken at the center frequency of the bubble that appear on the spectra of lower loading configurations. In it we try to observe what could be the reason for its existence. Some negative m-modes near the cut-off area show high values at these lower loading configurations and these modes lose power as the loading is increased. But more

Figure 37: Modal decomposition of the 2nd BPF for multiple throttling (RSS = 0.43 and 4250 rpm).

(a) Open throttle. (b) Throttle at 25% of area restriction. (c) Throttle at 40% of area restriction.

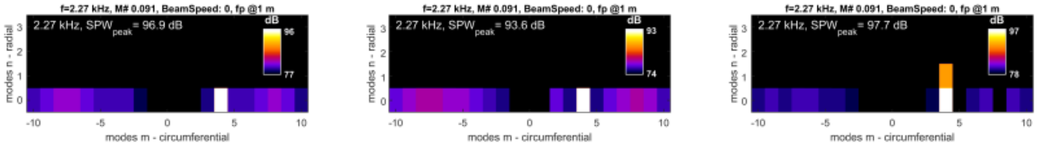

(d) Throttle at 50% of area restriction. (e) Throttle at 60% of area restriction. (f) Throttle at 70% of area restriction.

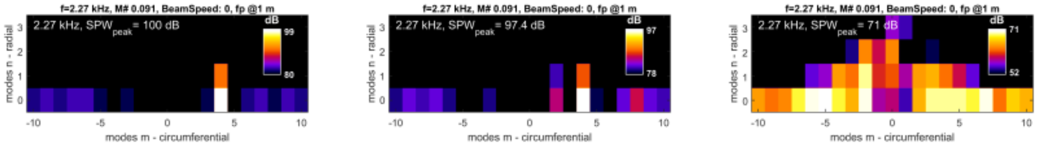

Source: Elaborated by the author.

Figure 38: Modal decomposition of the 3rd BPF for multiple throttling (RSS = 0.43 and 4250 rpm).

(a) Open throttle. (b) Throttle at 25% of area restriction. (c) Throttle at 40% of area restriction.

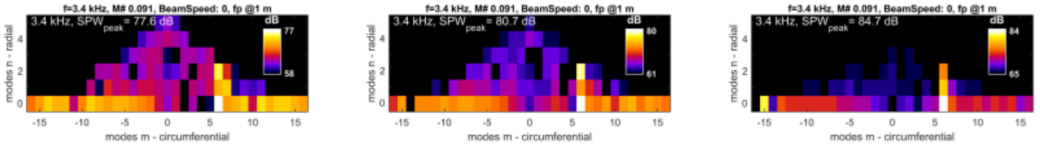

(d) Throttle at 50% of area restriction. (e) Throttle at 60% of area restriction. (f) Throttle at 70% of area restriction.

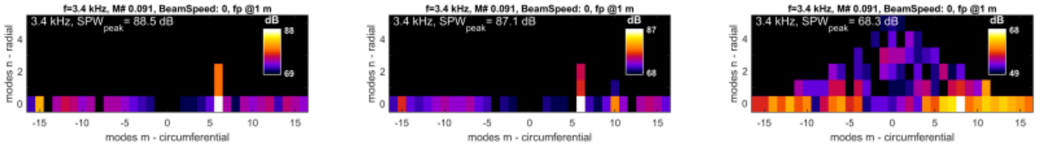

Source: Elaborated by the author.

detailed investigation on the frequencies composing the bubble is needed to confirm this hypothesis.

Figures 41 and 40 compile the effect of the decrease in axial speed induced by imposing an area restriction on the duct outlet on (2,0), (4,0) and (6,0) interaction modes PWL values. Its is possible to see that, for both, rotor-stator spacings, and before stalling, there is not a direct effect on the PWL values that can be spotted.

Figure 39: Modal decomposition of the 12th BPF for multiple throttling (RSS = 0.43 and 4250 rpm).

(a) Open throttle.
(b) Throttle at 25% of area restriction.
(c) Throttle at 40% of area restriction.

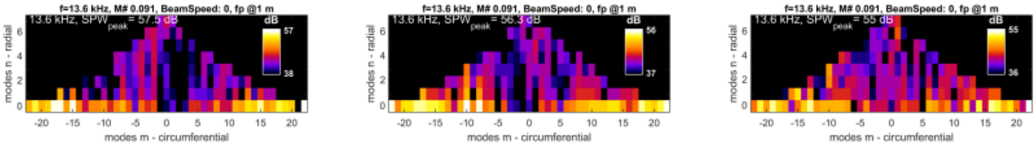

(d) Throttle at 50% of area restriction.
(e) Throttle at 60% of area restriction.
(f) Throttle at 70% of area restriction.

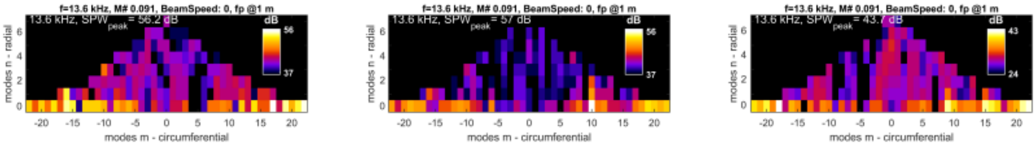

Source: Elaborated by the author.

Figure 40: Interaction modes (2,0), (4,0) and (6,0) compared to advance ratio for two rotor-stator spacings (4250 rpm).

(a) RSS = 0.43.
(b) RSS = 0.95.

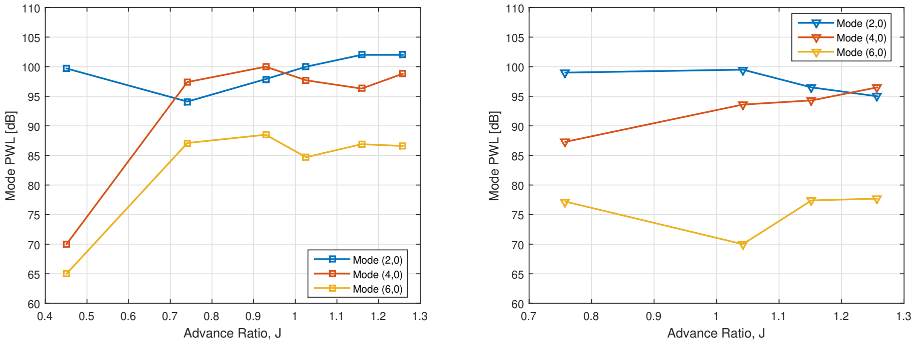

5.5.3 Effects of Rotor-Stator Spacing

From the current beliefs, we expect subsonic fans to have cut-off rotor-alone noise and most of the noise coming from the rotor-stator interaction. This interaction have many noise generating mechanisms itself, but the impingement of the blade wakes on the stator vanes are believed to account for most of this generation. Therefore, bringing the fan downstream, i.e. increasing the gap between rotor blades and stator vanes, would affect tonal noise, that because, with the spacing, the blade wakes are exponentially smoothed out before hitting the stator vanes. Figure 42 shows the effect on the averaged spectra and, as expected, the reduction on the BPF tone levels. It is also interesting noticing that, as explained by Goldstein (1976), the higher order BPF tones intensities are preferably reduced, since it is possible to represent the pressure fluctuations with less components

Figure 41: Interaction modes (2,0), (4,0) and (6,0) compared to throttling configuration for two rotor-stator spacings (4250 rpm).

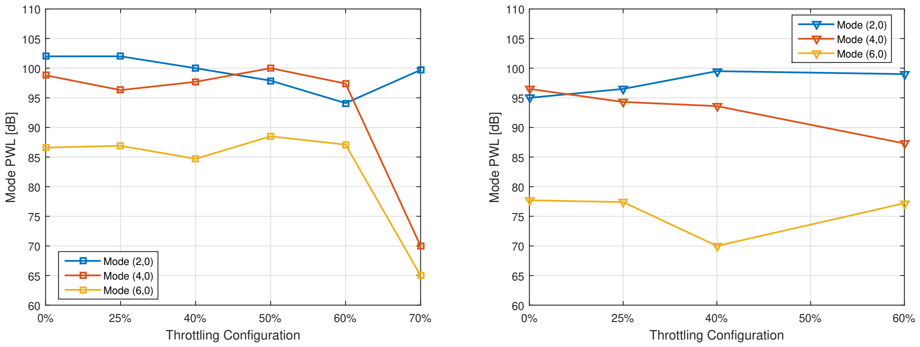

(a) RSS = 0.43.

(b) RSS = 0.95.

Source: Elaborated by the author.

when the deficit in velocity on the blade wakes are smoothed out. Broadband noise is also affected. In our experiments, as the tone levels are reduced, the broadband is increased, as it is possible to see in Figure 42.

Figure 42: Averaged spectra for multiple rotor-stator spacing configurations and fan speed of 4250 rpm.

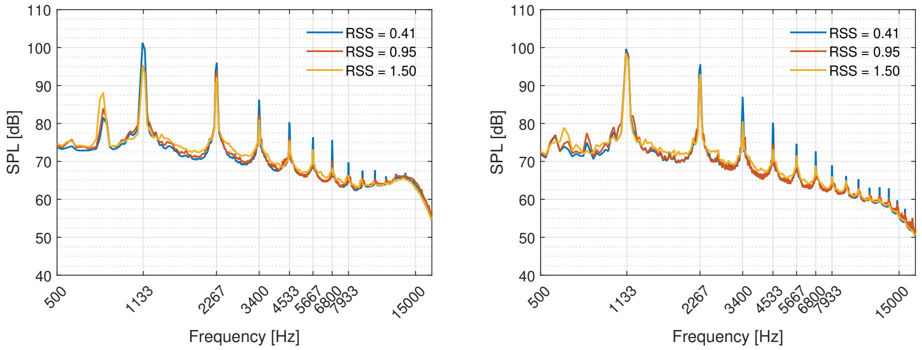

(a) Open throttle.

(b) Throttle at 40%.

Source: Elaborated by the author.

Figure 43 explore the effect of rotor-stator spacing on the broadband SPL levels. It is possible to see in 43a, up to the 2$^{\text{nd}}$ BPF, broadband is increased at least 0.5 dB (up to 2.5 dB) and then this increase is almost zero up to the bubble frequencies, were, one again, broadband is increased to higher levels. Figure 43b shows the integration of the spectra broadband for the three RSS. Again, it is possible to see that there is a increase throughout both low and high frequency bands, but the increase at the low frequency band is bigger.

Figure 43: Analysis of the effect of rotor-stator spacing on broadband noise for multiple throttle configurations.

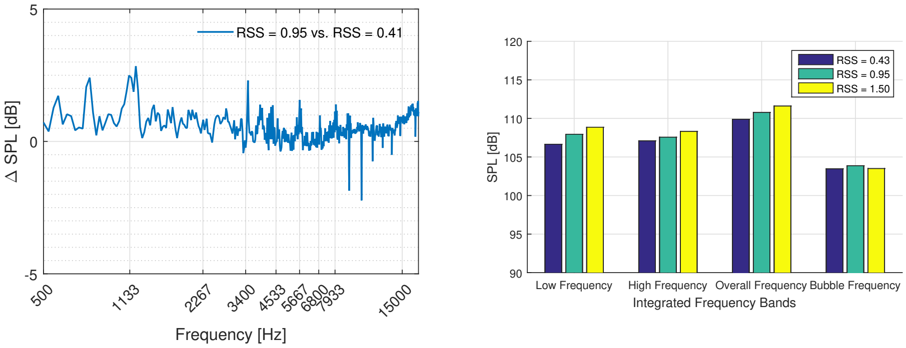

(a) Variation on SPL level (on frequency domain).

(b) Broadband noise integration.

Source: Elaborated by the author.

Figure 44a is the variation between different configurations of RSS and its data has too much noise to find behavior. Figure 44b contains the filtered data of 44a (using a moving average filter with 20 samples), which confirm us as higher broadband level when the gap between rotor and stator is increase. Nevertheless, how much higher and at what frequency bands depend on the fan loading. Between the 1st and the 2nd BPF, the higher the loading the lower is the increase in broadband. But for higher frequencies, the higher increase in broadband is found for the 25%-throttling configuration.

Figure 44: Analysis of the effect of rotor-stator spacing on broadband noise for multiple throttle configurations.

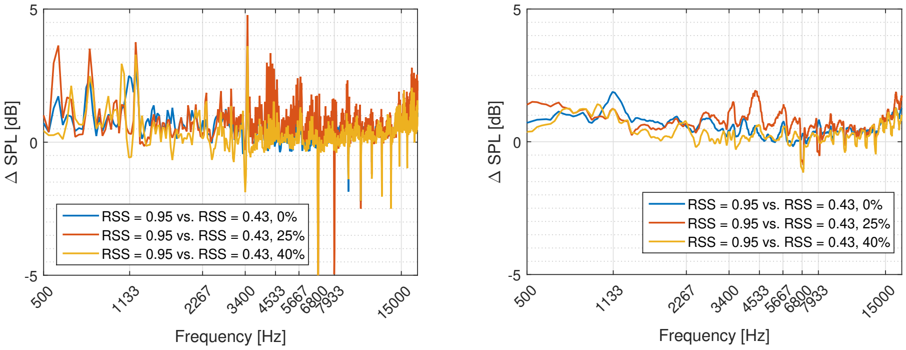

(a) Variation on SPL level (on frequency domain).

(b) Filtered variation on SPL level (on frequency domain).

Source: Elaborated by the author.

The BPF tone levels for the three spacing configurations is seen in Figure 45a. An overall decrease (also perceivable when the tone levels are added up, called overtone) is

Figure 45: Analysis of the BPFs tone levels and overtone (their sum) at 4250 rpm.

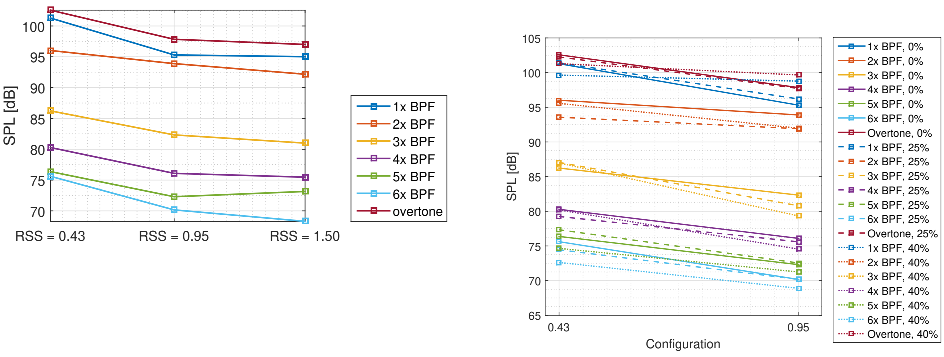
(a) Open throttle.

(b) Throttle from 0% to 40% area restriction.

Source: Elaborated by the author.

Figure 46: Modal decomposition at fundamental tones for rotor-stator spacings (open throttle and 4250 rpm).

(a) 1st BPF with RSS = 0.41.

(b) 1st BPF with RSS = 0.95.

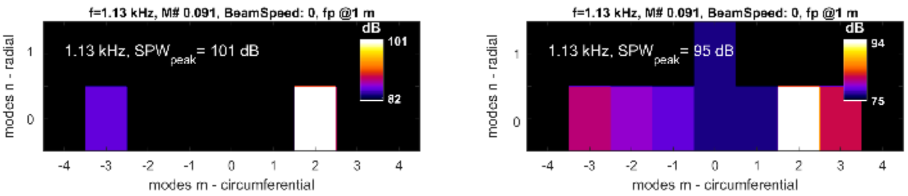

(c) 2nd BPF with RSS = 0.41.

(d) 2nd BPF with RSS = 0.95.

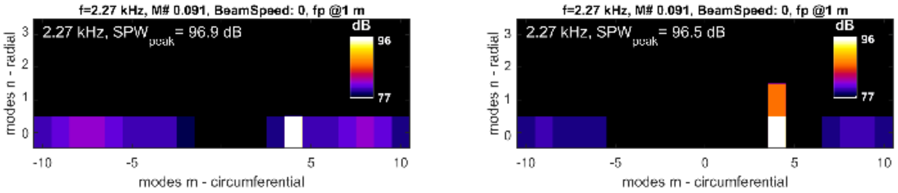

(e) 3rd BPF with RSS = 0.41.

(f) 3rd BPF with RSS = 0.95.

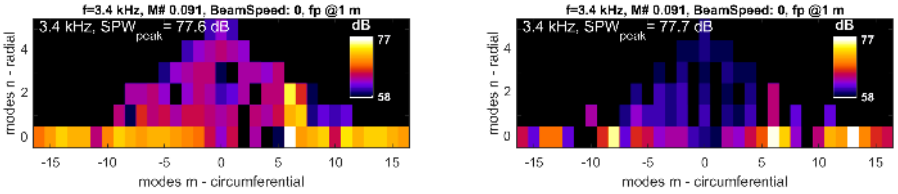

Source: Elaborated by the author.

observed. The overtone goes from 102.5 dB to 97 dB when the spacing goes from 0.41 to 0.95, leading to a value close to 4 dB per doubling. Figure 45b compares the effect of increasing the loading on the BPF tones reduction. The increase in loading reduces the axial speed, and, therefore, increases the distance travelled by the wakes of the blades. As the wakes have to cover a higher distance, they are more smoothed out and, higher decreases, are expected and in general, confirmed by Figure 45b.

Figure 46 show modal decomposition for the first six BPFs for the 4250 rpm configuration. In general, the Tyler-Sofrin modes are dominant and the acoustic power of these modes is reduced with more spacing. This is more evident for the first and the higher order BPFs (as it is possible to see in Figure and Figure), nevertheless it is not always true for all the BPFs, as it is possible to see with the (8,0) mode for the 4th BPF. Figure 47 compile the effect of the rotor-stator spacing on (2,0), (4,0) and (6,0) interaction modes PWL values, these modes power are, in general, decreased, as expected by the pattern on the BPFs.

Figure 47: Interaction modes (2,0), (4,0) and (6,0) compared to rotor-stator spacing for some throttling configurations (4250 rpm).

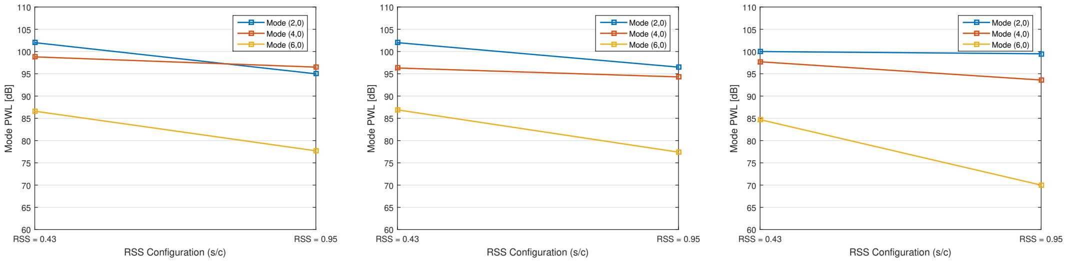

(a) Open throttle.

(b) Throttle at 25%.

(c) Throttle at 40%.

Source: Elaborated by the author.

Figure 48: Averaged spectra for multiple inflow configurations, fan speed of 4250 rpm and open throttle.

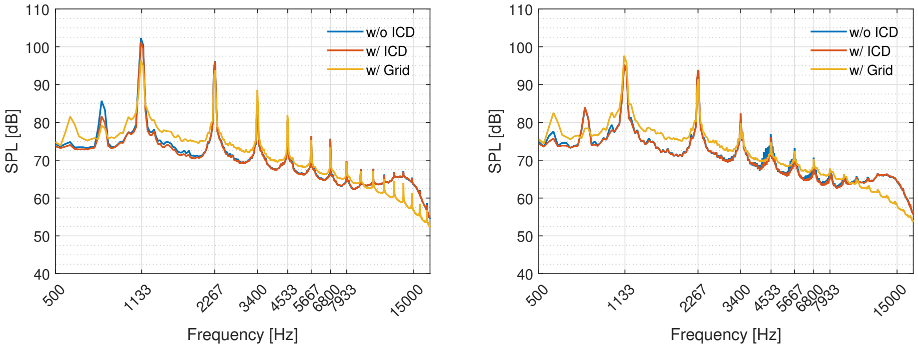

(a) RSS=0.43.

(b) RSS=0.95.

Source: Elaborated by the author.

Figure 49: Averaged spectra for multiple inflow configurations, fan speed of 4250 rpm and RSS = 0.43.

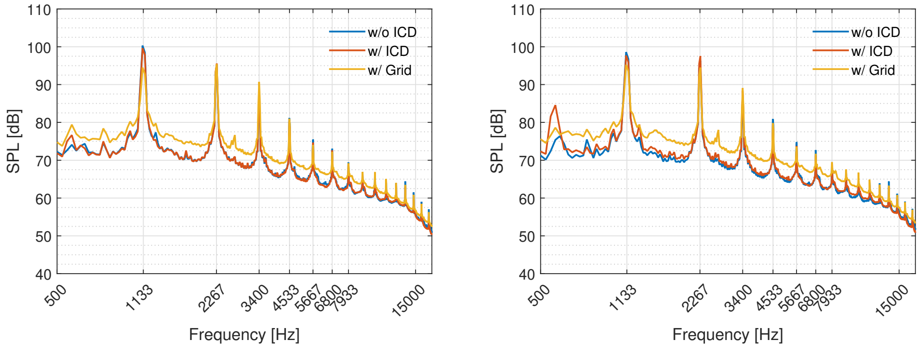
(a) 40% throttle.

(b) 50% throttle.

Source: Elaborated by the author.

5.5.4 Effects of Inflow Condition

Figure 48 shows the averaged spectra for the three different inflow conditions and at two different RSS configurations (left and right). It is hard to spot any difference regarding the placement of the ICD at the duct inlet, but the turbulence grid has a strong effect over the spectra. It works also as an area restriction device and the reduction on the axial speed shows the same effect of making the bubble disappear. Also, differently from the throttling screen, it increases the broadband level significantly. Figure 49 shows the same behaviour for other throttling configurations. Not much changes in the grid behaviour, but the few decibels that the blue curve had above the red curve in Figure 49 between first and second BPF disappears and it is actually reverted at 50% area restriction.

Figure 50: Averaged spectra for multiple inflow configurations, fan speed of 4250 rpm and 40% throttle.

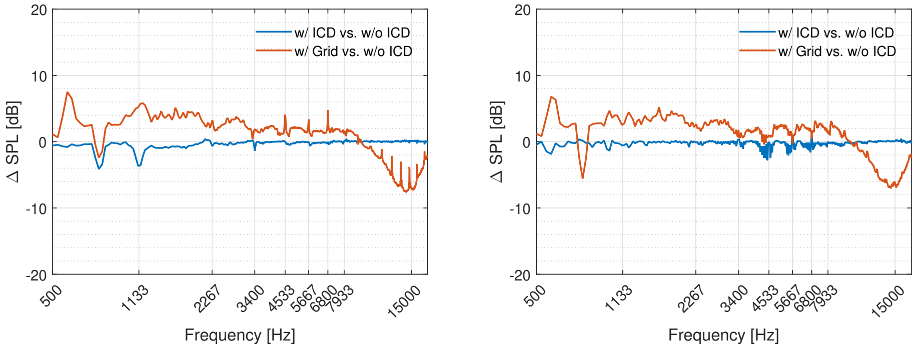
(a) RSS=0.43.

(b) RSS=0.95.

Source: Elaborated by the author.

Figure 51: Analysis of the effect of inflow condition on broadband noise for multiple throttle configurations.

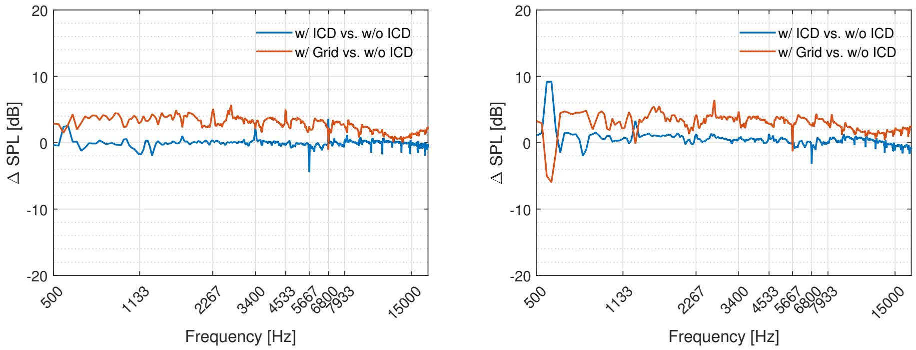

(a) 40% Throttling.

(b) 50% Throttling.

Source: Elaborated by the author.

Figure 52: Integration of broadband noise for different inflow conditions (RSS = 0.43, 4250 rpm and open throttle).

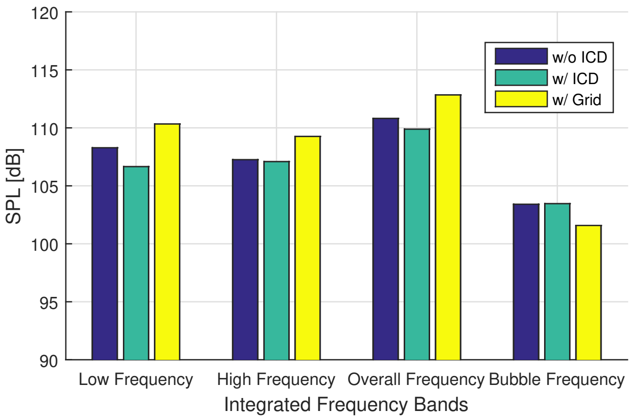

Source: Elaborated by the author.

Figure 50 and 51 show the variation of the broadband level for the previous spectra. The most important things to observe are that, in fact, the turbulence screen makes the bubble disappear and that the broadband level increase is almost the same throughout the spectra (around 4dB). Figure 52 shows the broadband integration of the spectra comparing the three inflow conditions. The slight difference suggests that the ICD reduces broadband level as expected. Figure 53 shows the effect on the BPF tones. No big differences are found for the ICD placement configuration, but the BPF are greatly reduced by the addition of the turbulence grid. Figure 54 show the effect of the inflow conditions on the on the modal decomposition for the first three BPFs. It is possible to see that for the first two BPFs,

Figure 53: Analysis of the BPFs tone levels and overtone (their sum) (RSS = 0.43 and 4250 rpm).

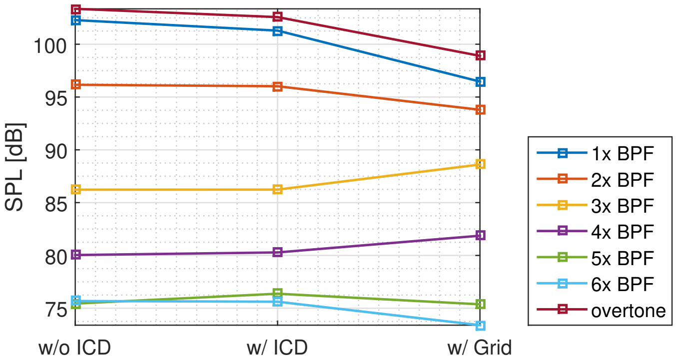

Source: Elaborated by the author.

Figure 54: Modal decomposition at fundamental tones for Inflow Condition (open throttle and 4250 rpm).

(a) 1st BPF with Inflow Condition = 0.41.
(b) 1st BPF with Inflow Condition = 0.95.
(c) 1st BPF with Inflow Condition = 0.95.

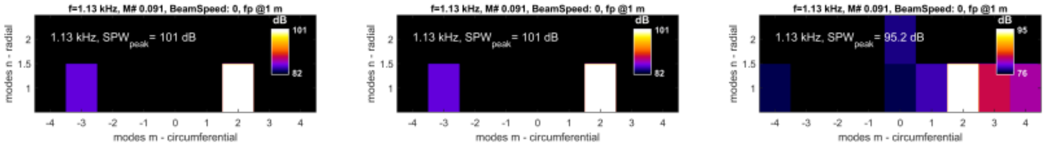

(d) 2nd BPF with Inflow Condition = 0.41.
(e) 2nd BPF with Inflow Condition = 0.95.
(f) 2nd BPF with Inflow Condition = 0.95.

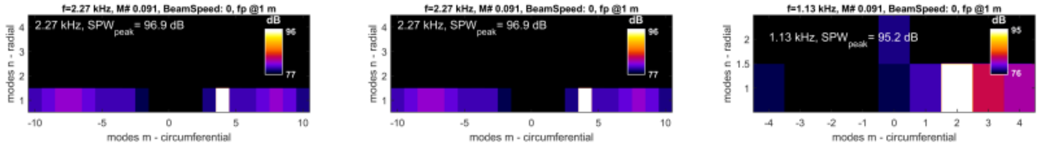

(g) 3rd BPF with Inflow Condition = 0.41.
(h) 3rd BPF with Inflow Condition = 0.95.
(i) 3rd BPF with Inflow Condition = 0.95.

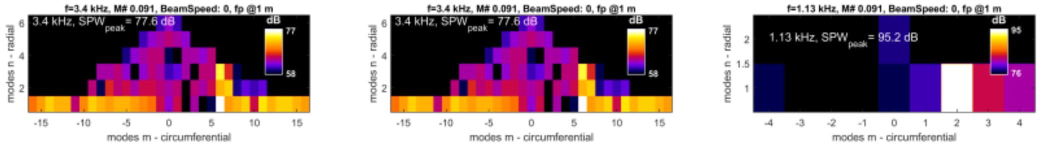

Source: Elaborated by the author.

there is not much effect on the PWL of the interaction modes due to ICD placement, but the turbulence generator grid does reduce their levels.

5.6 Summary

A parametric campaign was carried out exploring the effects of fan rotational speed, fan loading and rotor-stator spacing. Shaft speed effect was already studied at the EESC-USP Fan Rig, but, nevertheless, we could again observe increase in both tones and broadband with the increase of rotational speed. Other expected effect was the increase in mass-flow with rotational speed, which also happened. Throttling had a great impact on the mass-flow within the Fan Rig, higher throttling led to low dynamic pressure, as expected. On this study we could observe the effect of the rotor-stator spacing in tonal noise, an increase of spacing led to a decrease on the BPFs levels. For quantifying this effect, overtone, defined here as the sum of the SPL from the BPF and the first 4 harmonics, was introduced and doubling the spacing led to an average decrease of 4dB. As spacing is increased, higher harmonics drop more rapidly, shifting the spectrum to the first two harmonics, this effect comes from the smoothing of the blade wakes. Broadband was not much affected by the spacing between rotor and stator, apart from a region of high frequencies. Rotor-stator spacing did not affect the mass-flow either. The tones and broadband levels did not change much in absolute terms, but considering the decrease in velocity, higher loading led to “extra noise”. Some interesting features could be observed:

1. The high frequency “bubble” disappears with higher blade loading
2. For some speeds there is a strong tone before the BPF, this could be a mechanical noise which appears when a natural frequency of the system is excited
3. There are high frequency tones unrelated to shaft speed, they could be aerodynamic, like cavity noise.

6 INSTRUMENTED STATOR VANE

6.1 Introduction

Measurements of unsteady pressure over stator vanes are scarce in literature. Mueller (1984) has published results of stator-vane fluctuating pressures for both static and flight tests. Others studies, at NASA's Advanced Noise Control Fan (ANCF), Sutliff, Heidelberg e Envia (1999) compared the duct modes power level results measured by his rotating rake at the fan inlet and exhaust with what would be obtained by getting the surface pressure on the stator vane and using Green's functions model to predict the noise, finding good prediction accuracy. At NASA's Source Diagnostic Test (SDT), Envia (2002) separated the blade passing frequency and broadband contents of the signal obtained and found correlations of the tip speed and the increase in broadband level and indications of broadband homogeneity.

The research mentioned above use Kulite pressure sensors for measuring unsteady pressure in such a confined space, but due to their complexity these sensors have prohibiting prices. Other types of transducer or measurement methods can be used, as, for instance, hot-film anemometry or pressure sensitive paint. Nevertheless, measurements taken using microphones are straightforward and, in this work we propose the use of Micro-Electro-Mechanical Systems (MEMS) microphones. Advancements in telecommunication industry and the search for small and cheap electronics that have their use widely spread affected many other research areas. With large scale production, these miniaturised microphones became accessible.

6.2 Design of the Instrumented Stator Vane

The instrumented stator vane used in this work was designed using recently available technologies, as fused deposition modelling (FDM), 3D printing and the use of MEMS microphones. In this section some considerations regarding the use of these methods is discussed.

The choice for using MEMS microphones was due to two main factors. First, in this device there is a strong need for small sized transducers, which reduces the range of available sensors. MEMS microphones can be as small as 2.5x3.5x1.5 mm, which make them suitable for this need. Secondly, comparing to other options, they are inexpensive, disposable, electronic components which allow for higher risks in design in such confined space. Furthermore, MEMS microphones are easy to find and optimised for human audible frequencies. On the other hand, when using this type of transducers, it is necessary to design an interface circuit and their calibration is not as straightforward as off-the-shelf microphones, since they do not have a broad flat free field response. Also,comparatively, MEMS microphones have lower acoustic overload point (AOP) and signal-to-noise ratio (SNR).

Figure 55: Manufactured parts of the stator vane using FDM (fused deposition modelling) 3D printing.

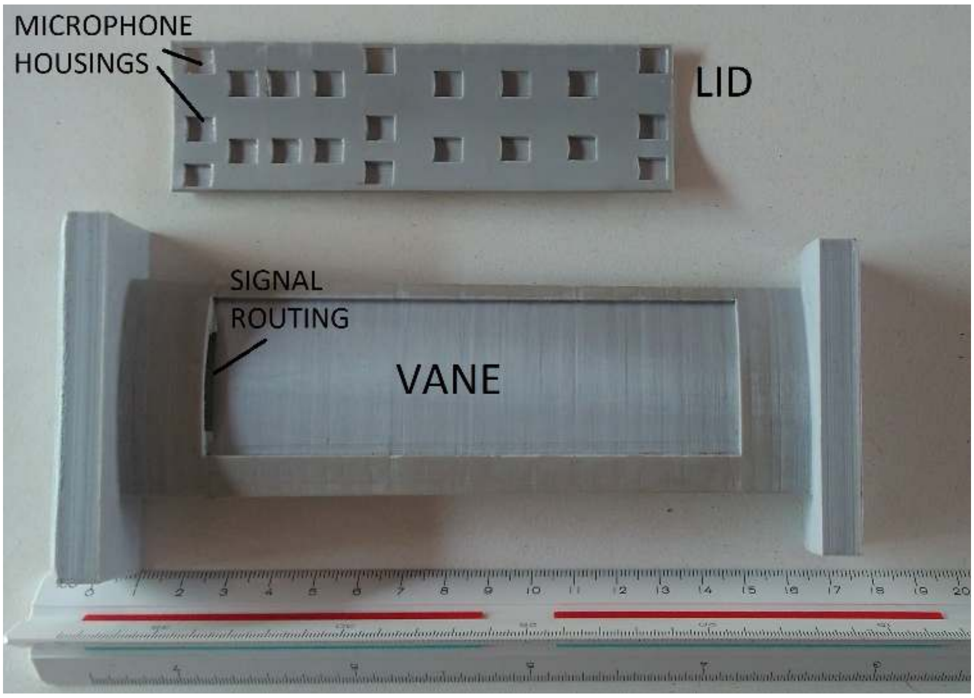

Source: Elaborated by the author.

The vane was designed in two parts, the main body and a lid, that can be seen in Figure 55. The body follows the design of a regular vane used in the stator assembly, but has a dug area to embed a flexible circuit board (FCB) in which surface mounted microphones are soldered; the signals from the microphones are routed out of the vane via the FCB through a hole which leads to the outer side of the wind tunnel. The lid has small cavities to accommodate the MEMS microphones and fit the dug area in the main body. After lodging the FCB in the vane main body, the lid was positioned and closed. A layer of epoxy resin was added and surface finishing was accomplished by sandpapering. Finally, the vane was painted and holes were pierced in it so that they match the position of the MEMS cavities (final assembly can be seen in Figure 56).

In our experiment, the frequency range of interest is from 200 to 10 kHz and the maximum SPL is lesser than 120 dB and the chosen MEMS microphone was the SPM0406HE3H-SB [6]. This is a miniature, high performance, low power microphone. Its typical free field response normalised to 1 kHz stays within ±1 dB from 200 to 6 kHz and within ±3 dB from 100 to 10 kHz. Its sensitivity is within -25 and -19 dBV/Pa, the total harmonic distortion (THD) is 1% and its signal-to-noise ratio is 59 dB(A-weighted) at 1

Figure 56: Final assembly of the stator vane, after surface finishing, and microphones enumeration.

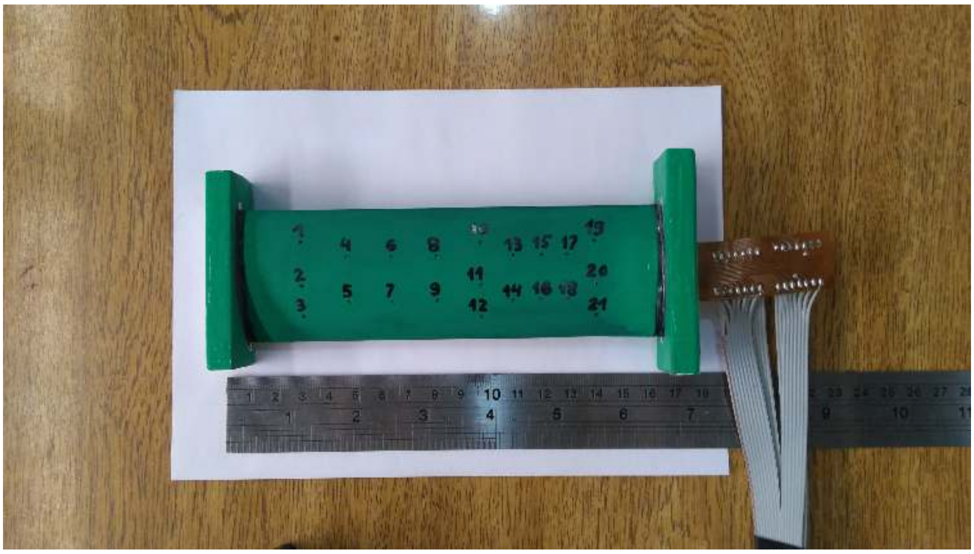

Source: Elaborated by the author.

kHz and sound pressure level (SPL) of 94 dB. At 1 kHz, limiting to 10% THD, supplying 5.5V and using 0 dB gain, the minimum acoustic overload point is 115 dB, therefore this microphone corresponds to the needs. Also, the maximum thickness acceptable should not be greater than 2mm and this microphone is only 1.25mm thick.

Figure 57: Electronics design of the flexible circuit board.

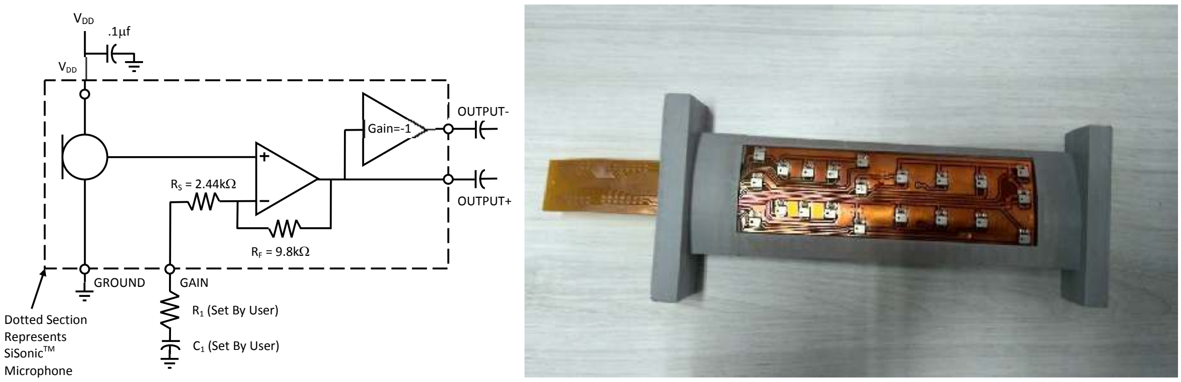

(a) Circuit scheme for each microphone.

(b) Embedded circuit board mounted within the stator vane.

Source: Knowles Electronics (2016) and the author.

The circuit board was designed and manufactured in-house, following instructions of the design guide and datasheet provided by the MEMS microphone manufacturer. The electronics design was set to have no gain, in order to have maximum acoustic overload point (AOP), delaying as much as possible saturation of the transducer signal. The circuit scheme used for each microphone is shown in Figure 57a, it consists of an energy supply, V_{DD}, for the microphones which was set to $5\,V$DC, a filtering capacitor, surface mounted (SMD), put next to the MEMS ($0.1\,\mu F$). Microphone signal was routed single-ended to the acquisition board using OUTPUT+ pin and connecting it to pin GAIN, without using R_1 and C_1, so that the gain was set to 0 dB. Pin OUTPUT- was ignored. This block was reproduced for the 21 microphones, and then it was printed in a flexible circuit board which was later corroded. The SMD components (the microphones and filtering capacitors) were soldered with the use of a re-flow oven and the final result can be seen in Figure 57b. The profile of temperatures was taken from the design manual of the MEMS microphone.

6.3 Data Processing

Microphone measurements of unsteady pressures over surfaces of stator vanes have two main components in its noise spectra. The first is a periodic, coherent component related to shaft speed, blade passages and blade-to-blade variations. The second is an incoherent, broadband component related stochastic phenomena, like turbulence. The analysis of the spectra should be done using individual levels of these components and, therefore, their separation is important for properly assessing noise control techniques and for validating numerical simulation codes. There have been several ways explored in the literature to separate a periodic component of a composite signal. For aeroacoustics applications, several methods have been used extensively: spectral methods, phase-averaging, Vold-Kalman filter and Sree's Methods.

Spectral methods comprehend all sort of methods that take as input the noise spectrum and treat its data in order to “chop off” the tones and consider as broadband what is left. These methods include peak finding methods, as performed by Stephens e Envia (2011), where the tone levels are substituted by interpolated values; moving median filters (PARRY; KINGAN; TESTER, 2011); deletion of FFT components of determined frequencies (CALDAS et al., 2016a); and so on. These spectral methods are robust, easy to use, and fast at the cost of being subjective, i.e. they are completely deprived of meaning. Phase-averaging consists of having measurements that accounts for the shaft rotations: tachometers, encoders, hall sensors. The revolution can be synchronised using this signal and, from the noise time series the periodic component can be obtained by ensemble averaging each revolution data. This has been used by (ENVIA, 2002), since this method provides the time series as output and, therefore, can be used for correlation calculations. Stephens e Vold (2014) used a Vold-Kalman Filter to extract the time histories of harmonics relative to one or more shafts. It is a convoluted method that can extract tone for multiple rotors even when they have different instant rotation rate and works when phase-averaging fails. It does so by calculating the best relation between structural equations and data equations, i.e. adjusting expected behaviour to observed behaviour, as in famous Kalman

Filters. This method is considerably slower than other, and also require the use of an encoder signal. Sree and Stephens developed methods for extracting the tone without the use of a rotation rate signal. Sree (2013), Stephens e Sree (2014) introduce a new method in which it is possible to obtain the two components from the time series without using an encoder signal. The method relies on synchronising the data correspondent to each rotation by calculating the auto-correlation between successive revolutions and obtaining the drift, as the number of samples corresponding to maximum auto-correlation value. Later, Sree e Stephens (2016) introduce an improved version of this method, that integrates with the spectral estimation calculation and outputs the broadband spectrum directly. Table 5 compiles a summary of the different methods for proceeding with tone-broadband separation.

Table 5: Comparison of Tone/Broadband Processing Methods

	Spectral Methods	**Phase Averaging**	**Order Tracking**	**Sree's Method**
Application	Any	Single shaft	Multi-shaft	Any
Input	Frequency spectrum	Time series	Time series	Time series
Output	Frequency spectra	Time series	Time series	Frequency spectra
Encoder Required	No	Yes	Yes	No
Processing Speed	Fastest	Medium	Slowest	Fast
Other Advantages	Robust	Well defined	Quantifies tone coherence with each shaft	Parameter free
Other Disadvantages	Ad-hoc, subjective		May require filter bandwidth tuning	Only accounts for dominant frequency and harmonics

Source: Stephens e Sree (2014).

For the instrumented stator vane analysis in the EESC-USP Fan Rig, phase-averaging was the chosen method for tone-broadband separation, since a hall sensor signal was acquired simultaneously to the acoustic measurements and also because it outputs a time series signal, therefore, enabling auto-correlation analysis, fundamental to obtaining data for integral length scale calculations.

6.3.1 Phase Averaging using Hall Sensor Signal

Phase-averaging can be done by cutting the signal into ensembles of samples corresponding to a single rotation, overlaying this ensembles and averaging them. As the broadband noise is of random nature, by doing this average it is zeroed and thus we obtain only the periodic component as a result. Note that this periodic component contain more than the harmonics of the BPF, it contains any blade-to-blade variation associated periodicity. To obtain the broadband component, a subtraction of this periodic part repeated for every revolution from the original time series can be done.

Figure 58: Segment cutting process for phase-averaging method without signal alignment.

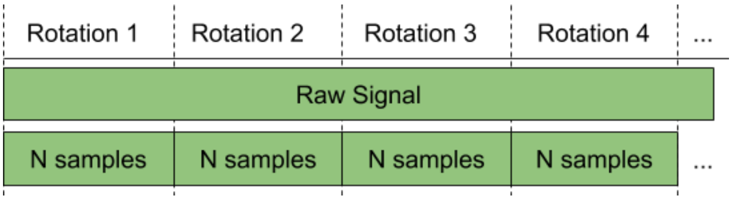

Source: Elaborated by the author.

To separate the tonal content from the signal obtained at any given experiment, one can phase-average it. To do so, the signal should be cut into a set of samples with the size of a rotor revolution (as shown in Figure 58). This task is not straightforward, because it would result in sets of samples containing the periodic data, as shown in Figure 59. In this figure, the x-axis is limited to the number of samples corresponding to a fan rotation. Each of the the stripes shows the pressure peak from a blade passage (16 per rotation, same number as blade counting), which are not aligned. As these sets need to be summed up and then divided by the revolutions count, this nonalignment would cause the average to fail and tend to zero. This data nonalignment is caused by jitter (time intervals between samples can have small differences and the rotor speed is not exactly constant, i.e. it can drift) and this should be assessed in order to properly sum the data and divide by the number of revolutions, while accounting for all tonal content.

Figure 59: Raw signal (i.e. unaligned) time series.

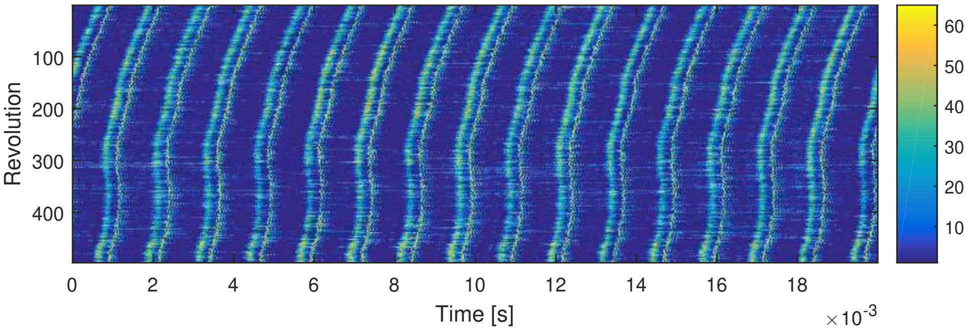

Source: Elaborated by the author.

To measure this jitter effect and mitigate its effect on the averaging, a Hall effect sensor was used with a magnet glued to the shaft. Raw data from this sensor consists of square signals corresponding to the magnet passage by the sensor. This data is processed by transforming into one-zero signal with one being exactly the moment when the signal change from low to high value as exemplified by Figure 60a where, in blue, the raw signal is measured as a step signal, every time the rotor completes a full rotation. In black, the signal is transformed into a pulse signal. The number of samples corresponding to

Figure 60: Processed sensor Hall signal into samples-per-revolution and accumulated jitter.

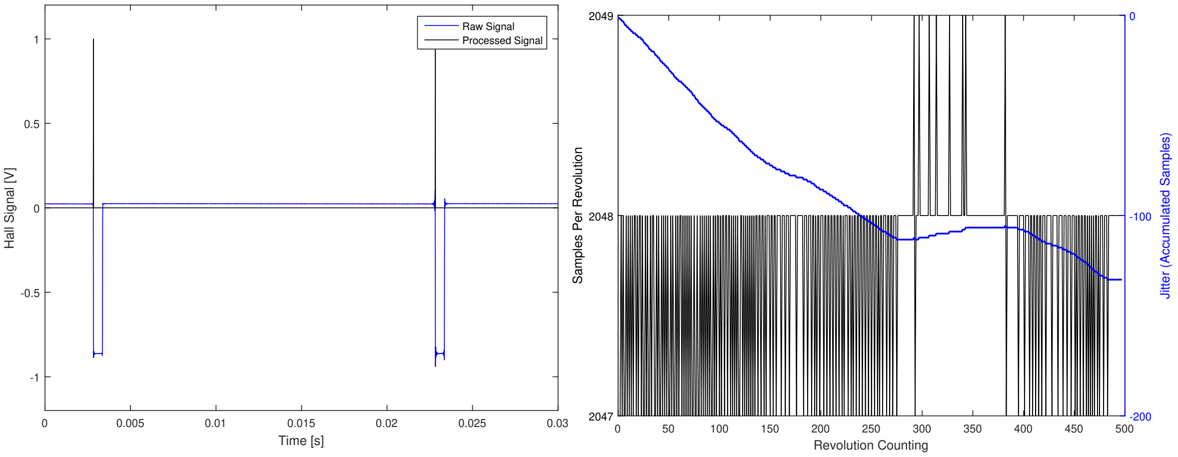

(a) Hall signal.

(b) Samples-per-revolution (SPR) and accumulated jitter.

Source: Elaborated by the author.

each revolution and the accumulated jitter over one experiment acquisition is shown in Figure 60b. The difference, in samples, between the pulses in processed sensor hall signal is counted and shown in black for each individual revolution. The accumulated sum of the difference the measured and averaged samples per revolution, known as jitter, is plotted in blue. This allows to count the number of samples that correspond to each revolution of the fan. It is possible to see that the number of samples per revolution (SPR) oscillates between 2047 and 2049, being 2048 the expected value.

Figure 61: Segment cutting process for phase-averaging method using processed hall sensor signal for microphones signal alignment.

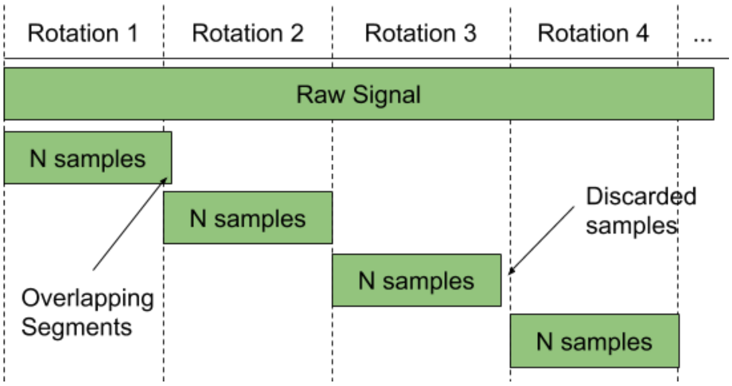

Source: Elaborated by the author.

The segment cutting process using the processed Hall sensor signal is shown in Figure 61: if the SPR is lower than expected, the missing sample needs to be borrowed from the next interval. Alternatively, if it is higher, the extra sample needs to be discarded.

Figure 62: Phase-averaging the signal.

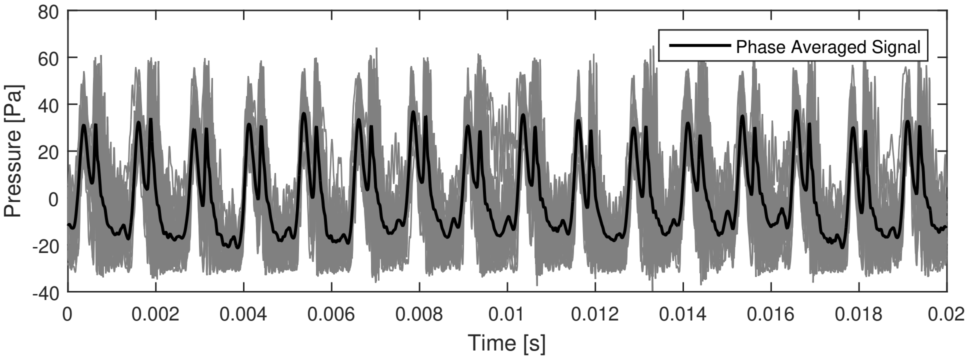

Source: Elaborated by the author.

Figure 63: Microphones signals time series after alignment.

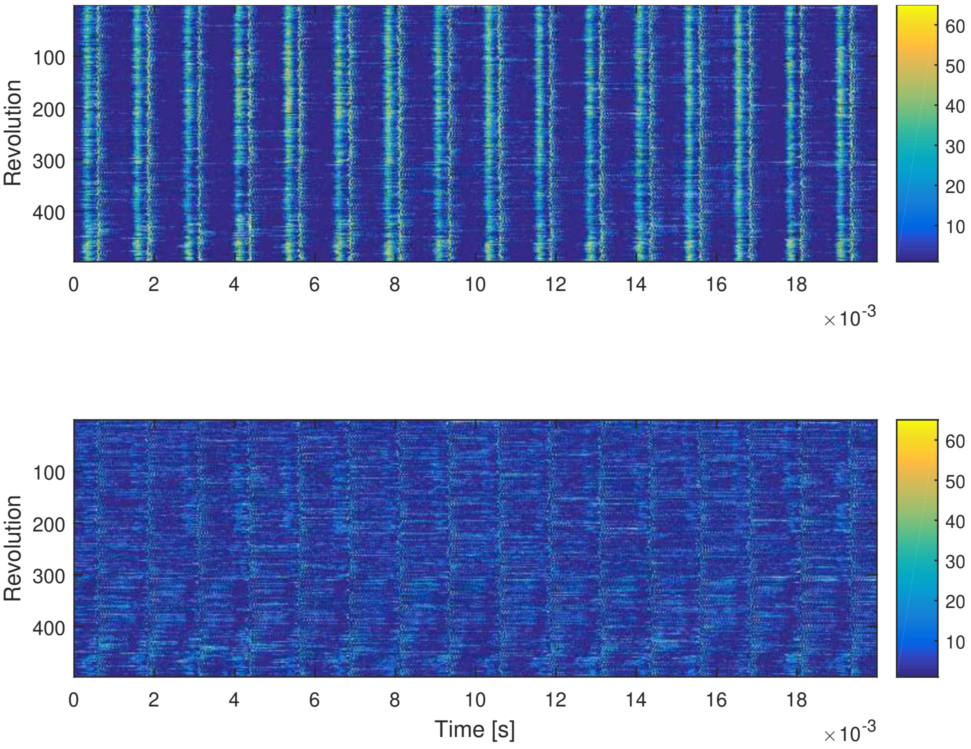

Source: Elaborated by the author.

By doing this, one can obtain the aligned sets of data and average them out to obtain the periodic phase-averaged time series, as seen in Figure 62. In this figure, the grey curve shows signals from all revolution are superposed and, in black, their average is shown. Figure 63 shows the aligned raw signal and its broadband component, which is obtained by subtracting the periodic phase-averaged signal from the raw signal. The x-axis is limited to the number of samples corresponding to a fan rotation. Each of the the stripes show the pressure peak from a blade passage (16 per rotation, same number as blade counting).

Upper image shows complete (tonal + broadband signal) and lower image shows the time series after removal of periodic signal.

Figure 64 shows the spectral separation process.First image (up) shows the complete spectrum, both coherent and incoherent components, of a measurement. Second image (centre) shows the separation of the spectrum into two parts, broadband component - incoherent - (in blue) and tonal spectra - the periodic, coherent to rotor revolutions - (in black). Third image (down) shows the extraction of BPF spectrum: in it the periodic component, which contain noise generation related both to blade passages and blade-to-blade differences, is phase-averaged once again, to the period of one blade passage, and the BPF spectrum is then extracted. It is possible to double check that the broadband hump do not contain periodic signal by increasing the refinement in the frequency resolution and checking if the power associated with the BPF frequency does not increase.

Figure 64: Separation of tonal and broadband components of noise spectrum.

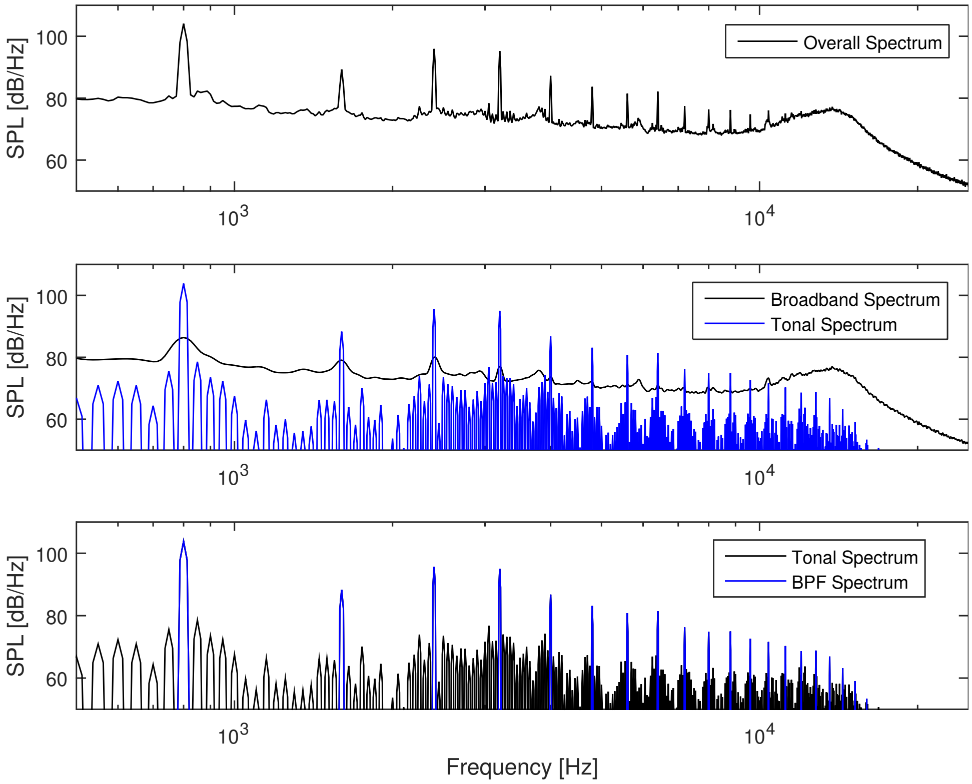

Source: Elaborated by the author.

6.4 Experimental Procedure

For the instrumented stator vane analysis, the priority was to run a great range of rotational speeds for a single condition. The baseline condition chosen was rotor-stator spacing of 0.43 (0), no ICD (0), no throttling (1). For this configuration, fan speeds from 4250 to 2000 rpm, with steps of 250 rpm (1-10), were tested. Also, some tested were done using throttling of 25% area restriction and with the addition of the ICD. In this Campaign, the the first two rings of the inlet microphone antenna and the 21 microphones embedded in the stator vane were used. Table 12, in the Appendix C, contains the test matrix of the experiments, with all the configurations actually tested. Finally, for this tests a *in loci* calibration method was done using an NC-74 RION Sound Calibrator and putting its tube in touch with the vane surface after the installation of the MEMS microphones within it.

Figure 65: Effect of fan tip speed for average broadband level in vane MEMS microphones and in inlet wall-mounted microphone (B&K Microphone Type4958).

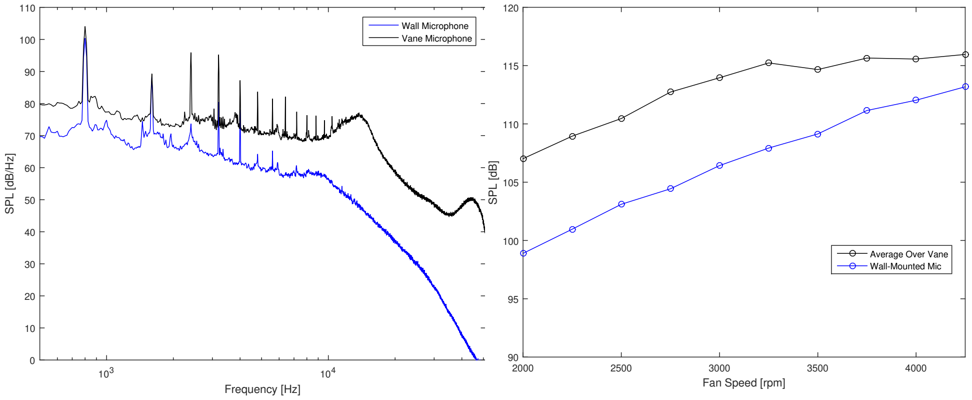

(a) Shift in spectra broadband level.

(b) Effect of fan speed on average broadband levels.

Source: Elaborated by the author.

Figure 65a compares the spectra of two microphones, one, a B&K Microphone Type 4958, mounted in the antenna array and one, a MEMS microphone, within the stator vane. Obviously, as the vane microphone is much closer to the noise sources, the power level is higher and the spectrum appears shifted up. Also, there are some amplification effects present in the spectrum of the vanes microphones at frequencies higher than 10 kHz. The first bump (from 10 to 20 kHz) is due to a cavity effect (Helmholtz cavity) due to the fact that MEMS microphones have a housing to the sensing membrane. The second bump should have a similar explanation but no literature was found in this effect.

6.5 Experimental Results

After the spectral separation into broadband and tonal components is done, broadband levels can be analysed separately. In this work, these levels are condensed into a single value by integrating the spectra from 10 Hz - to avoid low frequency noise contamination due to limited acquisition time - to 12 kHz - which allows capturing overall trend but avoids considering the cavity resonance effect, present in high frequencies. For this analysis a wall-mounted microphone, installed at the inlet antenna, and two span lines are considered (at 30% and 63% chord). The analysis firstly uses the spectra of the microphones in order to observe the effect of the rotational speed on the averaged levels and its distribution over the vane. Later, data time-series is used to observe the effect of rotational speed on zero-delay cross-correlation coefficients and integral length scale for the microphones distributed over the mentioned span lines.

Figure 66: Distribution of integrated broadband level for microphones over two span lines and three different fan speeds.

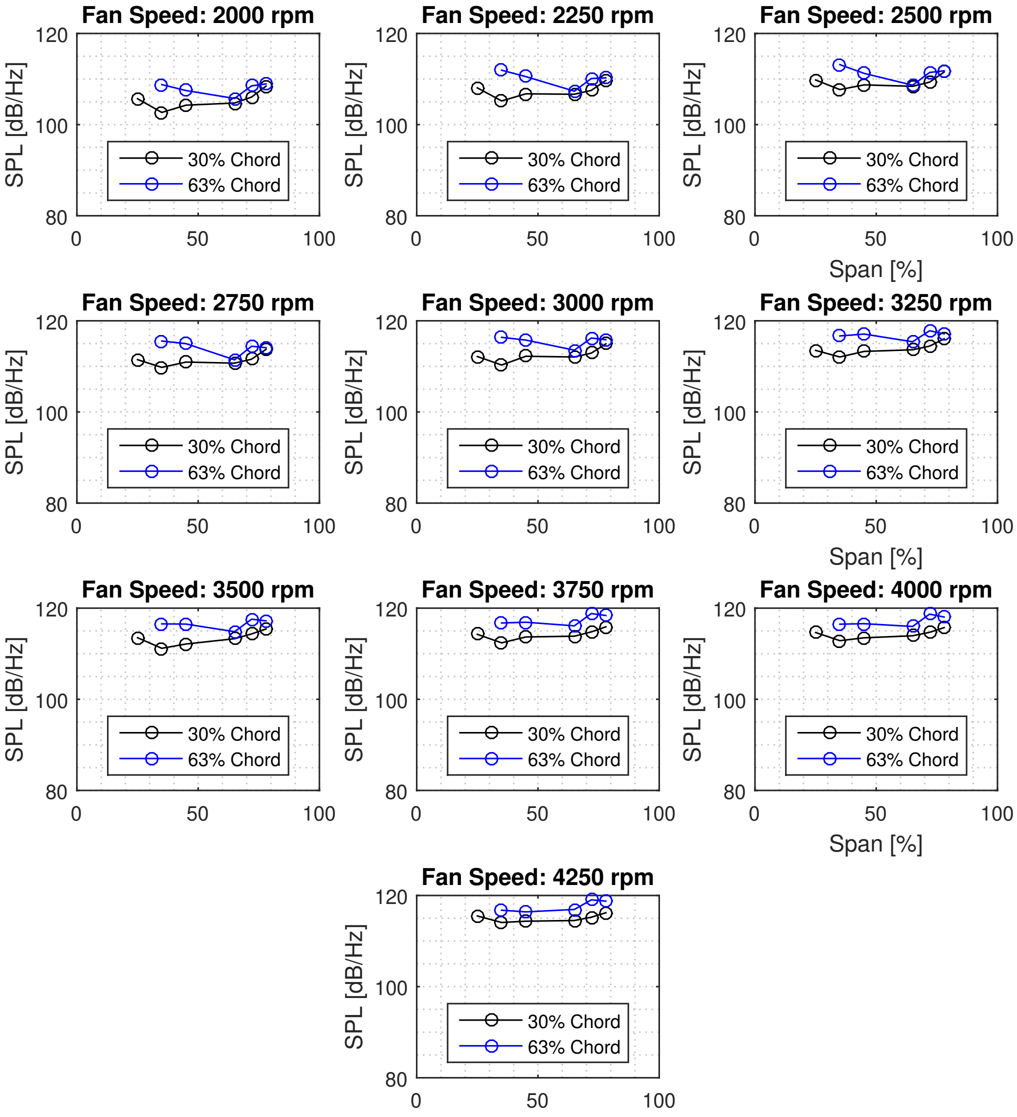

Source: Elaborated by the author.

Figure 65b shows the effect of the increase in fan speed in the averaged level over the vane and for a wall mounted microphone. It is possible to see a trend of increasing level with fan speed, but for higher speeds the increase amount diminishes for the vane microphones. This could be a physical limitation of the transducer, i.e. acoustic overload point could have been reached, since the trend does not change for the wall mounted microphone. Figure 66 shows the distribution of the integrated broadband level for two span lines (at 30% and 60% chords) and for three fan speeds. It is possible to see that the distribution is almost flat over the vane, with a levels little lower mid-vane. Also, as in Figure 65b, it is possible to observe that the levels increase with speed, the new information is that the shape of distribution maintains itself for all three speeds.

Figure 67: Auto-correlation and cross-correlation comparing the signals from microphone 18 and microphones distributed over its span line (itself and microphones 16, 14, 9, 7, and 5).

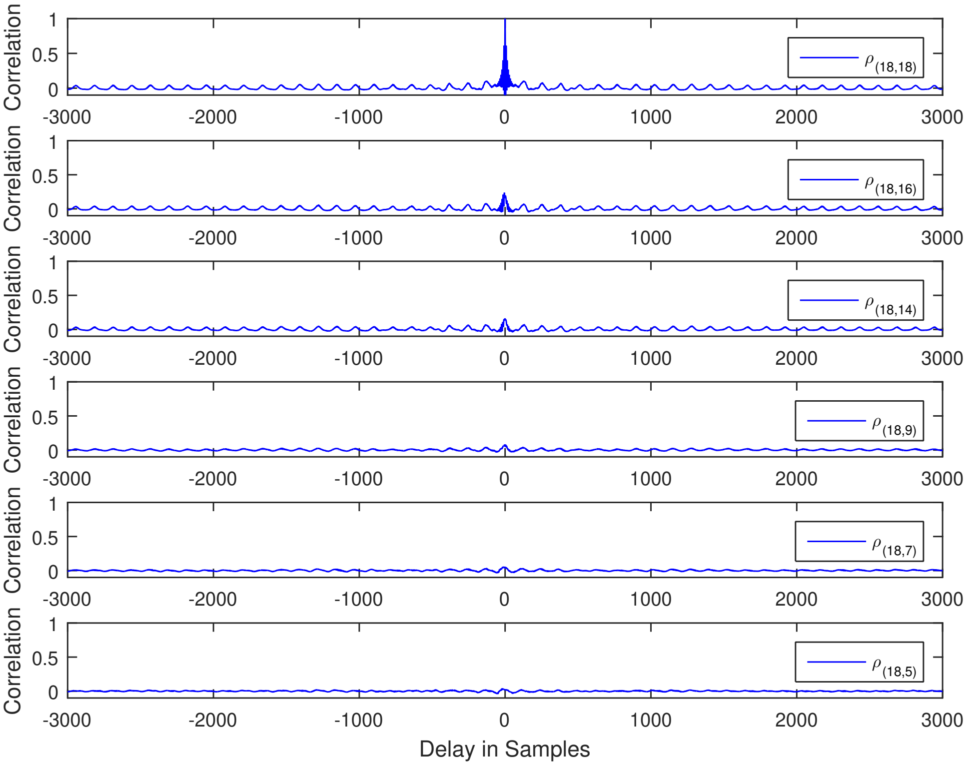

Source: Elaborated by the author.

Figure 67 shows the correlation coefficient comparing multiple microphones along a span line. The coefficient $\rho_{(i,j)}$ corresponds to the cross-correlation between microphones i and j according to the delay of the signals in samples (function *xcorr()* in Matlab). The figure shows that the farther apart microphones are from each other, the lower is the value of the zero-delay correlation coefficient (peak value in the centre of the graphs). As expected, the peak value is reduced with greater spacing, because broadband pressure oscillations are localised and have small wavenumber. The presence of the peak near zero delay also indicates that this is a acoustic phenomenon, i.e. its information speed is greater than flow speed.

Figure 68 shows the levels of the mentioned peaks, i.e. zero-delay correlation coefficient value, reducing as the microphones distance grows. As speed is increased the curve is shifted down and correlation disappears for smaller distances. Figure 69 shows

Figure 68: Zero-delay auto-correlation and cross-correlation comparing the signals from microphone 18 and microphones distributed over its span line (itself and microphones 16, 14, 9, 7, and 5) for three different fan speeds.

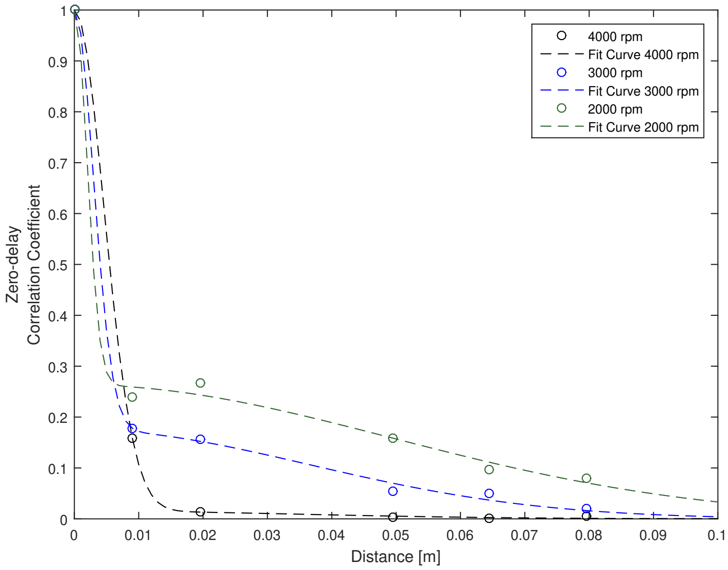

Source: Elaborated by the author.

Figure 69: Effect of fan tip speed in pressure integral length scales, which are obtained by integrating the fit curves from zero-delay correlation coefficient over two span lines (at 30 and 63% chord).

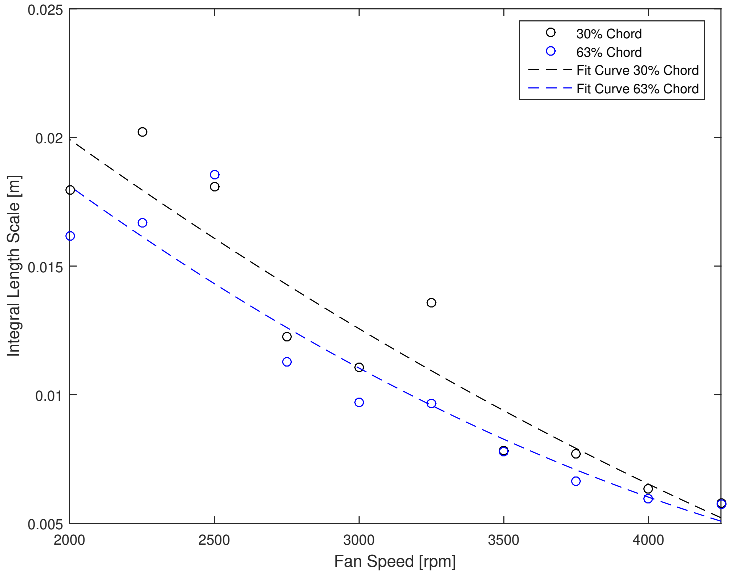

Source: Elaborated by the author.

the effect of increasing the fan speed in the integral length scale. The integral length scale is obtained by integrating the zero-delay coefficient up to the distance where it loses the correlation completely (i.e. becomes nearly zero). In here, this integration was obtained by calculating the area below the curves that better fit the points. In this best fit calculation a bi-Gaussian function with zero means was used, so that the curves ares represented by two standard deviation values.

Two different span lines and the microphones along them were considered and compared. The trend lines make clear the decrease of length scale with the increase in fan speed, just as shown in last figure and what was observed in the experiments done by Envia (2002). In this reference article, a homogeneous pressure field is also hypothesised from the little difference between the spatial coherence in spanwise and chordwise directions. Here, the deviation of the data points from the fit curves makes it possible to believe that both curves are close enough to indicate homogeneity spanwise as well. Nevertheless, more data in different directions should be assessed to better support this evidence.

6.6 Summary

In this work, the use of MEMS microphones was proposed as an alternative fan noise aeroacoustics measurements sensor. A measurement device was designed and manufactured to achieve this goal. The chosen MEMS microphones provide an almost flat response in the frequency bands of interest and were calibrated *in loci* using an appropriate calibrator. The measured signals were processed in order to separate tonal and broadband components using a hall sensor signal and phase-averaging technique. Measurement results obtained using MEMS microphones were compatible to more expensive alternatives even without multi-frequency calibration. The drawback is that for high fan speeds, as the pressure oscillations are too high, the acoustic overload point might have been reached as the broadband levels stop increasing, indicating transducer saturation. Broadband level distribution was measured in two span lines of the instrumented stator vane and in one of the antenna microphones. It was possible to notice that the broadband levels increased with the increase in fan speed and that its distribution over these span lines maintained its shape for different speeds. Cross-correlation of the microphones were calculated and showed decay of zero-delay cross-correlation with increase in distance between microphones. The integral length scale, obtained by the integration of zero-delay cross-correlation curve, showed decay with increase in fan speed and both span lines presented similar values of the integral length scale, indicating broadband homogeneity span-wise. These results come to contribute to the understanding of the broadband noise generated by rotor-stator interaction in turbofan engines.

7 CONCLUSION

This chapter contains a brief compilation of this dissertation main conclusions for each of the experimental campaigns and a list of suggestions for future work in this research framework.

7.1 Overview

The Department of Aeronautical Engineering of the São Carlos School of Engineering (EESC) at the University of São Paulo (USP), in partnerships with other Brazilian universities and Embraer S.A., has been part of the Silent Aircraft and SILENCE research projects. These projects have the objective of understanding aircraft noise and developing new technologies to mitigate this issue. In this work, the focus was obtaining aerodynamic and acoustic experimental data from a subsonic fan installed in an aeroacoustics wind-tunnel, the EESC-USP Fan Rig. To do so, three experimental campaign were taken aiming to extend the knowledge of this workbench capabilities and to observe the effect that some parameters can have on noise generation.

A extensive campaign of experiments was taken to analyse the performance characteristics of the scaled-down ANCF geometry used in the EESC-USP Fan Rig. These experiments consisted of Pitot tube traversing - measuring dynamic pressure in a set of radial and circumferential positions-, static pressure measurements in several sections of the ducts, ambient pressure, temperature and humidity measurements, input electric power measurements, and fan speed measurements, that, altogether, make possible to calculate the performance quantities. This campaign was carried out to quantify the effects of controllable parameters on the aerodynamic characteristics of the flow. Starting from unrestricted flow to 70% area constraint, and a range of fan speeds, several flow measurements that could be translated into performance quantities were taken: volume flow rate, fan total and static pressures, compression ratio, total and net power, and efficiency. The measured compression ratio ranged from 1.00 to 1.02, with maximum axial Mach of 0.13 and maximum total efficiency of 65%. The surge effect, an unstable configuration characterised by rotor blades stall was also observed. Significant differences in fan performance due to the installation of an Inlet Control Device (ICD) and the rotor-stator spacing were not found, except under surge conditions. After stalling (at 50% throttling, each configuration reaches a very different mean volume flow rate, and the ICD has lesser effect than increasing rotor-stator spacing. Also, the effect of rotational speed is still the same and the volume flow rate scales linearly with the fan speed. Also, the flow quantities behave as expected, i.e. flow rate scaled with fan speed; fan total and static pressures with fan speed to the power of two; fan input and output powers with fan speed to the power of three.

A parametric campaign was carried out exploring the effects of fan rotational speed, fan loading and rotor-stator spacing. Shaft speed effect was already studied at the EESC-USP Fan Rig, but, nevertheless, we could again observe increase in both tones and broadband with the increase of rotational speed. Other expected effect was the increase in mass-flow with rotational speed, which also happened. Throttling had a great impact on the mass-flow within the Fan Rig, higher throttling led to low dynamic pressure, as expected. On this study we could observe the effect of the rotor-stator spacing in tonal noise, an increase of spacing led to a decrease on the BPFs levels. For quantifying this effect, overtone, defined here as the sum of the SPL from the BPF and the first 4 harmonics, was introduced and doubling the spacing led to an average decrease of 4dB. As spacing is increased, higher harmonics drop more rapidly, shifting the spectrum to the first two harmonics, this effect comes from the smoothing of the blade wakes. Broadband was not much affected by the spacing between rotor and stator, apart from a region of high frequencies. Rotor-stator spacing did not affect the mass-flow either. The tones and broadband levels did not change much in absolute terms, but considering the decrease in velocity, higher loading led to “extra noise”. Some interesting features could be observed:

1. The high frequency “bubble” disappears with higher blade loading
2. For some speeds there is a strong tone before the BPF, this could be a mechanical noise which appears when a natural frequency of the system is excited
3. There are high frequency tones unrelated to shaft speed, they could be aerodynamic, like cavity noise.

Finally, the use of MEMS microphones was proposed as an alternative fan noise aeroacoustics measurements sensor. A measurement device was designed and manufactured to achieve this goal. The chosen MEMS microphones provide an almost flat response in the frequency bands of interest and were calibrated *in loci* using an appropriate calibrator. The measured signals were processed in order to separate tonal and broadband components using a hall sensor signal and phase-averaging technique. Measurement results obtained using MEMS microphones were compatible to more expensive alternatives even without multi-frequency calibration. The drawback is that for high fan speeds, as the pressure oscillations are too high, the acoustic overload point might have been reached as the broadband levels stop increasing, indicating transducer saturation. Broadband level distribution was measured in two span lines of the instrumented stator vane and in one of the antenna microphones. It was possible to notice that the broadband levels increased with the increase in fan speed and that its distribution over these span lines maintained its shape for different speeds. Cross-correlation of the microphones were calculated and showed decay of zero-delay cross-correlation with increase in distance between microphones. The integral length scale, obtained by the integration of zero-delay cross-correlation curve, showed decay with increase in fan speed and both span lines presented similar values of the integral length scale, indicating broadband homogeneity span-wise. These results come to contribute to the understanding of the broadband noise generated by rotor-stator interaction in turbofan engines. Measurements of unsteady pressure over stator vanes are scarce in literature and there are few comparative reference.

7.2 Recommendations for Future Work

Improvements on the EESC-USP Fan Rig experimental setup are constantly being taken, next steps are already being taken by the manufacturing of a new rotor-stator geometry and new sets of stator rings. Also a treated wall configuration has been designed and is in tests at the present moment. All the data collected by this experimental setup should be useful for theoretical or empirical models that have been developed in parallel. From the point of view of this author, the following experiments, modifications and improvements would be valuable for future models:

- Measurement of turbulence level ingested by fan by traversing a hot-wire anemometer in the a duct section upstream to the fan. Also, using this measurements it will be possible to have more knowledge on the effect of placing the ICD and, in the future, design a new, more efficient, version.
- Measurement of the flow leaving the fan blades, characterisation of the wake and turbulence levels are fundamental for most models, since the impingement of these wake on the stator leading edges are the greatest contributor to subsonic fan noise.
- Parametric investigation can be extended by exploring the effects of blade pitch angle in comparison with throttling, larger rotor-stator spacing, other counts of fan blades and stator vanes, controllable casing boundary layer thickness, tip gap and ingested turbulence, and new swept and leaned vane configurations.
- Designed of an improved instrumented stator vane, with greater density of measurement points and simultaneous measurements of more than one instrumented vane, to improve correlation calculations

BIBLIOGRAPHY

ANNEX, I. 16" international standards and recommended practices. **Environmental protection**, v. 2, 2004.

BALOMBIN, J. R.; STAKOLICH, E. G. Effect of rotor-to-stator spacing on acoustic performance of a full-scale fan (qf-5) for turbofan engines. 1974.

BOZAK, R. F. **Advanced noise control fan aerodynamic performance**. [S.l.], 2009.

CALDAS, L. C. **In-duct beamforming and mode detection using a circular microphone array for the characterisation of broadband aeroengine fan noise**. 2016. Dissertação (Mestrado) — Escola politécnica da Universidade de São Paulo, São Paulo, Brazil, 2016.

CALDAS, L. C. et al. In-duct beamforming noise source estimation and mode detection at the university of são paulo fan rig. In: **AIAA-2015-2233, 21st AIAA/CEAS Aeroacoustics Conference**. American Institute of Aeronautics and Astronautics, 2015. Disponível em: <http://dx.doi.org/10.2514/6.2015-2233>.

______. Comparison of different techniques for rotating beamforming at the university of são paulo fan rig test facility. In: **BeBeC-2016-D14, 6th Berlin Beamforming Conference**. [S.l.: s.n.], 2016.

______. In-duct rotating beamforming and mode detection of fan noise sources. In: **AIAA 2016-3034, 22st AIAA/CEAS Aeroacoustics Conference**. American Institute of Aeronautics and Astronautics, 2016. Disponível em: <http://dx.doi.org/10.2514/6.2016-3034>.

CARLSON, J. F.; HEINS, A. E. The reflection of an electromagnetic plane wave by an infinite set of plates, i. **Quarterly of Applied Mathematics**, JSTOR, v. 4, n. 4, p. 313–329, 1947.

CUENCA, R. G. **Aeroacústica de motores aeronáuticos: uma abordagem por meta-modelo**. 2017. Tese (Doutorado) — Universidade de São Paulo, São Carlos, Brazil, 2017.

CUENCA, R. G.; CALDAS, L. C.; GRECO, P. C. Aero-acoustic fan broadband noise: A new parameterization proposal. In: **ICA2016-430, 22nd International Congress on Acoustics**. [S.l.]: International Commission for Acoustics, 2016.

CUENCA, R. G.; MARTINEZ, B.; GRECO, P. C. Parametric investigation of eesc-usp aeroacoustic fan rig. In: **ICAS 2018 Congress**. [S.l.: s.n.], 2018.

CURLE, N. The influence of solid boundaries upon aerodynamic sound. **Proc. R. Soc. Lond. A**, The Royal Society, v. 231, n. 1187, p. 505–514, 1955.

DOUGHERTY, R. P.; WALKER, B. E. Virtual rotating microphone imaging of broadband fan noise. In: **15th AIAA/CEAS Aeroacoustics Conference (30th AIAA Aeroacoustics Conference)**. American Institute of Aeronautics and Astronautics, 2009. Disponível em: <http://dx.doi.org/10.2514/6.2009-3121>.

ENGHARDT, L.; HOLEWA, A.; TAPKEN, U. Comparison of different analysis techniques to decompose a broad-band ducted sound field in its mode constituents. In: **13th AIAA/CEAS Aeroacoustics Conference (28th AIAA Aeroacoustics Conference)**. [S.l.]: American Institute of Aeronautics and Astronautics, 2007.

ENGHARDT, L.; NEUHAUS, L.; LOWIS, C. Broadband sound power determination in flow ducts. In: **10th AIAA/CEAS Aeroacoustics Conference**. [S.l.]: American Institute of Aeronautics and Astronautics (AIAA), 2004.

ENVIA, E. Fan noise source diagnostics test-vane unsteady pressure results. In: **8th AIAA/CEAS Aeroacoustics Conference & Exhibit**. [S.l.: s.n.], 2002. p. 2430.

ENVIA, E. et al. An assessment of current fan noise prediction capability. **AIAA paper**, v. 2991, p. 2008, 2008.

FARASSAT, F. Linear acoustic formulas for calculation of rotating blade noise. **AIAA journal**, v. 19, n. 9, p. 1122–1130, 1981.

GLEGG, S.; DEVENPORT, W. **Aeroacoustics of low mach number flows: fundamentals, analysis, and measurement**. [S.l.]: Academic Press, 2017.

GLEGG, S. A. L. The response of a swept blade row to a three-dimensional gust. **Journal of sound and vibration**, Elsevier, v. 227, n. 1, p. 29–64, 1999.

GLIEBE, P.; KANTOLA, R. Effects of vane/blade ratio and spacing on fan noise, volume 1. 1983.

GOLDSTEIN, A. W.; GLASER, F. W.; COATES, J. Effects of casing boundary-layer removal on noise of a turbofan rotor. 1972.

GOLDSTEIN, M. E. **Aeroacoustics**. [S.l.]: McGraw-Hill Inc.,US, 1976. ISBN 0070236852.

HEIDELBERG, L. Fan noise source diagnostic test-tone modal structure results. In: **8th AIAA/CEAS Aeroacoustics Conference & Exhibit**. [S.l.: s.n.], 2002. p. 2428.

HEIDELBERG, L. et al. A unique ducted fan test bed for active noise control and aeroacoustics research. In: **Aeroacoustics Conference**. [S.l.]: American Institute of Aeronautics and Astronautics (AIAA), 1996.

HEINS, A. E. The reflection of an electromagnetic plane wave by an infinite set of plates iii. **Quarterly of Applied Mathematics**, JSTOR, v. 8, n. 3, p. 281–291, 1950.

HEINS, A. E.; CARLSON, J. F. The reflection of an electromagnetic plane wave by an infinite set of plates, ii. **Quarterly of Applied Mathematics**, JSTOR, v. 5, n. 1, p. 82–88, 1947.

HOMYAK, L.; MCARDLE, J.; HEIDELBERG, L. A compact inflow control device for simulating flight fan noise. In: **8th Aeroacoustics Conference**. [S.l.]: American Institute of Aeronautics and Astronautics (AIAA), 1983.

HUBBARD, H. H. **Aeroacoustics of flight vehicles: Theory and practice. volume 1. noise sources**. [S.l.], 1991.

HUFF, D. L. **Fan noise prediction: status and needs**. [S.l.]: National Aeronautics and Space Administration, Lewis Research Center, 1997.

HUGHES, C. et al. Fan noise source diagnostic test-rotor alone aerodynamic performance results. In: **8th AIAA/CEAS Aeroacoustics Conference & Exhibit**. [S.l.: s.n.], 2002. p. 2426.

ICAO, I. Environmental report 2013. **Aviation and climate change**, v. 2013, 2013.

______. Environmental report 2016. **Aviation and climate change**, v. 2016, 2016.

ISO5801. **Industrial fans — Performance testing using standardized airways**. Geneva, CH, 2007.

KAJI, S.; OKAZAKI, T. Generation of sound by rotor-stator interaction. **Journal of Sound and Vibration**, Elsevier, v. 13, n. 3, p. 281–307, 1970.

______. Propagation of sound waves through a blade row: Ii. analysis based on the acceleration potential method. **Journal of Sound and Vibration**, Elsevier, v. 11, n. 3, p. 355–IN1, 1970.

KEMP, N. H.; SEARS, W. R. Aerodynamic interference between moving blade rows. **Journal of the Aeronautical Sciences**, 1953.

______. The unsteady forces due to viscous wakes in turbomachines. **Journal of the Aeronautical Sciences**, 1955.

KNOWLES ELECTRONICS. **Differential SiSonicTM Microphone With Enhanced RF Protection - Product Datasheet SPM0406HE3H-SB**. Revision e. [S.l.], 2016.

KOBAYASHI, H. Three-dimensional effects on pure tone fan noise due to inflow distortion. In: **11th Fluid and Plasma Dynamics Conference**. [S.l.: s.n.], 1978. v. 1.

KOBAYASHI, H.; GROENEWEG, J. F. Effects of inflow distortion profiles on fan tone noise. **AIAA Journal**, v. 18, n. 8, p. 899–906, 1980.

KOCH, W. On the transmission of sound waves through a blade row. **Journal of sound and vibration**, Elsevier, v. 18, n. 1, p. 111–128, 1971.

KRÖMER, F. J. **Sound emission of low-pressure axial fans under distorted inflow conditions**. [S.l.]: FAU University Press, 2018.

LABORDERIE, J. de; MOREAU, S. Prediction of tonal ducted fan noise. **Journal of Sound and Vibration**, Elsevier, v. 372, p. 105–132, 2016.

LIGHTHILL, M. J. On sound generated aerodynamically i. general theory. **Proc. R. Soc. Lond. A**, The Royal Society, v. 211, n. 1107, p. 564–587, 1952.

______. On sound generated aerodynamically ii. turbulence as a source of sound. **Proc. R. Soc. Lond. A**, The Royal Society, v. 222, n. 1148, p. 1–32, 1954.

LOWIS. **In-duct measurement techniques for the characterisation of broadband aeroengine noise.** 2007. Tese (phdthesis) — University of Southampton, Institute of Sound and Vibration Research, 2007. 145pp.

LOWRIE, B. Simulation of flight effects on aero engine fan noise. In: **2nd Aeroacoustics Conference**. [S.l.: s.n.], 1975. p. 463.

LOWSON, M. Reduction of compressor noise radiation. **The Journal of the Acoustical Society of America**, ASA, v. 43, n. 1, p. 37–50, 1968.

MANI, R. Discrete frequency noise generation from an axial flow fan blade row. **Journal of Basic Engineering**, American Society of Mechanical Engineers, v. 92, n. 1, p. 37–43, 1970.

MANI, R.; HORVAY, G. Sound transmission through blade rows. **Journal of sound and vibration**, Elsevier, v. 12, n. 1, p. 59–83, 1970.

MARTINEZ, B. et al. Baseline acoustic levels of the eesc-usp fan rig. In: **23rd AIAA/CEAS Aeroacoustics Conference**. [S.l.: s.n.], 2017.

______. Design of an instrumented stator vane using mems microphones for unsteady pressure measurements at the eesc-usp fan rig. In: **ICAS 2018 Congress**. [S.l.: s.n.], 2017.

MOREAU, A.; ENGHARDT, L. Improvements of a parametric model for fan broadband and tonal noise. **Journal of the Acoustical Society of America**, [New York: Acoustical Society of America], v. 123, n. 5, p. 3540, 2008.

______. Ranking of fan broadband noise sources based on an experimental parametric study. In: **15th AIAA/CEAS Aeroacoustics Conference (30th AIAA Aeroacoustics Conference)**. [S.l.]: American Institute of Aeronautics and Astronautics (AIAA), 2009.

MUELLER, A. W. Study of stator-vane fluctuating pressures in a turbofan engine for static and flight tests. 1984.

MUELLER, T. J. **Aeroacoustic Measurements**. [S.l.]: Springer, 2001.

NAMBA, M. Three-dimensional analysis of blade force and sound generation for an annular cascade in distorted flows. **Journal of Sound and Vibration**, Elsevier, v. 50, n. 4, p. 479–508, 1977.

PARRY, A.; KINGAN, M.; TESTER, B. Relative importance of open rotor tone and broadband noise sources. In: **17th AIAA/CEAS Aeroacoustics Conference**. [S.l.: s.n.], 2011.

PEAKE, N.; PARRY, A. B. Modern challenges facing turbomachinery aeroacoustics. **Annual Review of Fluid Mechanics**, Annual Reviews, v. 44, p. 227–248, 2012.

PERCIVAL, D. B.; WALDEN, A. T. **Spectral Analysis for Physical Applications**. [S.l.]: Cambridge University Press, 1993.

POSSON, H.; MOREAU, S.; ROGER, M. On the use of a uniformly valid analytical cascade response function for fan broadband noise predictions. **Journal of sound and vibration**, Elsevier, v. 329, n. 18, p. 3721–3743, 2010.

PREISSER, J.; CHESTNUTT, D. Flight effects on fan noise with static and wind tunnel comparisons. In: **8th Aeroacoustics Conference**. [S.l.]: American Institute of Aeronautics and Astronautics (AIAA), 1983.

RIENSTRA, S.; HIRSCHBERG, A. **An introduction to acoustics**. [S.l.]: Eindhoven University of Technology, 2014.

SEARS, W. R. Some aspects of non-stationary airfoil theory and its practical application. **Journal of the Aeronautical Sciences**, v. 8, n. 3, p. 104–108, 1941.

SMITH, M. J. T. **Aircraft Noise**. CAMBRIDGE UNIV PR, 2004. ISBN 0521616999. Disponível em: <http://www.ebook.de/de/product/4289833/michael_j_t_smith_aircraft_noise.html>.

SMITH, S. N. **Discrete frequency sound generation in axial flow turbomachines**. [S.l.]: Citeseer, 1972.

SREE, D. A novel signal processing technique for separating tonal and broadband noise components from counter-rotating open-rotor acoustic data. **International Journal of Aeroacoustics**, SAGE Publications Sage UK: London, England, v. 12, n. 1-2, p. 169–188, 2013.

SREE, D.; STEPHENS, D. a. Improved separation of tone and broadband noise components from open rotor acoustic data. **Aerospace**, Multidisciplinary Digital Publishing Institute, v. 3, n. 3, p. 29, 2016.

STEPHENS, D.; ENVIA, E. Acoustic shielding for a model scale counter-rotation open rotor. In: **17th AIAA/CEAS aeroacoustics conference (32nd AIAA aeroacoustics conference)**. [S.l.: s.n.], 2011. p. 2940.

STEPHENS, D.; SREE, D. Tone and broadband noise separation from acoustic data of a scale-model counter-rotating open rotor. In: **20th AIAA/CEAS Aeroacoustics Conference**. [S.l.: s.n.], 2014. p. 2744.

STEPHENS, D. B.; VOLD, H. Order tracking signal processing for open rotor acoustics. **Journal of Sound and Vibration**, Elsevier, v. 333, n. 16, p. 3818–3830, 2014.

SUTLIFF, D. et al. Baseline acoustic levels of the NASA active noise control fan rig. In: **Aeroacoustics Conference**. [S.l.]: American Institute of Aeronautics and Astronautics (AIAA), 1996.

SUTLIFF, D.; HEIDELBERG, L.; ENVIA, E. Coupling of low speed fan stator vane unsteady pressures to duct modes-measured vs. predicted. In: **5th AIAA/CEAS Aeroacoustics Conference and Exhibit**. [S.l.: s.n.], 1999.

SUTLIFF, D. L. Rotating rake turbofan duct mode measurement system. In: **NOISE-CON**. Institute of Noise Control Engineering, 2005. Disponível em: <http://dx.doi.org/10.1121/1.4779000>.

TYLER, J. M.; SOFRIN, T. G. Axial flow compressor noise studies. **Transactions of the society of automotive engineers**, v. 70, p. 309–32, 1962.

VENTRES, C. S.; THEOBALD, M. A.; MARK, W. D. Turbofan noise generation. volume 1: Analysis. 1982.

WHITEHEAD, D. S. **Vibration and sound generation in a cascade of flat plates in subsonic flow**. [S.l.]: University of Cambridge, 1970.

WILLIAMS, J. F.; HAWKINGS, D. L. Sound generation by turbulence and surfaces in arbitrary motion. **Phil. Trans. R. Soc. Lond. A**, The Royal Society, v. 264, n. 1151, p. 321–342, 1969.

WOODWARD, R.; GLASER, F. Effects of blade-vane ratio and rotor-stator spacing on fan noise with forward velocity. In: **7th Aeroacoustics Conference**. [S.l.: s.n.], 1981. p. 2032.

WOODWARD, R. et al. Fan noise source diagnostic test- circumferential mode measurements results. In: **8th AIAA/CEAS Aeroacoustics Conference & Exhibit**. [S.l.: s.n.], 2002. p. 2427.

Appendix

APPENDIX A – PERFORMANCE CAMPAIGN

A.1 Static Pressure Taps

Figure 70: Static pressure tapping manufacture.

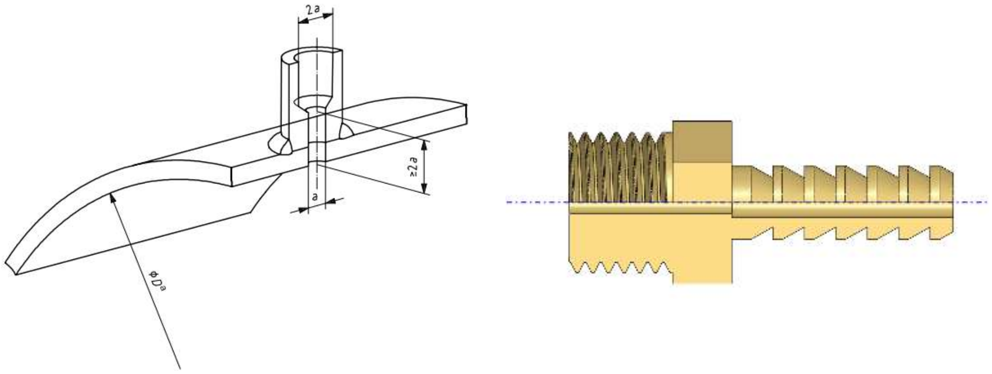

(a) Schematic for tapping design.

(b) Design of tapping manufactured for the Rig.

Source: ISO5801 (2007) and the author.

Figure 71: Tapping connection and position to obtain average static pressure.

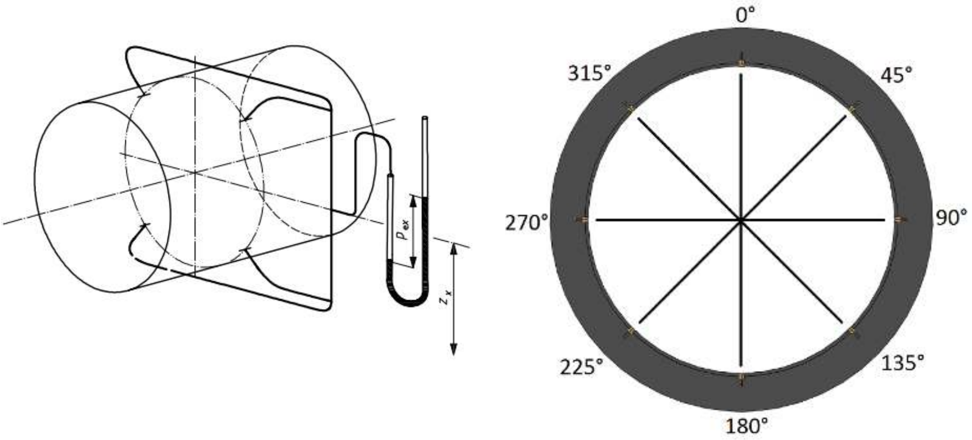

(a) Tapping connection schematic.

(b) Tapping circumferential positions in the Rig.

Source: ISO5801 (2007) and the author.

Figure 72: Static pressure taps installed in the Rig.

(a) Single tapping in place. (b) Connection using silicon hoses.

Source: Elaborated by the author.

Table 6: Positions for traverse measurements.

ISO position	ISO position applied to EESC-USP Fan Rig
0.021D ± 0.0006D	12.60 ± 0.36 mm (from the wall)
0.117D ± 0.0035D	70.20 ± 2.10 mm (from the wall)
0.184D ± 0.0050D	110.4 ± 3.00 mm (from the wall)
0.345D ± 0.0050D	207.0 ± 3.00 mm (from the wall)
0.655D ± 0.0050D	Mirrorred
0.816D ± 0.0050D	Mirrorred
0.883D ± 0.0035D	Mirrorred
0.979D ± 0.0006D	Mirrorred

Source: Elaborated by the author.

A.2 Design of Experiments

Table 7: Performance Campaign Test Matrix.

	#	RSS	ICD	Throt	RPM		#	RSS	ICD	Throt	RPM		#	RSS	ICD	Throt	RPM
No Area Restr.	1	0	1	1	500	40% Area Restr.	15	0	1	3	500	60% Area Restr.	29	0	1	3	500
	2	0	1	1	1000		16	0	1	3	1000		30	0	1	3	1000
	3	0	1	1	1500		17	0	1	3	1500		31	0	1	3	1500
	4	0	1	1	2000		18	0	1	3	2000		32	0	1	3	2000
	5	0	1	1	2500		19	0	1	3	2500		33	0	1	3	2500
	6	0	1	1	3000		20	0	1	3	3000		34	0	1	3	3000
	7	0	1	1	3500		21	0	1	3	3500		35	0	1	3	3500
25% Area Restr.	8	0	1	2	500	50% Area Restr.	22	0	1	4	500	70% Area Restr.	36	0	1	4	500
	9	0	1	2	1000		23	0	1	4	1000		37	0	1	4	1000
	10	0	1	2	1500		24	0	1	4	1500		38	0	1	4	1500
	11	0	1	2	2000		25	0	1	4	2000		39	0	1	4	2000
	12	0	1	2	2500		26	0	1	4	2500		40	0	1	4	2500
	13	0	1	2	3000		27	0	1	4	3000		41	0	1	4	3000
	14	0	1	2	3500		28	0	1	4	3500		42	0	1	4	3500

Source: Elaborated by the author.

APPENDIX B – PARAMETRIC CAMPAIGN

B.1 Inlet Control Device

A dome-shaped ICD, inspired on the one described at [1], was built and installed at the bellmouth of the EESC-USP Fan Rig inlet. It was fabricated with tubular aluminum structure, where a screen gauze, with an open area of 62%, was riveted.

B.2 Design of Experiments

Tables 8, 9 and 10 contain the test matrices for the parametric campaign.

Table 8: Test Matrix for Battery of Tests 1 of the Paramatric Campaign.

	Battery of Tests 1: RSS 0																	
	With ICD						Without ICD						With Turbulence Grid					
	#	**RSS**	**ICD**	**Throt**	**RPM**	**# Mics**	#	**RSS**	**ICD**	**Throt**	**RPM**	**# Mics**	#	**RSS**	**ICD**	**Throt**	**RPM**	**# Mics**
No Area Restr.	1	0	1	0	4500	33+23+21	21	0	0	0	4500	33+23+21	41	0	2	0	4500	33+23+21
	2	0	1	0	4250	33+23+21	22	0	0	0	4250	33+23+21	42	0	2	0	4250	33+23+21
	3	0	1	0	4000	33+23+21	23	0	0	0	4000	33+23+21	43	0	2	0	4000	33+23+21
	4	0	1	0	3750	33+23+21	24	0	0	0	3750	33+23+21	44	0	2	0	3750	33+23+21
	5	0	1	0	3500	33+23+21	25	0	0	0	3500	33+23+21	45	0	2	0	3500	33+23+21
25%Area Restr.	6	0	1	1	4500	33+23+21	26	0	0	1	4500	33+23+21	Not tested					
	7	0	1	1	4250	33+23+21	27	0	0	1	4250	33+23+21	Not tested					
	8	0	1	1	4000	33+23+21	28	0	0	1	4000	33+23+21	Not tested					
	9	0	1	1	3750	33+23+21	29	0	0	1	3750	33+23+21	Not tested					
	10	0	1	1	3500	33+23+21	30	0	0	1	3500	33+23+21	Not tested					
40% Area Restr.	11	0	1	2	4500	33+23+21	31	0	0	2	4500	33+23+21	51	0	2	2	4500	33+23+21
	12	0	1	2	4250	33+23+21	32	0	0	2	4250	33+23+21	52	0	2	2	4250	33+23+21
	13	0	1	2	4000	33+23+21	33	0	0	2	4000	33+23+21	53	0	2	2	4000	33+23+21
	14	0	1	2	3750	33+23+21	34	0	0	2	3750	33+23+21	54	0	2	2	3750	33+23+21
	15	0	1	2	3500	33+23+21	35	0	0	2	3500	33+23+21	55	0	2	2	3500	33+23+21
50% Area Restr.	16	0	1	3	4500	33+23+21	36	0	0	3	4500	33+23+21	56	0	2	3	4500	33+23+21
	17	0	1	3	4250	33+23+21	37	0	0	3	4250	33+23+21	57	0	2	3	4250	33+23+21
	18	0	1	3	4000	33+23+21	38	0	0	3	4000	33+23+21	58	0	2	3	4000	33+23+21
	19	0	1	3	3750	33+23+21	39	0	0	3	3750	33+23+21	59	0	2	3	3750	33+23+21
	20	0	1	3	3500	33+23+21	40	0	0	3	3500	33+23+21	60	0	2	3	3500	33+23+21

Source: Elaborated by the author.

Table 9: Test Matrix for Battery of Tests 2 of the Paramatric Campaign.

Battery of Tests 2: RSS 1																		
	With ICD						Without ICD						With Turbulence Grid					
	#	**RSS**	**ICD**	**Throt**	**RPM**	**# Mics**	**#**	**RSS**	**ICD**	**Throt**	**RPM**	**# Mics**	**#**	**RSS**	**ICD**	**Throt**	**RPM**	**# Mics**
No Area Restr.	1	1	1	0	4500	33+23+21	21	1	0	0	4500	33+23+21	41	1	2	0	4500	33+23+21
	2	1	1	0	4250	33+23+21	22	1	0	0	4250	33+23+21	42	1	2	0	4250	33+23+21
	3	1	1	0	4000	33+23+21	23	1	0	0	4000	33+23+21	43	1	2	0	4000	33+23+21
	4	1	1	0	3750	33+23+21	24	1	0	0	3750	33+23+21	44	1	2	0	3750	33+23+21
	5	1	1	0	3500	33+23+21	25	1	0	0	3500	33+23+21	45	1	2	0	3500	33+23+21
25%Area Restr.	6	1	1	1	4500	33+23+21	26	1	0	1	4500	33+23+21	46	1	2	1	4500	33+23+21
	7	1	1	1	4250	33+23+21	27	1	0	1	4250	33+23+21	47	1	2	1	4250	33+23+21
	8	1	1	1	4000	33+23+21	28	1	0	1	4000	33+23+21	48	1	2	1	4000	33+23+21
	9	1	1	1	3750	33+23+21	29	1	0	1	3750	33+23+21	49	1	2	1	3750	33+23+21
	10	1	1	1	3500	33+23+21	30	1	0	1	3500	33+23+21	50	1	2	1	3500	33+23+21
40%Area Restr.	11	1	1	2	4500	33+23+21	31	1	0	2	4500	33+23+21	51	1	2	2	4500	33+23+21
	12	1	1	2	4250	33+23+21	32	1	0	2	4250	33+23+21	52	1	2	2	4250	33+23+21
	13	1	1	2	4000	33+23+21	33	1	0	2	4000	33+23+21	53	1	2	2	4000	33+23+21
	14	1	1	2	3750	33+23+21	34	1	0	2	3750	33+23+21	54	1	2	2	3750	33+23+21
	15	1	1	2	3500	33+23+21	35	1	0	2	3500	33+23+21	55	1	2	2	3500	33+23+21
50%Area Restr.	16	1	1	3	4500	33+23+21	36	1	0	3	4500	33+23+21	56	1	2	3	4500	33+23+21
	17	1	1	3	4250	33+23+21	37	1	0	3	4250	33+23+21	57	1	2	3	4250	33+23+21
	18	1	1	3	4000	33+23+21	38	1	0	3	4000	33+23+21	58	1	2	3	4000	33+23+21
	19	1	1	3	3750	33+23+21	39	1	0	3	3750	33+23+21	59	1	2	3	3750	33+23+21
	20	1	1	3	3500	33+23+21	40	1	0	3	3500	33+23+21	60	1	2	3	3500	33+23+21

Source: Elaborated by the author.

Table 10: Test Matrix for Battery of Tests 1 of the Paramatric Campaign: Extra Tests.

Battery of Tests 1: RSS 0 (Extra Tests)						
	With ICD					
	#	**RSS**	**ICD**	**Throt**	**RPM**	**# Mics**
60% Area Restr.	71	0	1	1	4500	33+23+21
	72	0	1	1	4250	33+23+21
	73	0	1	1	4000	33+23+21
	74	0	1	1	3750	33+23+21
	75	0	1	1	3500	33+23+21
70% Area Restr.	76	0	1	2	4500	33+23+21
	77	0	1	2	4250	33+23+21
	78	0	1	2	4000	33+23+21
	79	0	1	2	3750	33+23+21
	80	0	1	2	3500	33+23+21

Source: Elaborated by the author.

Table 11: Flow measurements

Condition	**RPM**	**Throt.**	ρ **[kg/m3]**	$M_{inlet,a}$[1]	M_{axial}	M_{tip}	**J**	α_{hub} **[deg]**	α_{tip} **[deg]**	$p_{st,1}$ **[Pa]**	$p_{st,2}$ **[Pa]**	$p_{st,3}$ **[Pa]**	$p_{st,4}$ **[Pa]**	**Reynolds**
1	4250	0%	1.052	0.106	0.127	0.343	1.258	17.48	1.28	-511.8	-1325	-721	-557	4.1E+05
2	4250	0%	1.062	0.107	0.128	0.344	1.257	17.50	1.30	-421.5	-1340	-712	-563	4.1E+05
3[2]	4250	0%												
4	4250	25%	1.050	0.098	0.117	0.339	1.159	19.81	2.85	-437.1	-1121	-130	21.7	4.0E+05
5	4250	40%	1.058	0.087	0.104	0.336	1.026	23.27	5.01	-343.8	-909.1	470.1	646.5	4.0E+05
6	4250	50%	1.056	0.079	0.094	0.332	0.929	26.02	6.62	-284.7	-744.7	825	990.5	4.0E+05
7	4250	60%	1.055	0.063	0.075	0.327	0.741	31.96	9.82	-182.4	-485.3	1285	1280	3.9E+05
8	4250	70%	1.055	0.038	0.046	0.322	0.451	42.77	14.94	-67.6	110	1140	1108	3.9E+05
9	4500	0%	1.053	0.113	0.135	0.363	1.260	17.42	1.24	-580	-1496	-845	-639	4.3E+05
10	4000	0%	1.051	0.100	0.120	0.322	1.258	17.48	1.28	-456.2	-1168	-633	-494	3.9E+05
11	3750	0%	1.051	0.093	0.112	0.302	1.255	17.54	1.33	-399.9	-1028	-551	-436	3.6E+05
12	3500	0%	1.051	0.088	0.105	0.282	1.262	17.37	1.21	-348.8	-894	-476	-375	3.4E+05
13	4500	0%	1.063	0.112	0.134	0.364	1.248	17.71	1.44	-470.6	-1503	-792	-636	4.4E+05
14	4000	0%	1.061	0.100	0.120	0.324	1.255	17.55	1.33	-372.8	-1183	-626	-493	3.9E+05
15	3750	0%	1.061	0.093	0.112	0.303	1.250	17.65	1.40	-326.2	-1027	-546	-422	3.6E+05
16	3500	25%	1.060	0.087	0.105	0.283	1.250	17.66	1.41	-285.3	-902	-478	-373	3.4E+05
17	4250	40%	1.059	0.097	0.117	0.340	1.152	20.00	2.97	-356.6	-1131	-153	38.8	4.1E+05
18	4250	60%	1.057	0.088	0.106	0.336	1.042	22.84	4.75	-291.7	-925.9	400.3	619	4.0E+05
19	4250	0%	1.056	0.064	0.077	0.328	0.758	31.39	9.53	-156.5	-504.5	1260	1264	3.9E+05
20[2]	4250	40%												

Source: Elaborated by the author.

---

[1] M_{inlet} refers to the axial speed on the duct before the contraction to the diameter of the fan (0.5 m)

[2] Only spectral analysis of these conditions were performed, due to lack of microphones available on test occasion

APPENDIX C – INSTRUMENTED VANE CAMPAIGN

C.1 Design of Experiments

Table 12 contains the test matrix for the instrumented stator vane campaign.

Table 12: Test Matrix for the Instrumented Stator Vane Campaign.

	#	**RSS**	**ICD**	**Throttle**	**RPM**	**Antenna Mics**	**Vane Mics**
Without ICD No Area Restr. (baseline)	1	0	0	0	4250	33+23+0	21
	2	0	0	0	4000	33+23+0	21
	3	0	0	0	3750	33+23+0	21
	4	0	0	0	3500	33+23+0	21
	5	0	0	0	3250	33+23+0	21
	6	0	0	0	3000	33+23+0	21
	7	0	0	0	2750	33+23+0	21
	8	0	0	0	2500	33+23+0	21
	9	0	0	0	2250	33+23+0	21
	10	0	0	0	2000	33+23+0	21
25% Area Restr.	11	0	0	1	4250	33+23+0	21
	12	0	0	1	4000	33+23+0	21
	13	0	0	1	3750	33+23+0	21
	14	0	0	1	3500	33+23+0	21
	15	0	0	1	3250	33+23+0	21
	16	0	0	1	3000	33+23+0	21
With ICD	17	0	1	0	4250	33+23+0	21
	18	0	1	0	4000	33+23+0	21
	19	0	1	0	3750	33+23+0	21
	20	0	1	0	3500	33+23+0	21
	21	0	1	0	3250	33+23+0	21
	22	0	0	0	3000	33+23+0	21

Source: Elaborated by the author.